Three-Body Halo Nuclei in an Effective Theory Framework

Dissertation

zur

Erlangung des Doktorgrades (Dr. rer. nat.)

der

Mathematisch–Naturwissenschaftlichen Fakultät

der

Rheinischen Friedrich–Wilhelms–Universität Bonn

vorgelegt von

David L. Canham

aus

Mesa, AZ, USA

Bonn 2009

Angefertigt mit Genehmigung der Mathematisch–Naturwissenschaftlichen Fakultät der Rheinischen Friedrich–Wilhelms–Universität Bonn

Diese Dissertation ist auf dem Hochschulschriftenserver der ULB Bonn unter http://hss.ulb.uni-bonn.de/diss_online elektronisch publiziert.

Erscheinungsjahr: 2009

Referent: Prof. Dr. Hans-Werner Hammer

Koreferent: Prof. Dr. Ulf–G. Meißner

Tag der Promotion: 20. Mai 2009

Three-Body Halo Nuclei in an Effective Theory Framework

The universal properties and structure of halo nuclei composed of two neutrons ($2n$) and a core are investigated within an effective quantum mechanics framework. We construct an effective interaction potential that exploits the separation of scales in halo nuclei and treat the nucleus as an effective three-body system, which to leading order is described by the large S-wave scattering lengths in the underlying two-body subsystems. The uncertainty from higher orders in the expansion is quantified through theoretical error bands. First, we investigate the possibility to observe excited Efimov states in $2n$ halo nuclei. Based on the experimental data, ^{20}C is the only halo nucleus candidate to possibly have an Efimov excited state, with an energy less than 7 keV below the scattering threshold. Second, we study the structure of ^{20}C and other $2n$ halo nuclei. In particular, we calculate their matter density form factors, radii, and two-neutron opening angles.

We then make a systematic improvement upon these calculations by extending the effective potential to the next-to-leading order. To this order, we require an additional two-body parameter, which we tune to the effective range of the interaction. In addition to range corrections to the $2n$ halo nuclei results, we show corrections to the Efimov effect in the three-boson system. Furthermore, we explore universality in the linear range corrections to the Efimov spectrum.

Finally, we study the scattering of D^0 and D^{*0} mesons and their antiparticles off the $X(3872)$ in an effective field theory for short-range interactions. We present results for the S-wave scattering amplitude, total interaction cross section and S-wave scattering length.

Mom and Dad

By wisdom the Lord *laid the earth's foundations,*
by understanding he set the heavens in place;
by his knowledge the deeps were divided,
and the clouds let drop the dew.
Proverbs 3:19–20

And these are but the outer fringe of his works;
how faint the whisper we hear of him!
Who then can understand the thunder of his power?
Job 26:14

Contents

Chapter 1

Introduction

There has been a considerable interest in physical systems with large scattering lengths recently. The scattering of two particles with short-range interactions at sufficiently low energy is determined by their S-wave scattering length a. If a is much larger than the range of the interaction R, the system shows universal properties which are independent of the details of the underlying potential [Br06b]. The simplest example is the existence of a shallow two-body bound state if a is large and positive, but there are many more, including the effects of a limit cycle [Bed99] and the Efimov effect [Ef70] in the three-body system.

The best known example of a nuclear system with a large scattering length is the two-nucleon (NN) system. There are two independent S-wave scattering lengths that govern the low-energy scattering of nucleons. Both scattering lengths are significantly larger than the range of the interaction $R \sim 1/m_\pi \approx 1.4$ fm, with the scattering length in the triplet channel being approximately three times as large, and that in the singlet channel about nine times as large. The effective ranges in both channels are of the same order as R. The corresponding shallow bound state in the NN system is the deuteron.

The deuteron is also the simplest example of what are known as *halo nuclei*: nuclear systems which consist of a tightly bound *core* surrounded by a "halo" of lightly bound nucleons. Halo nuclei are characterized by their large nuclear radius compared to the radius of the core, or equivalently, the separation energy of the halo nucleons is small compared to the excitation energy of the core. For example, ^{6}He can be considered to be a three-body bound state of the alpha particle with two lightly bound neutrons in the halo, therefore, known as a $2n$ halo nucleus. The two neutrons are bound to the alpha particle with a separation energy of ≈ 0.97 MeV, which is very small in comparison to the binding energy of the alpha particle, ≈ 28.3 MeV. Due to this separation of scales, halo nuclei offer the possibility of exploring universal behavior [Ri94, Zh93, Hans95, Ta96, Je04].

Also, the separation of scales found in systems with large scattering lengths allows for the use of effective theories, which provide for systematically improvable calculations of observables with realistic uncertainties. In few-nucleon systems, it

is practical to use an effective theory built up of contact interactions in an expansion in $r_0/|a|$, where r_0 is the effective range of the interaction. Such an effective theory has successfully been applied to various two-, three-, and four-nucleon observables (See Refs. [Bed02, Bed03a, Pl05] and references therein). For halo nuclei, one can assume the core to be a structureless particle, and treat the nucleus as a few-body system of the core and the valence nucleons. An effective field theory (EFT) comprised of contact interactions was first applied to study two-body halo nuclei in Refs. [Ber02, Bed03b], where the unbound alpha-neutron system was considered.

In this thesis, we focus mainly on $2n$ halo nuclei composed of a core and two valence neutrons. Such systems are interesting as they can display universal three-body behavior, specifically the Efimov effect [Ef70]. Efimov found that in three-body systems of non-relativistic particles, if at least two of the three pairs of particles have a large scattering length $|a|$ compared to the range R of the interaction, there occurs a sequence of three-body bound states whose binding energies are spaced geometrically between $\hbar^2/mR^2$ and $\hbar^2/ma^2$. The number of bound states grows to infinity, with an accumulation point at the three-body scattering threshold, in the limit $\pm a \to \infty$. The sequence of three-body bound states has universal properties that are independent of the details of the two-body potential at short distances. For example, in this so called resonant limit, $a = \pm\infty$, there exists a discrete scaling symmetry and a discrete scaling factor λ_0 which relates the binding energies of neighboring Efimov states as the threshold is approached: $B_3^{(n)} = \lambda_0^2 B_3^{(n+1)}$ as $n \to \infty$.

The first experimental evidence for Efimov states was found through their signature in the recombination rate of ultracold Cesium atoms [Kr06]. In such ultracold atomic systems, the scattering length can be experimentally tuned by varying an external magnetic field in what is known as a *Feshbach resonance* [Fes62]. In this way, the scattering length can be set to an almost arbitrarily large value, where the physics of the system is dominated by universal behavior, and in the three-body sector by so called Efimov physics. Specifically, if there is an Efimov trimer near the scattering threshold, there will be a resonant enhancement of scattering processes. There appears just such a resonant enhancement of the measured recombination rate in the lowest hyperfine state of ultracold ^{133}Cs atoms at $a \sim -850a_0$ due to the presence of an Efimov trimer at the three-body threshold [Kr06]. At this value of the scattering length, three atoms can form a shallow Efimov bound state, and consequently leave the trap. More recent experiments have utilized Feshbach resonances and have possibly found the characteristic signature of the Efimov effect in other ultracold atomic systems [Kn08, Ot08, Hu08, Ba09].

At this point we begin to understand what is meant by the *universality* of systems with large scattering lengths. A property is considered to be universal if it applies to various systems with much different length (or energy) scales. As mentioned above, the simplest universal property of systems with a large and positive scattering length is the shallow two-body bound state, with a binding energy given by the universal formula: $B_2 = \hbar^2/2\mu a^2$, where μ is the reduced mass of the dimer system. We have already identified the deuteron as the dimer in the NN system. At the atomic scale,

the large scattering length of the ^{4}He system leads to a shallow ^{4}He dimer which is used to extract the scattering length [Gr00].

In this work, we are interested in looking at the universal properties of three-body systems with large scattering lengths. As we already mentioned, the main focus will be on $2n$ halo nuclei systems, but we will also show how these results can be applied to the Efimov effect found for three identical bosons. Also, we explore the three-body particle-dimer scattering in the growing field of mesonic molecules.

The thesis is organized as follows: In Ch. 2, we provide a brief overview of the basic theoretical concepts which are central to this work. We discuss in more detail the already often mentioned scattering length as it is defined through the effective range expansion in scattering theory. We also define what is meant by the natural low-energy length scale, as well as provide examples of systems with large scattering lengths. We give a brief introduction to effective theories, and analyze the two-body system with large scattering length through an EFT with contact interactions. This EFT lays the groundwork for the effective quantum mechanics approach which is used in the bulk of this work.

We then introduce the formalism needed in solving the non-relativistic three-body problem through the well known Faddeev equations in Ch. 3. We also introduce the Jacobi momenta which describe the motion of the three-body system and build a complete set of partial wave projected basis states to be used in our quantum mechanical framework. From the general results we derive the Faddeev equations for solving the $2n$ halo nucleus problem.

In Ch. 4, we explore the occurrence of the Efimov effect and its well known universal properties for $2n$ halo nuclei with a core of spin zero using an effective potential. We perform all of the calculations to leading order, in which only the scattering length plays a role. We show explicitly the renormalization of the two-body potential, which is necessary for a proper renormalization of the three-body problem. After doing this, we review the universal properties of the Efimov effect, before determining which known $2n$ halo nuclei exhibit the possibility of having an excited Efimov state. Generally, we show what the values of the two-body energies or, in other words, how large the scattering lengths must be in order to produce at least one Efimov excited state, when the three-body ground state energy is known. From the earliest studies of halo nuclei, ^{20}C has been suggested as a good candidate for Efimov states [Fed94], with future theoretical work supporting this prediction [Amo96, Maz00]. We critically examine these earlier studies and perform an improved analysis in the framework of an effective theory. We also look at the structure of known halo nuclei, calculating the one- and two-body matter density form factors. From these results we can extract various mean square radii, and calculate other geometrical properties, specifically the two-neutron opening angle. Throughout this chapter, the uncertainties of our leading order analysis are quantified through error bands.

In Ch. 5, we provide a systematic improvement of our LO results by including the next-to-leading order (NLO) term in the effective potential. It is at this order that the effective range of the interaction comes into play. After showing in detail the

process of renormalizing the two-body potential, we discuss various characteristics of the two-body problem to NLO which then play an important role in the three-body problem. Specifically, we look at the pole structure of the two-body T-matrix, as well as re-derive a constraint on the effective range arising from the use of a short-range effective potential. We then apply our results to the three-boson system, in order to calculate NLO corrections to the Efimov effect, which are important to systems of ultracold atoms near a Feshbach resonance. We explore universality in the linear range corrections similarly to that done in Ref. [Pl08]. We also look at universal aspects of the structure of Efimov states to NLO by calculating the mean square distance of the two bosons in the dimer subsystem, as well as the distance of the spectator boson from the center of mass. We then move on to calculate the NLO corrections to the $2n$ halo nuclei results found in Ch. 4. Although the effective ranges for the various two-body subsystems of known $2n$ halo nuclei are not well known, we estimate this value to be of the order of the natural low-energy length scale.

In Ch. 6, we step away from the bound state problem to explore the universal properties of particle-dimer scattering. For this analysis, we no longer use the quantum mechanics framework, but rather return to an EFT similar to that derived in Ref. [Bed99]. We also no longer consider nuclear systems, but rather explore the universal scattering which may be found in the growing field of exotic charmonium states. The recently discovered $X(3872)$ meson is very close to the $D^{*0}\bar{D}^0$ threshold, and as a result, has a resonant S-wave coupling to the $D^{*0}\bar{D}^0$ system. It is then possible that the $X(3872)$ is a weakly bound $D^{*0}\bar{D}^0$ dimer molecule with a large positive scattering length (see Ref. [Br08d] and references therein). We present novel predictions for the scattering of D^0 and D^{*0} mesons and their antiparticles off the $X(3872)$ in pionless EFT.

In the final chapter we briefly summarize our main results and provide an outlook to the possibilities for future studies of systems with large scattering lengths.

Chapter 2

Overview

To start the exploration into three-body systems with large scattering lengths, we wish to provide a brief overview of the main theoretical topics which will be used throughout this thesis. We begin with a review of quantum mechanical scattering theory in order to define the already mentioned *scattering length* through its origin in the *effective range expansion*. We then define the *natural low-energy length scale* in order to understand what is meant by a *large* scattering length. As examples, we briefly describe two systems with large scattering lengths, the neutron-neutron interaction and the mesonic molecule $X(3872)$, both of which appear in the two main topics of this thesis.

The second half of this chapter provides a brief introduction to *effective theories*. A review of the concepts of *effective field theory* (EFT) is illustrated by the EFT for a two-boson system with large scattering length. This EFT is important to the rest of this thesis, as it provides the foundation for the three-body systems we will later explore. We also show explicitly the connection between the EFT solution and the scattering theory results. We conclude this chapter by briefly describing the usefulness of an effective quantum mechanical theory as an analogous approach to calculating low-energy observables in systems with large scattering lengths.

2.1 Scattering Theory Concepts

In this section we give a brief review of some basic concepts of scattering theory which are central to this work, including the *scattering length*, the *effective range expansion*, and how these relate to the *scattering amplitude* and *bound states*. Then, the unnaturally large scattering length will be defined in terms of a *natural low-energy length scale*, and some examples of systems with large scattering lengths will be given. More detailed reviews with a focus on ultracold atoms can be found in Refs. [Da99, He99].

2.1.1 Scattering Theory Basics

The most important parameter in the low-energy interactions of particles is the two-body S-wave scattering length, which we now refer to as simply the *scattering length*. Therefore, we now wish to review the origins of this parameter in the partial wave expansion of the scattering amplitude. Let us start with the low-energy elastic scattering of two identical particles with mass m which interact through a short-range potential. In the center-of-mass frame, the momenta of the particles are $\pm\hbar\vec{k}$ and their total kinetic energy $E = \hbar^2k^2/m$. The elastic scattering is described by a stationary wave function $\psi(\vec{r})$ where $\vec{r}$ is the separation of the two particles. The behavior in the asymptotic limit $r \to \infty$, is the sum of a plane wave, for the incoming part, and a spherical wave, for the outgoing scattered part. Taking the z-direction as the direction of the incoming wave, the wave function is

$$\psi(\vec{r}) = e^{ikz} + f_k(\theta)\frac{e^{ikr}}{r}\,, \tag{2.1}$$

where $f_k(\theta)$ is the *scattering amplitude* arising from the two-body interaction potential. The scattering amplitude depends on the scattering angle θ and the wave number k, and can be used to find the *differential cross section*:

$$\frac{d\sigma}{d\Omega} = |f_k(\theta) \pm f_k(\pi - \theta)|^2\,, \tag{2.2}$$

where the plus(minus) sign is used if the particles are identical bosons(fermions). If the particles are distinguishable, the second term $f_k(\pi - \theta)$ would be omitted. Because the particles are identical, to obtain the cross section for elastic scattering, one must integrate over only half of the 4π solid angle (and over the whole solid angle for distinguishable particles). However, the total cross section is related to the forward-scattering limit of the scattering amplitude by the optical theorem:

$$\sigma^{(total)} = \frac{8\pi}{k}\mathrm{Im}f_k(\theta = 0)\,. \tag{2.3}$$

Distinguishable particles would have a prefactor of 4π rather than 8π. If there are no inelastic channels in the two-body scattering, the total cross section is equal to the elastic cross section found from integrating Eq. (2.2) over half of the total solid angle. Otherwise, the total cross section would be the sum of the elastic and inelastic cross sections.

In the low-energy limit ($k \to 0$ or $E \to 0$), the scattering amplitude becomes an isotropic constant. This low-energy limit to the scattering amplitude is the sought after scattering length a:

$$f_k(\theta) \to -a \qquad \text{as } k \to 0\,. \tag{2.4}$$

Measurement of the low-energy limit of the elastic cross section provides a way of determining the absolute value of a:

$$\sigma(E) \to 8\pi a^2 \qquad \text{as } E \to 0\,, \tag{2.5}$$

where, again, distinguishable particles would have a prefactor of 4π rather than 8π. Determining the sign of a requires the measurement of a more complicated interference effect. Inelastic channels at $E = 0$ would require complex values of a, and thus a^2 in Eq. (2.5) would need to be replaced with $|a|^2$.

Since we noted that a is the two-body S-wave scattering length, it is useful to resolve the scattering amplitude $f_k(\theta)$ into the contributions from the definite angular momentum quantum number l (of which the S-wave corresponds to $l = 0$), by the partial wave expansion, an expansion in terms of Legendre polynomials:

$$f_k(\theta) = \frac{1}{k}\sum_{l=0}^{\infty}(2l+1)c_l(k)P_l(\cos\theta)\,. \tag{2.6}$$

For bosons, only the even values of l contribute to the differential cross section in Eq. (2.2), while for fermions only the odd values of l contribute. Unitarity places a constraint on the values of the coefficients $c_l(k)$ in Eq. (2.6): $|c_l| \leq 1$. Writing the coefficients in terms of *phase shifts* $\delta_l(k)$ takes into account these unitarity constraints automatically:

$$c_l(k) = e^{i\delta_l(k)}\sin\delta_l(k)\,. \tag{2.7}$$

Substituting this into Eq. (2.6) then gives a scattering amplitude:

$$f_k(\theta) = \sum_{l=0}^{\infty}\frac{2l+1}{k\cot\delta_l(k) - ik}P_l(\cos\theta)\,. \tag{2.8}$$

Inelastic channels in the scattering would produce complex values for the phase shifts with positive imaginary parts. However, if there exists only elastic scattering, the phase shifts are real valued and integrating Eq. (2.2) over half the solid angle with Eq. (2.8) substituted for $f_k(\theta)$ would give

$$\sigma(E) = \frac{8\pi}{k^2}\sum_{l=0}^{\infty}(2l+1)\sin^2\delta_l(k)\,. \tag{2.9}$$

Distinguishable particles would have a prefactor of 4π rather than 8π. Recall that the total kinetic energy in the system is related to the center-of-mass momentum, $E = \hbar^2k^2/m$. Again, for bosons the summation is taken over only even values of l, and for fermions over odd values.

We are interested in two-body scattering of identical particles due to a short-range potential in the low-energy limit. In the limit $k \to 0$ (or similarly $E \to 0$) the phase shift $\delta_l(k)$ approaches zero like k^{2l+1}. The dominant term in the scattering amplitude thus comes from the lowest partial wave contribution, the S-wave ($l = 0$) for bosons or the P-wave ($l = 1$) for fermions. At these low energies the S-wave phase shift $\delta_0(k)$ can be expanded in powers of k in what is known as the *effective range expansion*. It is most usefully written as

$$k\cot\delta_0(k) = -\frac{1}{a} + \frac{1}{2}r_0k^2 - \frac{1}{4}P_0k^4 + \dots\,, \tag{2.10}$$

where the first term gives the proper definition for the previously defined scattering length a. The next two terms define the S-wave *effective range* r_0, and the S-wave *shape parameter* P_0. These two parameters depend on the specific shape of the interaction potential, and thus their measurement gives useful information on the interaction potential. Substituting Eq. (2.10), keeping only the first two terms, into Eq (2.8) with $l = 0$, gives the low-energy S-wave scattering amplitude:

$$f_k(\theta) = \frac{1}{-1/a + r_0 k^2/2 - ik} \,. \tag{2.11}$$

This shows the isotropic nature of S-wave scattering as well as verifies the earlier definition of a given in Eq. (2.4).

One possibility of the two-body interaction is the two-body bound state, also known as a *dimer*. This requires that the potential have an attractive region which is deep enough for the bound states to form. The poles of the scattering amplitude f_k in the upper half-plane of the complex variable k give the two-body binding energies B_2. It is then useful to define the *binding wave number* κ in terms of the binding energies:

$$B_2 = \frac{\hbar^2 \kappa^2}{m} \,. \tag{2.12}$$

To determine the S-wave bound states, the binding wave number can be found from the pole of Eq. (2.8) for $l = 0$ with $k = i\kappa$. The binding wave number is then the positive real-valued solution to

$$i\kappa \cot \delta_0(i\kappa) + \kappa = 0 \,. \tag{2.13}$$

For a shallow bound state, the effective range expansion of Eq. (2.10) can be substituted into this equation. If the scattering length is large compared to the other coefficients, for example $a \gg r_0$, then only the first term is necessary and the resulting $\kappa = 1/a$ gives a shallow binding energy of

$$B_2 = \frac{\hbar^2}{m a^2} \,, \tag{2.14}$$

with a first correction of order r_0/a.

2.1.2 Natural Low-Energy Length Scale and the Large Scattering Length

In order to define a *large* scattering length, we need the scattering length to be large compared to some known scale. The necessary scale is the *natural low-energy length scale* ℓ, sometimes called the *characteristic radius of interaction*, and thus related

to the interaction potential. At low-energies, the scattering amplitude f_k can be expanded in powers of the wave number k:

$$f_k = c_0 + c_1 k + c_2 k^2 + \dots . \tag{2.15}$$

The natural scale of the expansion coefficients, $c_n = (c_0, c_1, \dots)$, is then set by ℓ. By dimensional analysis, f_k must have the dimension of length, and since k has the dimension of ℓ^{-1}, the coefficient of the k^n term must have the dimension $[c_n] = \ell^{n+1}$. Thus, the coefficient c_n can be rewritten as ℓ^{n+1} multiplied by a new dimensionless coefficient a_n:

$$f_k = a_0 \ell + a_1 \ell^2 k + a_2 \ell^3 k^2 + \dots . \tag{2.16}$$

While there is no general constraint on the magnitude of these coefficients, for a generic potential, there usually exists a length scale ℓ for which all of the coefficients have a magnitude of or near order 1: $|a_n| \sim 1$. To have a coefficient with an absolute value of an order of magnitude much larger than 1 usually requires the *fine-tuning* of specific parameters of the potential, generally related to the shape of the potential. The natural low-energy length scale is defined as the length scale ℓ for which most of the coefficients of the $\ell^{n+1}k^n$ expansion of the scattering amplitude have magnitudes of order 1.

Applied to the effective range expansion, one assumes that for a generic potential, the scattering length a, the effective range parameter r_0, etc. would all have magnitudes comparable to ℓ. Coefficients with a magnitude comparable to ℓ we refer to as having a *natural size*. A large scattering length would result if $|a| \gg \ell$. As stated before, the case of a large scattering length would normally require the fine-tuning of some parameter of the interaction potential. However, even if a is large, the other coefficients in the effective range expansion, such as r_0, should be of natural size. To have more than one coefficient large would require the fine-tuning of two parameters of the potential simultaneously.

As shown at the end of the previous subsection, a large scattering length with an attractive potential can produce a shallow two-body bound state with binding energy $B_2 = \hbar^2/ma^2$. Typically, the shallowest bound state energy would be set by the natural low-energy length scale to $\hbar^2/m\ell^2$ multiplied by some coefficient ~ 1. A large scattering length $|a| \gg \ell$ creates a bound state with energy of magnitude much smaller than expected. Thus, the fine-tuning of the binding energy can be the fine-tuning needed to produce a large positive scattering length.

The fine-tuning necessary to generate a large scattering length can be the lucky consequence of the values of fundamental constants in nature, called *accidental fine-tuning*, or it can be produced by the adjustment of conditions under experimental control, called *experimental fine-tuning*.

An example of accidental fine-tuning important to this work, due to its appearance in three-body halo nuclei, is the large scattering length of the neutron-neutron interaction. Although the neutron is a spin-1/2 fermion, neutrons with opposite spins

can scatter in the S-wave channel. The standard value for the scattering length is $a = (-18.7 \pm 0.6)$ fm [Gon99], and a measurement of the effective range has found $r_0 = (2.75 \pm 0.11)$ fm [Mi90]. The low-energy interactions between two neutrons can be described by a short-range potential generated by the exchange of pions. Therefore, the natural low-energy length scale is the range of the one-pion-exchange calculated by the inverse of the pion mass scale: $\ell_\pi \approx \hbar/m_\pi c = 1.4$ fm. One clearly sees that although the effective range is of natural size, the absolute value of the scattering length is an order of magnitude larger. We will later exploit this separation of scales in order to describe the neutron-neutron interaction with a pionless effective theory built up of zero-range contact interactions (see Ch. 4 and Ch. 5).

More recently, systems with large scattering lengths have been found in particle physics, specifically mesonic molecules. Of particular interest is the $X(3872)$ which was discovered by the Belle collaboration [Ch03] in $B^\pm \to K^\pm \pi^+ \pi^- J/\psi$ decays and shortly after confirmed by the CDF collaboration in $p\bar{p}$ collisions [Ac04]. This state has quantum numbers $J^{PC} = 1^{++}$ and is very close to the $D^{*0}\bar{D}^0$ threshold. As a consequence, the $X(3872)$ has a resonant S-wave coupling to the $D^{*0}\bar{D}^0$ system. Many studies have addressed the nature of the $X(3872)$ and provided predictions for its decay modes based on the assumption that it is a $D^{*0}\bar{D}^0$ molecule with even C-parity:

$$(D^{*0}\bar{D}^0)_+ \equiv \frac{1}{\sqrt{2}}\left(D^{*0}\bar{D}^0 + D^0\bar{D}^{*0}\right) . \tag{2.17}$$

A recent status report can be found in Ref. [Br08d]. Using the latest measurements in the $J/\psi\pi^+\pi^-$ channel [Ada08, Aub08, CDF08], the mass of the $X(3872)$ is [Br09]:

$$m_X = (3871.55 \pm 0.20)\ \text{MeV}\,, \tag{2.18}$$

which corresponds to an energy relative to the $D^{*0}\bar{D}^0$ threshold

$$E_X = (-0.26 \pm 0.41)\ \text{MeV}\,. \tag{2.19}$$

The central value corresponds to a $(D^{*0}\bar{D}^0)_+$ bound state with binding energy $B_X = 0.26$ MeV, but a virtual state can not be excluded from the current data in the $J/\psi\pi^+\pi^-$ and $D^{*0}\bar{D}^0$ channels [Hanh07b]. The $X(3872)$ is also very narrow with a width smaller than 2.3 MeV. Since the binding energy is much smaller than the natural scale, given by the pion mass scale: $m_\pi^2 c^2/(2\mu) \approx 10\ \text{MeV}/c^2$, where μ is the reduced mass of the $D^{*0}\bar{D}^0$ system, the $D^{*0}\bar{D}^0$ scattering length must be much larger than the natural low-energy length scale. If the $X(3872)$ is indeed a $D^{*0}\bar{D}^0$ molecule, it has universal low-energy properties that depend only on its binding energy, some of which we explore in Ch. 6.

Experimental fine-tuning to generate a large scattering length can be done through *shape resonance*, in which the depth or range of the potential is tuned to produce a bound state near the threshold, as illustrated in Fig. 2.1(a). This technique uses

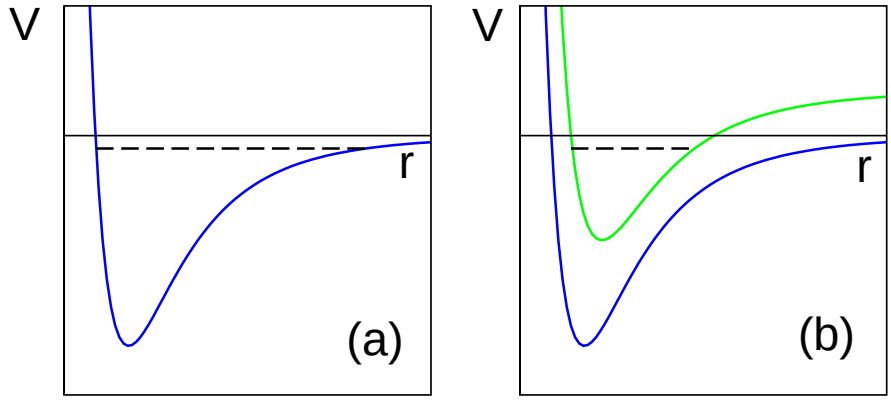

Figure 2.1: Two mechanisms for experimentally generating a large scattering length by tuning a bound state, represented by the dashed lines, to be at the scattering threshold. Left panel(a): a shape resonance in which the bound state is in the potential for the open channel. Right panel(b): the bound state is in the potential for a weakly-coupled closed channel, as in a Feshbach resonance. Figure reproduced with permission from Ref. [Br06b].

only the *open channel*, defined by the scattering particles. Another mechanism for experimentally tuning the scattering length, a *Feshbach resonance* [Fes62], requires the use of a second *closed channel* that is weakly coupled to the open channel, as shown in Fig. 2.1(b). Feshbach resonances in alkali atoms can be generated by tuning the magnetic field [Ti92, Ti93], with the general goal of generating a very weak two-body bound state. This technique is now widely used in ultracold atomic systems, where it is possible to tune the scattering length to magnitudes for which universal behavior is observed, for example in Ref. [Kr06].

2.2 Effective Theories

To understand the low-energy behavior of a physical system, an effective theory is the most general approach. An effective theory is one that is developed within the framework of a more fundamental theory in such a way as to apply only to the desired conditions, interactions, and particles contained within a certain subsystem of the more fundamental "whole." This is done because the fundamental theories are often impractical to work with when considering a smaller subsystem. This division into effective theories normally separates the different behavior of physics at different energy levels [Kap95]. When working at an energy level much lower than that described by the fundamental theory, a more practical effective theory specific to the desired energy level and conditions of the system can be developed. In a way, all physical theories can be thought of as differing levels of effective theories specific to the desired conditions, interactions, and particles of the described system. The

theories that are thought of as most fundamental today also apply to a specific set of parameters, conditions, and energies within the whole physical universe. In the development of physics, this process most often has occurred the other way around. Typically, but not always, the low-energy effective theory was first discovered, with the more fundamental theories coming later.

For example, when measuring the effect of gravity on an object near earth, one finds that the force F on the object is equal to the object's mass m multiplied by a constant acceleration due to gravity g: $F = mg$. Or, when thought of in terms of the potential energy: $V = mgh$, where h is the height of the object. However, this is only an effective theory which applies when considering heights small compared to the radius of the earth. A more fundamental theory would be Newton's theory of gravity: $F = GM_E m/(R_E + h)^2$, or in terms of the potential energy: $V = -GM_E m/(R_E + h)$, where G is the gravitational constant, and M_E and R_E are the mass and radius of the earth. Expanding either of these formulas with respect to h/R_E, one finds that $g = GM_E/R_E^2$, and that the first correction to the effective theory is proportional to h/R_E, which would be negligible for $h \ll R_E$. This demonstrates the important principle of correspondence between an effective theory and its more fundamental theory. The two theories must correspond to one another when the appropriate expansions and approximations are made to the fundamental theory. Moreover, Newton's theory of gravity is also just an effective theory when considering objects with sufficiently light masses. The more fundamental theory is Einstein's General Relativity, the correspondence between the two having been well established [We72]. Going further, General Relativity could be assumed to also be just another effective theory for an even more fundamental theory yet to be discovered.

The application of this general effective theory approach, when applied to field theories, is called effective field theory. For example, *quantum electrodynamics* (QED) is a quantum field theory which describes the behavior of electrons, positrons, and photons. However, the perturbative calculations in QED give rise to intermediate steps with *ultraviolet divergences* which indicate a large dependence on physics at high energies, or short distances. The process of renormalization creates a theory that gives extremely accurate predictions for the behavior of these three particles in terms of two fundamental parameters: the fine structure constant α and the mass of the electron m_e. However, this theory is not complete in that it does not include the effects of heavier charged particles, such as the muon. Adding terms to QED for the interactions involving these heavier particle fields would ruin the renormalizability of the theory. However, an effective theory can be made to describe the effects of virtual heavier particles without adding any new particle fields, assuming that the momenta of the electrons, positrons and photons, and hence the energy in the system, are small compared to the mass of the heavier particles. The effects of virtual heavy particles can be taken into account with increasing accuracy by constructing field theories out of QED with additional interaction terms, for example a magnetic moment interaction term. These terms are constructed from only the electron and photon fields, plus an additional parameter that can be calculated from α, m_e, and the masses of the heavier

particles.

The ultraviolet divergence of QED is representative of divergences found in most calculations using quantum field theories, including work with the Standard Model. From these problems and the growing work with renormalization, effective field theories have been developed to describe many aspects of particle physics [Kap95, Ge93, Man96]. Starting from the Standard Model, effective field theories either work down the energy scale, developing theories to describe low-energy approximations, or up the energy scale, treating the Standard Model as the effective theory of a still more fundamental theory.

In the following subsection, we review the basic components and concepts needed in understanding and developing an effective field theory, and illustrate with the example of low-energy two-body scattering with a large scattering length. After that, we move back from field theories and reintroduce the basic concepts needed in developing an effective quantum mechanical theory.

2.2.1 An Introduction to Effective Field Theories

We now wish to review the basic concepts and components required in an effective field theory by exploring a system of identical particles in the low-energy regime. To start with, the particles interact non-relativistically, and the most fundamental interaction is that between two particles, governed by a two-body potential $V(r)$. The system of N particles of mass m and momentum $\vec{p}_i$ is then described through non-relativistic quantum mechanics by the Schrödinger equation in the Hamiltonian formalism:

$$\hat{H}^{(N)} = \sum_{i=1}^{N} \frac{p_i^2}{2m} + \sum_{i<j} V(r_{ij})\,, \tag{2.20}$$

where $\vec{r}_{ij} = \vec{r}_i - \vec{r}_j$ is the separation between particles i and j and $r_{ij} = |\vec{r}_{ij}|$.

Low-energy for this system means energy close to the N-particle scattering threshold. To describe the low-energy behavior of the system, we require that each particle has kinetic energy and that each pair of particles have potential energy that is small compared to a natural energy scale $\hbar^2/m\ell^2$, where ℓ is the natural low-energy length scale associated with the two-body potential $V(r)$ (see Sec. 2.1.2). Therefore, an effective theory can be developed through the simplest approach, using an effective short-range two-body potential $V_{\text{eff}}(r)$ in the Schrödinger equation, which depends on a set of parameters, $C_i = (C_0, C_1, \ldots)$, which can be tuned to reproduce physical results. The number of tuning parameters used determines the level of accuracy of the reproduced results.

We can now move on to describing the two-body system in a quantum field theory. A quantum field theory equivalent to the quantum mechanical Schrödinger equation for the N-body problem can be formulated through *second quantization*.[1] The

[1] For a textbook treatment of second quantization and quantum field theory see, e.g. [Pes95, Zi02]

quantum field theory is defined in terms of the quantum field operator $\psi(\vec{r})$ and its hermitian conjugate $\psi^\dagger(\vec{r})$ instead of the momentum and position operators $\hat{p}_i$ and $\hat{r}_i$. These operators, respectively, create or annihilate a particle at the point $\vec{r}$. Assuming the particles are bosons, the canonical commutator relations of the momentum and position operators are then replaced with the equal-time commutator relations

$$\left[\psi(\vec{r},t),\psi(\vec{r}',t)\right]=0, \qquad \left[\psi(\vec{r},t),\psi^\dagger(\vec{r}',t)\right]=\delta^3(\vec{r}-\vec{r}')\,. \tag{2.21}$$

These quantum field operators work on quantum states $|Z\rangle$. For example, the number operator defined by

$$\hat{N}=\int d^3r\;\psi^\dagger(\vec{r})\psi(\vec{r}) \tag{2.22}$$

applied to the state $|Z\rangle$ containing exactly N particles will produce the eigenvalue equation

$$\hat{N}|Z\rangle=N|Z\rangle\,. \tag{2.23}$$

The quantum mechanical N-body problem defined in Eq. (2.20) along with the canonical commutator relations of the position and momentum operators can be equivalently described by a quantum field theory with the commutator relations in Eq. (2.21), the N-body constraint in Eq. (2.23), and the time evolution Hamiltonian of the quantum field:

$$\hat{H} \;=\; \int d^3r\frac{\hbar^2}{2m}\nabla\psi^\dagger\cdot\nabla\psi+\frac{1}{2}\int d^3r\int d^3r'\;\psi^\dagger(\vec{r})\psi(\vec{r})V(|\vec{r}-\vec{r}'|)\psi^\dagger(\vec{r}')\psi(\vec{r}')\,. \tag{2.24}$$

Of course, replacing $V(|\vec{r}-\vec{r}'|)$ with $V_{\text{eff}}(|\vec{r}-\vec{r}'|)$ in this equation would produce an effective field theory.

In order to now formulate a suitable effective interaction, some of the concepts of low-energy scattering in quantum theories are needed. At the desired low energies, the particles will behave like point particles with a short-range interaction. Let us explain. The de Broglie wavelength $\lambda=2\pi\hbar/p$, where p is the momentum of the particle, sets the length scale of the quantum nature of the center-of-mass coordinate. The small relative momentum of the two interacting particles in the low-energy limit results in a de Broglie wavelength larger than the spacial extent of the particles, and thus the particles are unable to resolve, or "see," the other's internal structure. The interaction of the two particles is therefore the same as that of two point particles. Furthermore, if the interaction potential is short-ranged, with a range of R, and $p\ll\hbar/R$, then the particles also can not resolve the structure of the potential. The interaction potential then becomes equivalent to a local potential with *contact terms* proportional to the delta function $\delta^3(\vec{r}-\vec{r}')$ and derivatives of the delta function. Higher order effects

of the interaction could be taken into account through the inclusion of higher order derivatives of the delta function.

These concepts of low-energy interactions are taken into account in constructing the effective field theory, and thus we use a *local quantum field theory*. This is equivalent to taking the *scaling limit*. The scaling limit, sometimes called the *zero-range limit*, is achieved by taking the range of the interaction to zero while keeping the scattering length unchanged, thus constructing the effective potential out of contact terms. The effective Hamiltonian can then be expressed as the integral of a Hamiltonian density $\mathcal{H}_{\text{eff}}$:

$$\hat{H}_{\text{eff}} = \int d^3r \, \mathcal{H}_{\text{eff}} \, . \tag{2.25}$$

The Hamiltonian density can only depend on the quantum field at a point $\psi(\vec{r})$ and the gradients of the field at the same point. While, in general, there are an infinite number of terms that can be included in $\mathcal{H}_{\text{eff}}$, several principles can reduce this number to give an effective theory specific to the conditions of the desired problem. Let us first write out the Hamiltonian needed to describe the two-body system with large scattering length and then discuss the principles used to form it:

$$\mathcal{H}_{\text{eff}} = \frac{\hbar^2}{2m}\nabla\psi^\dagger \cdot \nabla\psi + \frac{g_2}{4}(\psi^\dagger\psi)^2 + \frac{h_2}{4}\nabla(\psi^\dagger\psi)\cdot\nabla(\psi^\dagger\psi) + \ldots \, . \tag{2.26}$$

First, a symmetry in the system must also be found in the Hamiltonian, and all symmetries found in the fundamental theory must also appear in the effective theory. The phase symmetry $\psi \to e^{i\alpha}\psi$ of Eq. (2.24), which generates a conservation of particle number, requires that every term in $\mathcal{H}_{\text{eff}}$ have an equal number of ψ and $\psi^\dagger$ factors. The term with N factors each of ψ and $\psi^\dagger$ is referred to as an N-body term. Also, the N-body system is only affected by terms with up to N factors each of ψ and $\psi^\dagger$. Thus, the two-body problem does not require terms with more than 2 factors each of ψ and $\psi^\dagger$. Next, in the non-relativistic problem, there is also a Galilean symmetry which imposes great constraints on the terms in the Hamiltonian. We will not go into the details of these constraints here, but only mention that due to these constraints, no other two-body terms besides the two found in Eq. (2.26) are allowed [Br06b]. Another principle that reduces the number of terms in the effective Hamiltonian is that boundary terms in $\mathcal{H}_{\text{eff}}$ do not change the theory. Therefore, terms that differ by integration by parts are equivalent. For example, the term $\psi^\dagger\psi\nabla^2(\psi^\dagger\psi)$ is equivalent to the term $\nabla(\psi^\dagger\psi)\cdot\nabla(\psi^\dagger\psi)$, and can be excluded. Finally, the terms with additional factors of ∇ have effects that scale with additional powers of the energy E. Therefore, to achieve corrections that scale with the order E^{n+1}, only terms with $2n$ factors of ∇ are required. The Hamiltonian in Eq. (2.26) can thus predict two-body observables up to order E^2, but no higher order corrections can be found.

Just as the tuning parameters C_i of the effective potential V_{eff} can be tuned to reproduce physical observables, the *coupling constants*, g_2 and h_2 in Eq. (2.26), can

be used as tuning parameters to reproduce low-energy observables. Tuned simultaneously, they can reproduce the scattering length a and the effective range r_0 associated with the two-body potential. By adding higher N-body terms to the local quantum field theory, the additional coupling constants can be tuned in order to reproduce the N-body scattering amplitude to a desired order in E, thus assuring the predictive power of the effective field theory in describing low-energy behavior.

The general use of effective field theories of this type runs into the problem of ultraviolet divergences occurring in integrations over virtual states. As stated before, this shows a large dependence on physics at high energy, or small distance, and can often be solved by a process of renormalization. In this case, it is common to resolve this problem through the use of an *ultraviolet cutoff* Λ.

In order to perform calculations with quantum field theories, it is more practical to use the Lagrangian rather than the Hamiltonian formalism. Using the Legendre transformation

$$\mathcal{L} = \Pi \partial_t \psi - \mathcal{H}\,, \tag{2.27}$$

where $\Pi = \partial\mathcal{L}/\partial(\partial_t\psi)$, the Hamiltonian density can be transformed into the Lagrangian density. In our case, $\Pi = \psi^\dagger i$, and integration by parts can be used to set $\nabla\psi^\dagger \cdot \nabla\psi = \psi^\dagger\nabla^2\psi$. Therefore, the Lagrangian density for the two-body problem of identical bosons with large scattering length in the scaling limit is

$$\mathcal{L} = \psi^\dagger \left(i\frac{\partial}{\partial t} + \frac{\hbar}{2m}\nabla^2 \right)\psi - \frac{g_2}{4}\left(\psi^\dagger\psi\right)^2 - \frac{h_2}{4}\nabla(\psi^\dagger\psi)\cdot\nabla(\psi^\dagger\psi) + \dots\,. \tag{2.28}$$

The scattering of two particles can be described by the interaction terms of Eq. (2.28) by calculating the power series expansion of g_2 and h_2 in perturbation theory. However, with a large scattering length one assumes that the interactions are strong and, therefore, the *on-shell scattering amplitude* $\mathcal{T}$ should be calculated non-perturbatively [Kap98, vK99].

Before this analysis can be done, a very brief explanation of the formalism must be presented. The physical observables of a scattering problem come from the S-matrix elements, where the $\hat{S}$ operator is (somewhat schematically):

$$\begin{aligned} \hat{S} &= \mathrm{T} e^{i\int d^4x \mathcal{L}_{int.}} \\ &= \mathbf{1} + i\mathrm{T}\int d^4x \mathcal{L}_{int.} + \cdots\,, \end{aligned} \tag{2.29}$$

where T is the time ordering operator and $\mathcal{L}_{int.}$ represents the interaction terms of the Lagrangian. The S-matrix elements arising from the application of the LSZ Theorem results in the Green's function $\langle 0|\hat{S}|0\rangle$, where $|0\rangle$ is the vacuum state. For our Lagrangian, this reduces to the 4-point Green's function $\langle 0|\mathrm{T}(\psi\psi\psi^\dagger\psi^\dagger)|0\rangle$, where the time and space coordinates have been suppressed. The physical observables are contained more usefully in the truncated connected Green's function in momentum space $i\mathcal{A}$ obtained by subtracting the disconnected terms which have the factored form

$\langle 0|\mathrm{T}(\psi\psi^\dagger)|0\rangle\langle 0|\mathrm{T}(\psi\psi^\dagger)|0\rangle$, Fourier transforming in all coordinates to enter momentum space, and factoring out the overall energy-momentum conserving delta function as well as the propagator arising from external legs. This analysis can more practically be done through the use of Feynman diagrams[2].

Returning to our example, we now calculate the amplitude $i\mathcal{A}$ of the two-body problem with large scattering length to leading order. To this order, only the g_2 interaction term of the Lagrangian is needed. We also use units such that $\hbar = 1$, in order to simplify the calculations. The correct placement of $\hbar$ in the results can be determined by dimensional analysis. As mentioned before, the scattering amplitude resulting from interactions with a large scattering length must be solved non-perturbatively. Therefore, the leading order amplitude is found by solving the integral equation represented by the Feynman diagrams shown in Fig. 2.2.

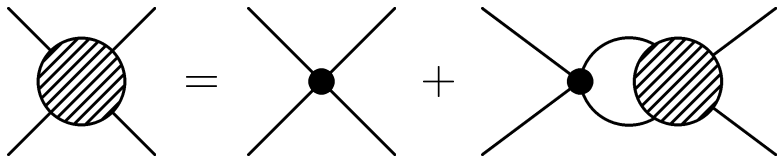

Figure 2.2: Diagrammatic representation of the integral equation for the leading order two-body scattering amplitude $\mathcal{A}$.

The Feynman rules used to write the analytical form of the integral equation from this diagram are shown in Fig. 2.3. These rules are derived from the Lagrangian found in Eq. (2.28). The vertex factors shown in Fig. 2.3a),b) arise straightforwardly from the interaction terms of the Lagrangian. In calculations, both energy and momentum are conserved at each vertex. The loops are constructed from the propagator factor

[2]A complete coverage of the formalism of Feynman diagrams can be found in, e.g. [Pes95].

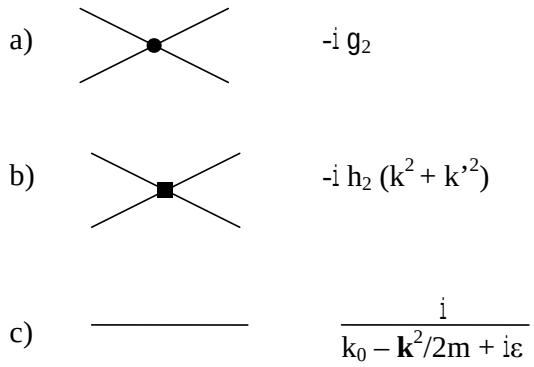

Figure 2.3: Feynman rules for the Lagrangian in Eq. (2.28): a) the vertex for the g_2 contact term, b) the vertex for the h_2 contact term, c) the propagator for a particle with energy k_0, momentum $\vec{k}$, and mass m.

shown in Fig. 2.3c), which comes from the inverse of the kinetic energy term of the Lagrangian in momentum space. However, the energy q_0 and the momentum $\vec{q}$ of propagators which are found in loops are not determined by the external energies and momenta of the incoming and outgoing particles. They must, therefore, be integrated over the phase space $d^4q/(2\pi)^4$. Also, every loop subdiagram that is invariant under the permutation of n internal lines also has a symmetry factor of $1/n!$. In our diagrams, the loop has a symmetry factor of $1/2$ corresponding to the switching of the two propagators found in the loop. Therefore, the integral equation shown diagrammatically in Fig. 2.2, using total energy E, internal propagators with energy q_0 and $E - q_0$ and momenta $\pm\vec{q}$ is

$$\mathcal{A}(E) \;=\; -g_2 - \frac{i}{2} g_2 \int \frac{d^3q}{(2\pi)^3} \int \frac{dq_0}{2\pi} \frac{1}{q_0 - q^2/2m + i\epsilon} \frac{1}{E - q_0 - q^2/2m + i\epsilon} \mathcal{A}(E)\,. \tag{2.30}$$

The function $\mathcal{A}(E)$ is independent of $\vec{q}$ and q_0 and can therefore be taken out of the integral. Next, the integral over q_0 can be done easily through contour integration on the complex plane, and we find:

$$\mathcal{A}(E) = -g_2 - \frac{1}{2} m g_2 \mathcal{A}(E) \int \frac{d^3q}{(2\pi)^3} \frac{1}{mE - q^2 + i\epsilon}\,. \tag{2.31}$$

The integral over $\vec{q}$ can be done in spherical coordinates. While the integration over the 4π solid angle is easy to perform, the integral over $q \equiv |\vec{q}|$ has the expected ultraviolet divergence. This divergence is regularized by imposing an ultraviolet cutoff on the upper limit of integration, $q < \Lambda$. The integral is now analytically solvable, and in the limit $\Lambda \gg |E|^{1/2}$ we find for our final result:

$$\mathcal{A}(E) = -g_2 \left[1 + \frac{m g_2}{4\pi^2} \left(\Lambda - \frac{\pi}{2}\sqrt{-mE - i\epsilon}\right)\right]^{-1}\,. \tag{2.32}$$

Generally, the amplitude $\mathcal{A}$ will depend on the energies and momentum of the four external particle lines. It is called an *off-shell amplitude* because the energy k_0 of an external line with momentum $\vec{k}$ does not need to be equal to its physical value $k^2/2m$. However, physical observables can only be found when the amplitude is evaluated using the physical values for every external line, called the *on-shell amplitude* $\mathcal{T}$. It is most convenient to work in the center-of-mass frame, in which the two incoming lines have opposite momenta $\pm\vec{k}$, and the outgoing lines momenta $\pm\vec{p}$. Therefore, the amplitude $\mathcal{A}$ can depend on only $\vec{k}$, $\vec{p}$, and the four off-shell external energies. However, for the local effective field theory, where the only interaction is the contact interaction, at which momentum and energy are both conserved, the amplitude is only dependent on the total momentum and the total energy E of the system. In the center-of-mass frame, where the total momentum is by definition zero, it is only a function of E. In fact, we used these assumptions already in the above calculation of

$\mathcal{A}(E)$. At the on-shell point we have $E = 2(k^2/2m) = 2(p^2/2m)$, which would require that $p = k$. Therefore the T-matrix element for this two-body scattering is

$$\mathcal{T}(k) = \mathcal{A}(E = k^2/m)\,. \tag{2.33}$$

The conventional scattering amplitude $f_k(\theta)$ for two-body scattering through an angle θ is proportional to the on-shell amplitude:

$$f_k(\theta) = \frac{m}{8\pi}\mathcal{T}(k)\,, \tag{2.34}$$

where m is the mass of the particle. The $k \to 0$ limit of f_k, as defined in Eq. (2.4), gives the scattering length:

$$a = -\frac{m}{8\pi}\mathcal{T}(0) = -\frac{m}{8\pi}\mathcal{A}(0)\,. \tag{2.35}$$

We can now use our result for the two-body scattering amplitude, Eq. (2.32), in the $E \to 0$ limit in order to eliminate the coupling constant g_2 in favor of the scattering length a:

$$a = \frac{mg_2}{8\pi}\left(1 + \frac{mg_2\Lambda}{4\pi^2}\right)^{-1}\,. \tag{2.36}$$

Solving for g_2 gives

$$g_2 = \frac{8\pi a}{m}\left(1 - \frac{2a\Lambda}{\pi}\right)^{-1}\,. \tag{2.37}$$

For a fixed ultraviolet cutoff Λ, Eq. (2.37) can be used to evaluate the value to which g_2 must to be tuned in order to reproduce an experimentally measured scattering length a. Conversely, for a given a, g_2 can be interpreted as a running coupling constant dependent on the momentum scale Λ. It is also interesting to note that for a large $\Lambda \gg 1/|a|$, the coupling constant g_2 is always negative, no matter the sign of a.

Substituting Eq. (2.37) into our result for the off-shell amplitude $\mathcal{A}$ now completes the so called *renormalization process*, whereby we eliminate the ultraviolet divergences:

$$\mathcal{A}(E) = \frac{8\pi}{m}\frac{1}{-1/a + \sqrt{-mE - i\epsilon}}\,. \tag{2.38}$$

In this simple two-body problem, the renormalization eliminates the dependence on Λ immediately. Normally, we should expect this dependence to only be suppressed in higher order terms proportional to powers of $1/(a\Lambda)$ or E/Λ^2, which would disappear in taking the limit $\Lambda \to \infty$. Substituting in the on-shell point, $mE = k^2$, in order to find the on-shell T-matrix gives

$$\mathcal{T}(k) = \frac{8\pi}{m}\frac{1}{-1/a - ik}\,, \tag{2.39}$$

which, along with the definition in Eq. (2.34), reproduces exactly the low-energy S-wave scattering amplitude, Eq. (2.11). Therefore, the EFT has reproduced all of the low-energy physics for two-body scattering with a large scattering length.

2.2.2 Effective Quantum Mechanical Theories

Rather than using an EFT, systems of non-relativistic particles interacting through short-range potentials can also be easily described through more familiar quantum mechanical theories. We therefore return to the Schrödinger equation in the Hamiltonian formalism with two-body interactions defined through an effective potential $V_{\text{eff}}(r)$, as was briefly introduced at the beginning of the previous subsection. Recall that the effective potential depends on a set of parameters C_i which are analogous to the coupling constants $(g_2, h_2, \ldots)$ of the EFT Lagrangian. These parameters can likewise be tuned in order to reproduce physical observables.

Depending on the number of parameters included, the effective potential can reproduce the low-energy behavior of the system with an arbitrary level of accuracy proportional to powers of the low-momentum scale M_{low} over the high-momentum scale M_{high}. The theory is valid up to a momentum M_{high} at which the errors become of order one. Therefore, if n coupling parameters are used, the error will be of the order $(M_{low}/M_{high})^n$. For example, in the two-body system with a large scattering length, $a \sim 1/M_{low}$, compared to the range of the interaction, $R \sim 1/M_{high}$, to leading order only one coupling parameter C_0 would be needed, which can be tuned to reproduce this scattering length. Once this is done, we can predict other low-energy observables with errors of the order M_{low}/M_{high}. At next-to-leading order, we would require a second coupling parameter, which can be tuned to reproduce the effective range of the interaction.

In this work, we explore systems for which the two-body interactions have large scattering lengths. Due to the success of EFTs in describing such systems [Br06b], we have chosen to generate our effective potential directly from the corresponding EFT Lagrangian, Eq. (2.28). This is equivalent to using field-theoretic language for the problem at hand. This leads to a separable potential made up of contact interactions in a momentum expansion. The two-body S-wave effective potential to next-to-leading order is therefore:

$$\langle \vec{p} \mid V_{eff} \mid \vec{p}' \rangle = C_0 + C_2(p^2 + p'^2) + \ldots , \tag{2.40}$$

where $\vec{p}$ and $\vec{p}'$ are the relative momenta of the incoming and outgoing particles, respectively. The dots indicate higher order momentum dependent interactions which will not be needed in this work. As in the EFT approach, calculating observables with this potential leads to ultraviolet divergences, due to high-energy effects, which must be regulated. Thus, the exact form of the potential will depend on the choice of *regularization scheme*. Of course, the low-energy observables must be independent of the regularization scheme, and one can choose the scheme most convenient for calculations. The specific choice of regularization scheme and its effects on the effective potential will be dealt with in detail in the following chapters.

This approach was chosen because it is especially well suited in solving the three-body system. The solution of the three-body non-relativistic quantum mechanical problem was derived by Faddeev in the 1960's [Fa61]. In the following chapter we

give a detailed derivation of the Faddeev equations, along with the specific form needed to solve the $2n$ halo nucleus problem.

Chapter 3

The Non-Relativistic Three-Body Problem

In this chapter, we detail the formalism needed in calculating observables in the non-relativistic three-body problem. The approach was first formulated by Faddeev in the 1960's [Fa61], and thus, the resulting coupled equations are the well known *Faddeev equations*. In the following section, we give a brief but thorough derivation of the Faddeev equations in operator form, first for an arbitrary three-body system (Sec. 3.1.1), then specializing to the $2n$ halo nucleus system (Sec. 3.1.2). For calculations, these equations will need to be projected onto a suitable basis state, which we create from the Jacobi momenta. We introduce the Jacobi momenta in Sec. 3.2.1, and describe how to build a complete set of basis states from the partial wave projected Jacobi momenta in Sec. 3.2.2. We then show the form of these Jacobi states for the two possible choices of two-body subsystems found in the $2n$ halo system in Sec. 3.2.3. Our goal is to derive a coupled set of integral equations with which we can compute low-energy observables of $2n$ halo nuclei. This set of coupled integral equations is shown in Sec. 3.3.

3.1 The Faddeev Equations

The Faddeev equations are used to compute three-body observables in a quantum mechanical framework. In the following subsection we give a brief derivation of this set of coupled equations starting from the Schrödinger equation. We follow that up by deriving the specific form of the Faddeev equations needed to solve the $2n$ halo nucleus problem.

3.1.1 The Faddeev Equations for an Arbitrary Three-Body System

Faddeev's idea was to decompose the full wave function Ψ into components ψ_i related to the two-body subsystems [Fa61]. In this way the contributions of the two-body potentials can be treated in a disconnected way. We start from the Schrödinger equation for the three-body system with only two-body potentials, which can be written in an integral equation form:

$$\Psi = \frac{1}{E - H_0} \sum_i V_i \Psi, \tag{3.1}$$

where the summation is over the three particles (which we refer to as particles i, j, and k), V_i refers the the two-body interaction between particles j and k,[1] and H_0 is the total kinetic energy of the three-body system. Faddeev showed that one could first sum up all the interactions within each two-body subsystem to infinite order by decomposing Ψ into Faddeev components:

$$\Psi = \sum_i \psi_i, \tag{3.2}$$

where

$$\psi_i \equiv G_0 V_i \Psi, \tag{3.3}$$

and we use the normal definition for the free three-body propagator:

$$G_0 \equiv \frac{1}{E - H_0}. \tag{3.4}$$

By inserting Eq. (3.2) into Eq. (3.3), we find:

$$\psi_i = G_0 V_i \psi_i + G_0 V_i \sum_{j \neq i} \psi_j. \tag{3.5}$$

We can then single out one two-body subsystem by bringing the ψ_i component to one side and solving:

$$\psi_i = (1 - G_0 V_i)^{-1} G_0 V_i \sum_{j \neq i} \psi_j. \tag{3.6}$$

The operator in front can be iterated and expanded to all orders, and one finds a familiar form for the two-body t-matrix. This is obvious from the Lippmann-Schwinger equation:

$$t_i = V_i + V_i G_0 t_i \tag{3.7}$$

[1] The spectator notation is used throughout. In this notation the index refers to the spectator particle of the three-body system.

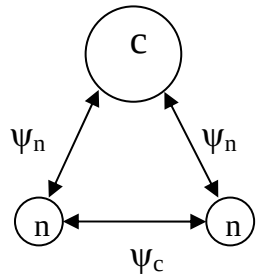

Figure 3.1: The Faddeev components of a $2n$ halo nucleus corresponding to their two-body subsystems

or

$$t_i = (1 - V_i G_0)^{-1} V_i. \tag{3.8}$$

Therefore, we end up with the coupled Faddeev equations:

$$\psi_i = G_0 t_i \sum_{j \neq i} \psi_j. \tag{3.9}$$

3.1.2 The Faddeev Equations for $2n$ Halo Nuclei

For the case of $2n$ halo nuclei, made up of a core c and two neutrons n, there are two types of two-body subsystems: two c-n subsystems and one n-n subsystem, with Faddeev components ψ_{n_1}, ψ_{n_2}, and ψ_c, respectively (see Fig. 3.1). The c-n subsystems' interaction t_n is characterized through the potential V_n, while the n-n interaction t_c by the corresponding potential V_c. Due to the symmetry of the two c-n subsystems, assuming they have the same interaction, the Faddeev equations can be simplified through the use of a permutation operator P which permutes the two neutrons. The application of P on any of the t-operators t_i or the potentials V_i will leave them unchanged. However, the wave functions and their components must be antisymmetric under the permutation of the two neutrons:

$$P\Psi = -\Psi \quad \text{and} \quad P\psi_{n_{1/2}} = -\psi_{n_{2/1}}. \tag{3.10}$$

Therefore, the ψ_{n_2} component can be written in terms of ψ_{n_1}, and we need only two of the Faddeev components. We are left with two coupled equations (dropping the subscript on n_1):

$$\psi_n = -G_0 t_n P \psi_n + G_0 t_n \psi_c \tag{3.11}$$

and

$$\begin{aligned} \psi_c &= G_0 t_c \psi_n - G_0 t_c P \psi_n \\ &= 2 G_0 t_c \psi_n, \end{aligned} \tag{3.12}$$

where the last step depends on an expansion in a suitable basis state (see Sec. 3.2 and 3.3). The full three-body wave function is then written as

$$\Psi = (1 - P)\psi_n + \psi_c. \tag{3.13}$$

The coupled Faddeev equations can most easily be solved as a large matrix equation:

$$\begin{bmatrix} \psi_n \\ \psi_c \end{bmatrix} = \begin{bmatrix} -G_0 t_n P & G_0 t_n \\ 2G_0 t_c & 0 \end{bmatrix} \begin{bmatrix} \psi_n \\ \psi_c \end{bmatrix}. \tag{3.14}$$

However, if we are only interested in finding the binding energies and not in the wave function, we can eliminate the ψ_c component by substituting Eq. (3.12) into Eq. (3.11) to obtain a large integral equation:

$$\psi_n = -G_0 t_n P \psi_n + 2G_0 t_n G_0 t_c \psi_n. \tag{3.15}$$

The energies, $E < 0$, for which this equation has a nontrivial solution or, equivalently, for which the kernel matrix in Eq. (3.14) has an eigenvalue equal to 1 are binding energies of the three-body system.

In order for observables to be calculated, the Faddeev equations must now be projected onto a suitable set of basis states.

3.2 The Jacobi Momentum States

The Jacobi momenta are used to describe the motion of three-body systems. This eliminates the motion of the center of mass in favor of a two-body subsystem motion and the motion of the spectator particle in relation to the two-body subsystem. These coordinates are then used in their partial wave projected form to create a complete set of basis states onto which the Faddeev components of the wave function are then projected.

3.2.1 Jacobi Momenta for an Arbitrary Three-Body System

For three particles (i, j and k) with momenta $\vec{k}_i$ and masses m_i, the Jacobi momenta are defined as:

$$\vec{p}_i = \mu_{jk} \left(\frac{\vec{k}_j}{m_j} - \frac{\vec{k}_k}{m_k} \right), \tag{3.16}$$

$$\vec{q}_i = \mu_{i,jk} \left(\frac{\vec{k}_i}{m_i} - \frac{\vec{k}_j + \vec{k}_k}{m_j + m_k} \right), \tag{3.17}$$

and

$$\vec{K} = \vec{k}_i + \vec{k}_j + \vec{k}_k, \tag{3.18}$$

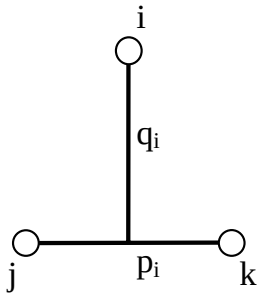

Figure 3.2: General Jacobi momenta

where $\vec{p}_i$ is the relative center-of-mass momentum of the two-body subsystem, composed of particles j and k, $\vec{q}_i$ is the momentum of particle i relative to the center of mass of the two-body subsystem (see Fig. 3.2), and $\vec{K}$ is the total three-body momentum (which is zero in the center-of-mass frame, $\vec{K} = 0$).[2] The two-body and three-body reduced masses are:

$$\mu_{jk} = \frac{m_j m_k}{m_j + m_k}, \tag{3.19}$$

and

$$\mu_{i,jk} = \frac{m_i(m_j + m_k)}{m_i + m_j + m_k}. \tag{3.20}$$

Also, the total mass of the system is obviously

$$M' = m_i + m_j + m_k. \tag{3.21}$$

The free three-body Hamiltonian is the kinetic energy of the three-body system, and thus in terms of the Jacobi momenta has the form

$$H_0 = \frac{K^2}{2M'} + \frac{p_i^2}{2\mu_{jk}} + \frac{q_i^2}{2\mu_{i,jk}}. \tag{3.22}$$

However, we will work in the center-of-mass frame, for which $\vec{K} = 0$. The relations for other spectator particles can be easily obtained through a cyclic permutation of ijk in Eqs. (3.16 - 3.22).

[2]The spectator notation is used throughout. In this notation the index refers to the spectator particle of the three-body system. The exceptions are the variables which refer to individual particles, for example, the individual particle momenta $\vec{k}_i$, the individual masses m_i, as well as the various reduced masses μ_{ij} or $\mu_{i,jk}$.

3.2.2 The Jacobi Momentum Basis States

The Jacobi momenta can be used to define a complete basis of vector Jacobi states:

$$| \vec{pq}\rangle_i \equiv | \vec{p}_i\vec{q}_i\rangle. \tag{3.23}$$

One constructs a partial wave projected basis state from these states, following the presentation by Glöckle [Gl83], which is then used in the application to the Faddeev equations:

$$\begin{aligned} | pq\mathcal{J}\rangle_i &\equiv | p_i q_i \mathcal{J}_i\rangle \\ &\equiv | pq[(ls)j(\lambda\sigma)\mathbf{j}]JM_J(t\mathbf{t})TM_T\rangle_i, \end{aligned} \tag{3.24}$$

where $\mathcal{J}_i$ is used as an abbreviation for all the discrete quantum numbers. The various quantum numbers are defined in the following list:

- $p = |\vec{p}_i|,\ q = |\vec{q}_i|$
- l = the coupled orbital angular momentum of the two-body subsystem
- s = the coupled spin of the two-body subsystem
- j = the coupling of l and s
- $\lambda = l_i$ = the orbital angular momentum of particle i relative to the two-body subsystem
- $\sigma = s_i$ = the spin of particle i
- $\mathbf{j}$ = coupling of λ and σ
- J = total angular momentum of the three-body system, i.e. the coupling of j to $\mathbf{j}$ (with z-component M_J)
- t = isospin of the two-body subsystem
- $\mathbf{t} = t_i$ the isospin of particle i
- T = total three-body isospin, i.e. the coupling of t to $\mathbf{t}$ (with z-component M_T)

This basis state is complete:

$$\sum_{\mathcal{J}} \int_0^\infty dp\ p^2 \int_0^\infty dq\ q^2 \mid pq\mathcal{J}\rangle\langle pq\mathcal{J} \mid = 1, \tag{3.25}$$

and accordingly normalized:

$${}_i\langle pq\mathcal{J} \mid p'q'\mathcal{J}'\rangle_i = \frac{\delta(p-p')}{pp'}\frac{\delta(q-q')}{qq'}\delta_{\mathcal{J}\mathcal{J}'}. \tag{3.26}$$

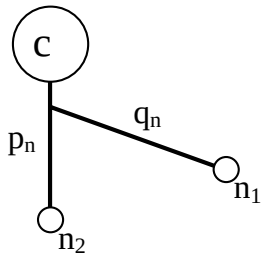

Figure 3.3: The Jacobi momenta corresponding to the c-n subsystem

It is then suitable for the expansion of the Faddeev component ψ_i:

$$\mid \psi\rangle_i = \sum_{\mathcal{J}} \int_0^\infty dp\ p^2 \int_0^\infty dq\ q^2 \mid pq\mathcal{J}\rangle\langle pq\mathcal{J} \mid \psi\rangle_i. \tag{3.27}$$

3.2.3 Jacobi States for $2n$ Halo Nuclei

We can now calculate the specific Jacobi momenta results for the two different halo nuclei subsystems. First, looking at the momenta related to the c-n subsystem (see Fig. 3.3), we can write the reduced mass relations:

$$\mu_{nc} = \frac{A}{A+1}m \qquad \text{and} \qquad \mu_{n,nc} = \frac{A+1}{A+2}m, \tag{3.28}$$

where A is the number of nucleons in the core, and m is the nucleon mass. The Jacobi momenta are (recall, we set $n_1 \to n$ in Eqs. (3.11 - 3.15))

$$\vec{p}_n = -\frac{1}{A+1}\left(\vec{k}_c - A\vec{k}_{n_2}\right) \tag{3.29}$$

and

$$\vec{q}_n = \frac{1}{A+2}((A+1)\vec{k}_{n_1} - \vec{k}_{n_2} - \vec{k}_c). \tag{3.30}$$

The corresponding free Hamiltonian is

$$H_0^n = \frac{p_n^2}{2\mu_{nc}} + \frac{q_n^2}{2\mu_{n,nc}} = \frac{A+1}{2Am}p_n^2 + \frac{A+2}{2m(A+1)}q_n^2. \tag{3.31}$$

Next, for the momenta related to the n-n subsystem (see Fig. 3.4), the relevant reduced masses:

$$\mu_{nn} = \frac{1}{2}m \qquad \text{and} \qquad \mu_{c,nn} = \frac{2A}{A+2}m, \tag{3.32}$$

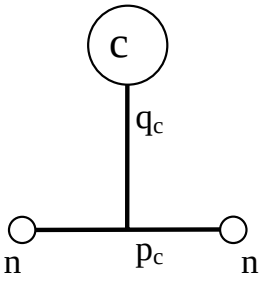

Figure 3.4: The Jacobi momenta corresponding to the n-n subsystem

lead to the Jacobi momenta

$$\vec{p}_c = \frac{1}{2}(\vec{k}_{n_1} - \vec{k}_{n_2}) \tag{3.33}$$

and

$$\vec{q}_c = \frac{1}{A+2}\left(2\vec{k}_c - A(\vec{k}_{n_1} + \vec{k}_{n_2})\right). \tag{3.34}$$

The corresponding Hamiltonian is

$$H_0^c = \frac{p_c^2}{2\mu_{nn}} + \frac{q_c^2}{2\mu_{c,nn}} = \frac{p_c^2}{m} + \frac{A+2}{4Am}q_c^2. \tag{3.35}$$

One important property of these Jacobi states is their behavior under the permutation operator P. Because the two neutrons have opposite spins, for the $\mid pq\mathcal{J}\rangle_c$ state, one finds:

$$P \mid pq\mathcal{J}\rangle_c = - \mid pq\mathcal{J}\rangle_c. \tag{3.36}$$

This relation justifies the simplification done in the second line of the Faddeev equation Eq. (3.12), as the permutation operator will naturally be next to a $\mid pq\mathcal{J}\rangle_c$ state when an expansion is done (see Sec. 3.3).

The behavior of the $\mid pq\mathcal{J}\rangle_n$ state under application of P requires that we explicitly keep track of the positions of the two neutrons in the notation. For the S-wave state with a spinless core we find:

$$P \mid pq\mathcal{J}\rangle_{n_1} = \mid pq\mathcal{J}\rangle_{n_2}. \tag{3.37}$$

This relation becomes useful in the expansion of the Faddeev equations.

3.3 The Faddeev Equations in the Jacobi Momentum States

Now that we have found a suitable set of basis states, we can return to the Faddeev equations for $2n$ halo nuclei, Eqs. (3.11, 3.12). We project these Faddeev equations

onto the partial wave momentum space. We must now expand the terms using the completeness relation, Eq. (3.25). For brevity we drop $\mathcal{J}$ as well as the summation over $\mathcal{J}$ because the discrete quantum numbers will be specifically chosen for our halo nuclei:

$$\begin{aligned}
{}_n\langle pq\mathcal{J} \mid \psi\rangle_n &= {}_n\langle pq\mathcal{J} \mid -G_0 t_n P \mid \psi\rangle_n + {}_n\langle pq\mathcal{J} \mid G_0 t_n \mid \psi\rangle_c \\
&= \int_0^\infty dp' p'^2 dq' q'^2 \int_0^\infty dp'' p''^2 dq'' q''^2 \, {}_n\langle pq \mid G_0 t_n \mid p'q'\rangle_n \\
&\quad \times \Big[{}_n\langle p'q' \mid -P \mid p''q''\rangle_n \; {}_n\langle p''q'' \mid \psi\rangle_n \\
&\quad + {}_n\langle p'q' \mid p''q''\rangle_c \; {}_c\langle p''q'' \mid \psi\rangle_c \Big], \qquad (3.38)
\end{aligned}$$

$$\begin{aligned}
{}_c\langle pq\mathcal{J} \mid \psi\rangle_c &= {}_c\langle pq\mathcal{J} \mid 2G_0 t_c \mid \psi\rangle_c \\
&= 2\int_0^\infty dp' p'^2 dq' q'^2 \int_0^\infty dp'' p''^2 dq'' q''^2 \, {}_c\langle pq \mid G_0 t_c \mid p'q'\rangle_c \\
&\quad \times {}_c\langle p'q' \mid p''q''\rangle_n \; {}_n\langle p''q'' \mid \psi\rangle_n. \qquad (3.39)
\end{aligned}$$

Here we see that the coupled integral equations both have a similar form, with a kernel comprised of T-matrix and overlap-matrix elements.

These coupled Faddeev equations form the starting point for exploring low-energy observables in $2n$ halo nuclei, for example, the three-body binding energies and various mean square radii can be found. Next, the two-body interactions must be suitably described by a proper choice of T-matrix, and the overlap-matrix elements must be solved for specific $2n$ halo systems. In the following chapters, we will show the results using a T-matrix derived from a leading order (LO) and next-to-leading order (NLO) S-wave effective potential (Ch. 4 and Ch. 5, respectively).

Chapter 4

Three-Body Halo Nuclei to Leading Order

We now come to the leading order calculations for three-body halo nuclei[1]: a special class of nuclear systems which offer the possibility of exploring universal behavior [Ri94, Zh93, Hans95, Ta96, Je04]. Halo nuclei consist of a tightly bound core and a "halo" of lightly bound nucleons. They are characterized by their large nuclear radius compared to the radius of the core. Equivalently, the separation energy of the halo nucleons is small compared to the excitation energy of the core. This separation of scales allows for the use of effective theories, where one can assume the core to be a structureless particle, and treat the nucleus as a few-body system of the core and the valence nucleons, which interact through pair-wise potentials dominated by their large S-wave scattering lengths.

The first application of effective field theory methods to halo nuclei was carried out in Refs. [Ber02, Bed03b], where the neutron-alpha system ("^{5}He") was considered. More recent studies have focused on the consistent inclusion of the Coulomb interaction in two-body halo nuclei such as the proton-alpha [Ber09] and alpha-alpha systems [Hi08]. Three-body halo nuclei composed of a core and two valence neutrons are of particular interest due to the possibility of these systems to display the Efimov effect [Ef70]. Efimov found that in three-body systems of non-relativistic particles, if at least two of the three pairs of particles have a large scattering length $|a|$ compared to the range R of the interaction, there occurs a sequence of three-body bound states whose binding energies are spaced geometrically between $\hbar^2/mR^2$ and $\hbar^2/ma^2$. The number of bound states grows to infinity, with an accumulation point at the three-body scattering threshold, in the limit $\pm a \to \infty$. The sequence of three-body bound states have universal properties that are independent of the details of the two-body potential at short distances.

The first experimental evidence for Efimov states in ultracold Cesium atoms has recently been found through their signature in three-body recombination rates [Kr06].

[1]The majority of this chapter has been published in [Ca08].

This signature could be unraveled by varying the scattering length a over several orders of magnitude using a Feshbach resonance. For halo nuclei, the interaction strength can not easily be varied and one has to look for different signatures of the Efimov effect. Since the ground state of a halo nucleus can not be uniquely identified as an Efimov state for fixed a, it is customary to look for excited states that have the Efimov character. One can then consider a halo nucleus to display the Efimov effect if it has at least one excited state with universal properties.

In this chapter, we explore the occurrence of the Efimov effect and its well known universal properties for $2n$ halo nuclei with a core of spin zero using an effective potential. We start by deriving the two-body S-wave T-matrix from our leading order effective potential (Sec. 4.1). In this process, we define the renormalization condition which tunes our coupling constant to reproduce the scattering length. In Sec. 4.2, we use this two-body result in the three-body problem, deriving the coupled Faddeev integral equations with which we can solve the $2n$ halo nucleus problem. We then give a short overview of the universal properties of the Efimov effect in $2n$ halo-like systems with arbitrary core mass and scattering lengths (Sec. 4.3.1). We also explore which known $2n$ halo nuclei have the possibility of displaying the Efimov effect (Sec. 4.3.2). From the earliest studies of halo nuclei, ^{20}C has been suggested as a good candidate for Efimov states [Fed94], with future theoretical work supporting this prediction [Amo96, Maz00]. We critically examine these earlier studies and perform an improved analysis in the framework of an effective theory (Sec. 4.3.3). The uncertainties of our leading order analysis are quantified through error bands. In the final part of this chapter, we focus on the structure of $2n$ halo nuclei. In particular, we calculate their matter form factors (Sec. 4.4.2), various radii, and two-neutron opening angles (Sec. 4.4.3). We close the chapter with conclusions and a brief outlook.

4.1 The Leading Order Effective Potential

For our study, we choose the effective quantum mechanics framework of Refs. [Pl05, Pl04a, Pl04b] which is equivalent to using field-theoretic language for the problem at hand. The short-range interactions characteristic of halo nuclei are then described using an effective interaction potential. The low-energy behavior of the system can be reproduced with a level of accuracy proportional to powers of the low-momentum scale M_{low} over the high-momentum scale M_{high}. The theory is valid up to a momentum M_{high} at which the errors become of order one. For example, the two-body interaction of halo nuclei can be characterized by their large scattering length, $a \sim 1/M_{low}$, and their effective range, $r_0 \sim 1/M_{high}$. Such systems need to leading order one coupling parameter C_0 for each pair interaction tuned to reproduce the scattering length. The effective range of the interaction enters at next-to-leading order. For $a > 0$, there is a two-body bound state, and the binding energy can be found through the universal

formula:

$$B_2 = \frac{\hbar^2}{2\mu a^2} + \dots , \tag{4.1}$$

where μ is the reduced mass of the two-body system. The dots indicate corrections of the order $\sqrt{2\mu B_2}/M_{high} \sim r_0/a$.

For the large separation of scales involved in halo nuclei, zero-range interactions can be used in constructing the effective interaction potential. This leads to a separable potential made up of contact interactions in a momentum expansion. The two-body S-wave potential to leading order is

$$\langle \vec{p} \mid V_{eff} \mid \vec{p}' \rangle = C_0\, g(p) g(p') + \dots , \tag{4.2}$$

where the dots indicate higher order momentum dependent interactions which we will deal with to next-to-leading order in Ch. 5. $g(p)$ is the regulator function (sometimes called the form factor) of the theory. Of course, the low-energy observables must be independent of the regularization scheme, and one can choose the scheme most convenient for calculations. We use a momentum cutoff scheme, multiplying the coupling parameter with a Gaussian regulator function

$$g(p) = \exp\left(-\frac{p^2}{\Lambda^2}\right), \tag{4.3}$$

where Λ is the cutoff parameter. This regulator function obviously suppresses the contributions of momenta $p, p' \gg \Lambda$, where the effective potential would break down and no longer be valid. A natural choice for the value of Λ is therefore $\Lambda \sim M_{high}$, but observables are independent of Λ after renormalization. The cutoff is inversely related to the interaction radius (see [Ef90] and references within), thus taking the limit $\Lambda \to \infty$ is equivalent to taking the range of our potential to zero.

One convenient property of a separable potential is that the two-body scattering amplitude, known as the T-matrix, can be solved exactly. It is defined by the Lippman-Schwinger equation:

$$\begin{aligned} T(\vec{p},\vec{p}') &\equiv \langle \vec{p} \mid t \mid \vec{p}' \rangle = V(\vec{p},\vec{p}') + \int d^3q\, \frac{V(\vec{p},\vec{q})}{E - \frac{q^2}{2\mu} + i\epsilon} T(\vec{q},\vec{p}') && (4.4)\\ &= C_0\, g(p) g(p') + C_0\, g(p) \int d^3q\, \frac{g(q)}{E - \frac{q^2}{2\mu} + i\epsilon} T(\vec{q},\vec{p}') && (4.5)\\ &= C_0\, g(p) g(p') + C_0\, g(p) B_1, && (4.6) \end{aligned}$$

where in the last line we have defined an intermediate function B_1. When we iterate Eq. (4.5) once, we can by comparison find an iterative relation for B_1:

$$\begin{aligned} B_1 &= C_0\, g(p') \int d^3q\, \frac{g(q)^2}{E - \frac{q^2}{2\mu} + i\epsilon} + C_0\, B_1 \int d^3q\, \frac{g(q)^2}{E - \frac{q^2}{2\mu} + i\epsilon} \\ &= C_0\, g(p') A_1 + C_0\, A_1 B_1, && (4.7) \end{aligned}$$

where we have now defined the integral as a function A_1, which we will return to shortly. First, we can easily solve for B_1:

$$B_1 = \frac{C_0 g(p') A_1}{1 - C_0 A_1}. \tag{4.8}$$

Substituting this back into the Lippmann-Schwinger equation, Eq. (4.6), we find a solution for the T-matrix:

$$T(\vec{p}, \vec{p}') = g(p) g(p') \frac{1}{\frac{1}{C_0} - A_1}. \tag{4.9}$$

Here we see that the T-matrix of a separable potential is itself separable.

We now return to the definition of the A_1 integral, which can be simplified by performing the trivial angular integration:

$$\begin{aligned} A_1 &\equiv \int d^3q \, \frac{g(q)^2}{E - \frac{q^2}{2\mu} + i\epsilon} \\ &= 4\pi 2\mu \int_0^\infty dq \, \frac{q^2 \exp\left(\frac{-2q^2}{\Lambda^2}\right)}{2\mu E - q^2 + i\epsilon}. \end{aligned} \tag{4.10}$$

Since we will be chiefly concerned with bound states, we can assume that $E < 0$ and not only is the $i\epsilon$ unnecessary , we can solve the A_1 integral analytically. The derivation of this relation is found in App. A:

$$A_1 = -2\pi^2 2\mu \left[\frac{\Lambda}{2}\sqrt{\frac{2}{\pi}} - \sqrt{-2\mu E} \exp\left(\frac{2(-2\mu E)}{\Lambda^2}\right) \operatorname{erfc}\left(\frac{\sqrt{2(-2\mu E)}}{\Lambda}\right)\right], \tag{4.11}$$

where $\operatorname{erfc}(x) = 1 - (2/\sqrt{\pi}) \int_0^x \exp(-t^2) dt$ denotes the complementary error function, which will go quickly to 1 for $x \ll 1$. Here one sees that in taking the zero-range limit, $\Lambda \to \infty$, the A_1 integral has a divergent term which must be removed through a proper renormalization.

In the case of two-body systems with a large scattering length a, the coupling constant C_0 can be tuned to reproduce this scattering length. For positive(negative) scattering length there is a bound(virtual) state with energy to leading order described by Eq. (4.1). For bound states, this appears in the T-matrix as a simple pole, and we can now use A_1 to tune $C_0(\Lambda)$ in order to reproduce a (now using units such that $\hbar = c = 1$):

$$\begin{aligned} \frac{1}{C_0} &= A_1(E = -B_2) \\ &= 2\pi^2 2\mu \left[\frac{1}{a} \exp\left(\frac{2}{a^2\Lambda^2}\right) \operatorname{erfc}\left(\frac{\sqrt{2}}{|a|\Lambda}\right) - \frac{\Lambda}{2}\sqrt{\frac{2}{\pi}} \right]. \end{aligned} \tag{4.12}$$

For $|a|\Lambda \gg 1$, the exp and erfc functions both quickly approach 1, and one finds the simpler relations:

$$C_0 = \frac{a}{2\pi^2 2\mu}\left[1 - \frac{a\Lambda}{2}\sqrt{\frac{2}{\pi}}\right]^{-1} \tag{4.13}$$

and

$$a = \frac{2\pi^2 2\mu C_0}{1 + 2\pi^2 2\mu C_0 \frac{\Lambda}{2}\sqrt{\frac{2}{\pi}}}. \tag{4.14}$$

These results are analogous to the findings of EFT using a strong cutoff regularization scheme as seen in Sec. 2.2.1, Eqs. (2.36, 2.37) and in Ref. [Br06b].

With the potential now properly renormalized, we can return to the two-body T-matrix for an S-wave interaction to leading order. By substituting Eqs. (4.11, 4.12) into Eq. (4.9) we find for $E < 0$:

$$\begin{aligned} T(\vec{p},\vec{p}') &= g(p)g(p')\frac{-1}{2\pi^2 2\mu}\left[-\frac{1}{a}\exp\left(\frac{2}{a^2\Lambda^2}\right)\mathrm{erfc}\left(\frac{\sqrt{2}}{|a|\Lambda}\right)\right. \\ &\quad \left. +\sqrt{-2\mu E}\exp\left(\frac{2(-2\mu E)}{\Lambda^2}\right)\mathrm{erfc}\left(\frac{\sqrt{2(-2\mu E)}}{\Lambda}\right)\right]^{-1}. \end{aligned} \tag{4.15}$$

If the cutoff is chosen large compared to all momentum scales involved in the problem: $\Lambda \gg 1/|a|, \sqrt{2\mu E}$, this T-matrix reproduces the usual effective range expansion at leading order.

4.2 The Leading Order Faddeev Equations

The two-body leading order T-matrix derived in the previous section can now be used in the kernel of the Faddeev integral equations found in Sec. 3.3. The aim is to find the bound states of $2n$ halo nuclei, by finding the energies $B_3 = -E > 0$ for which the coupled Eqs. (3.38, 3.39) have a nontrivial solution. We therefore return to the general form of the T-matrix element found in these Faddeev equations. We use units such that $\hbar = c = 1$ and the nucleon mass $m = 1$:

$${}_i\langle pq \mid G_0 t_i \mid p'q'\rangle_i = -G_0^i(p,q;B_3)\ {}_i\langle pq \mid t_i \mid p'q'\rangle_i, \tag{4.16}$$

where, depending on the choice of spectator particle $i = n$ or c, we need to use the proper free Hamiltonian H_0^i (see Sec. 3.2.3, Eqs. (3.31, 3.35)):

$$G_0^n(p,q;B_3) = \left[B_3 + \frac{A+1}{2A}p^2 + \frac{A+2}{2(A+1)}q^2\right]^{-1}, \tag{4.17}$$

$$G_0^c(p,q;B_3) = \left[B_3 + p^2 + \frac{A+2}{4A}q^2\right]^{-1}. \tag{4.18}$$

Recall that A is the mass of the core.

We know that the t_i-operator is derived from the two-body interaction T-matrix in our chosen two-body subsystem. Therefore, it must be diagonal in the quantum numbers of the spectator particle:

$$ {}_i\langle pq \mid t_i \mid p'q' \rangle_i = \frac{\delta(q-q')}{qq'} \; {}_i\langle p \mid t_i \mid p' \rangle_i. \tag{4.19}$$

We can now relate the partial wave projected T-matrix to the LO T-matrix found in the previous section, Eq. (4.15), knowing that $T(\vec{p},\vec{p}') \equiv \langle \vec{p} \mid t \mid \vec{p}' \rangle$, and using the completeness relation (for brevity, we drop the index i on the basis states):

$$ \langle p \mid t_i \mid p' \rangle = \int d^3p_1 \int d^3p_1' \; \langle p \mid \vec{p}_1 \rangle \; T_i(\vec{p}_1,\vec{p}_1') \; \langle \vec{p}_1' \mid p' \rangle. \tag{4.20}$$

The overlap of a vector state onto a partial wave state is calculated with the corresponding spherical harmonics:

$$ \langle p \mid \vec{p}_1 \rangle = \frac{\delta(p_1-p)}{pp_1} \mathrm{Y}_l^{m*}(\hat{p}_1). \tag{4.21}$$

Using the delta functions, the amplitude part of the integrals are trivially done, and thus we can ignore the subscript on $\hat{p}_1$, and $\hat{p}_1'$. However, in order to perform the angular integration, we use a trick. The effective potential used to derive the T-matrix is the S-wave two-body potential. Therefore, in the T-matrix exists a unitary factor related to the Legendre polynomial with $l = 0$:

$$ 1 = P_0(\cos\theta) \equiv P_0(\hat{p}\cdot\hat{p}'). \tag{4.22}$$

Then, we use the corresponding relation between Legendre polynomials and spherical harmonics:

$$ P_l(\hat{p}\cdot\hat{p}') = \frac{4\pi}{2l+1} \sum_{m=-l}^{l} \mathrm{Y}_l^{m*}(\hat{p}')\mathrm{Y}_l^{m}(\hat{p}), \tag{4.23}$$

in order to perform the angular integrations:

$$ \begin{aligned} \langle p \mid t_i \mid p' \rangle &= T_i(\vec{p},\vec{p}') \int d\hat{p} \int d\hat{p}' \; 4\pi \sum_{m''=0}^{0} \mathrm{Y}_l^{m*}(\hat{p})\mathrm{Y}_0^{m''}(\hat{p})\mathrm{Y}_0^{m''*}(\hat{p}')\mathrm{Y}_{l'}^{m'}(\hat{p}') \\ &= 4\pi \; T_i(\vec{p},\vec{p}') \; \delta_{m0}\delta_{l0}\delta_{l'0}\delta_{m'0}. \end{aligned} \tag{4.24}$$

However, we have already assumed that the discrete quantum numbers in the partial wave Jacobi states $\langle p \mid$ were chosen to be S-wave, so that $l = l' = 0$, and therefore $m = m' = 0$.

Also of importance in applying the two-body T-matrix in the context of the three-body Faddeev equations is the relation between the full three-body binding energy B_3 and the two-body subsystem energy E_i. The T-matrix must be calculated at the two-body subsystem energy, which can be found by subtracting the kinetic energy of the spectator particle from the three-body energy $E = -B_3$. We therefore define two-body subsystem energy functions as follows:

$$\tilde{E}_n(q'; B_3) \equiv -2\mu E_n = \frac{2A}{A+1}\left(B_3 + \frac{A+2}{2(A+1)}q'^2\right), \tag{4.25}$$

$$\tilde{E}_c(q'; B_3) \equiv -2\mu E_c = B_3 + \frac{A+2}{4A}q'^2. \tag{4.26}$$

We are now ready to write the final form of the T-matrix elements to be used in the Faddeev integral equations. Using the results found in Eqs. (4.24, 4.19), we write the T-matrix element in the form:

$${}_i\langle pq \mid G_0 t_i \mid p'q'\rangle_i = G_0^i(p, q; B_3)\frac{\delta(q-q')}{qq'}g(p)g(p')t_i(q'; B_3), \tag{4.27}$$

where the propagators $G_0^i(p, q; B_3)$ are defined in Eqs. (4.17, 4.18), and the results of the T-matrix interactions are found in the functions:

$$\begin{aligned} t_n(q'; B_3) &= \frac{1}{\pi}\frac{A+1}{A}\left[-\frac{1}{a_{nc}}\exp\left(\frac{2}{a_{nc}^2\Lambda^2}\right)\mathrm{erfc}\left(\frac{\sqrt{2}}{|a_{nc}|\Lambda}\right)\right. \\ &\quad \left.+\sqrt{\tilde{E}_n(q'; B_3)}\exp\left(\frac{2\tilde{E}_n(q'; B_3)}{\Lambda^2}\right)\mathrm{erfc}\left(\frac{\sqrt{2\tilde{E}_n(q'; B_3)}}{\Lambda}\right)\right]^{-1}, \end{aligned} \tag{4.28}$$

$$\begin{aligned} t_c(q'; B_3) &= \frac{2}{\pi}\left[-\frac{1}{a_{nn}}\exp\left(\frac{2}{a_{nn}^2\Lambda^2}\right)\mathrm{erfc}\left(\frac{\sqrt{2}}{|a_{nn}|\Lambda}\right)\right. \\ &\quad \left.+\sqrt{\tilde{E}_c(q'; B_3)}\exp\left(\frac{2\tilde{E}_c(q'; B_3)}{\Lambda^2}\right)\mathrm{erfc}\left(\frac{\sqrt{2\tilde{E}_c(q'; B_3)}}{\Lambda}\right)\right]^{-1}, \end{aligned} \tag{4.29}$$

where a_{nn} is the n-n, and a_{nc} the n-c scattering lengths.

For most halo nuclei, however, the S-wave scattering length is not as well known as the two-body bound(virtual) state energy. Therefore, we will generally use the two-body energies E_{nn} and E_{nc} as input parameters, from which we can calculate the

scattering length to leading order through Eq. (4.1), $1/a_{ni} = \pm\sqrt{2\mu_{ni}E_{ni}}$, where the $+$ refers to a bound state and the $-$ to a virtual state, $i = n$ or c, and μ_{ni} is the corresponding reduced mass. The difference between the two-body energy and the S-wave scattering length is higher order in the expansion in $M_{low}/M_{high} \sim r_0/|a|$.

Now that we have solved for the T-matrix element using a short-range effective potential to describe the two-body interactions found in halo nuclei, we can derive a form for the coupled Faddeev equations suitable for solving the bound $2n$ halo nucleus problem.

As the next step in the derivation, we require the recoupling of two Jacobi states in an overlap-matrix element of the form:

$$ {}_i\langle pq\mathcal{J} \mid p'q'\mathcal{J}'\rangle_j. \tag{4.30}$$

The evaluation of this overlap-matrix element is at the heart of the three-body problem, however, the derivation is complicated and tedious. A more detailed explanation can be found in App. B. For brevity, we present only the result here:

$$ {}_i\langle pq\mathcal{J} \mid p'q'\mathcal{J}'\rangle_j \;=\; \int_{-1}^{1} dx\, \frac{\delta(p-\tilde{\pi}_j)}{p\tilde{\pi}_j}\frac{\delta(p'-\tilde{\pi}'_j)}{p'\tilde{\pi}'_j}\frac{G_{\mathcal{J}\mathcal{J}'}(qq'x)}{\tilde{\pi}_j^{l}\tilde{\pi}_j^{l'}}, \tag{4.31}$$

where

$$ \tilde{\pi}_j = \sqrt{\left(\frac{\mu_{jk}}{m_k}\right)^2 q^2 + q'^2 + 2\frac{\mu_{jk}}{m_k}qq'x} \tag{4.32}$$

and

$$ \tilde{\pi}'_j = \sqrt{q^2 + \left(\frac{\mu_{ki}}{m_k}\right)^2 q'^2 + 2\frac{\mu_{ki}}{m_k}qq'x}. \tag{4.33}$$

The angular dependence is now found in the x variable, which is the cosine of the angle between q and q'. For more details on the exact form of the function G, we refer the reader to App. B. To leading order, only S-wave basis states are used, and the function G is simply a multiplicative constant.

First we look at the overlap-matrix element corresponding to the swapping of the spectator neutron:

$$ {}_{n_1}\langle pq \mid P \mid p'q'\rangle_{n_1} \;=\; {}_{n_1}\langle pq \mid p'q'\rangle_{n_2}. \tag{4.34}$$

The two-body subsystem in both states is a c-n system, which to leading order is in the S-wave. Therefore, due to the symmetry in the two-body subsystems, all the primed quantum numbers are equal to their unprimed counterparts, for example $l = l' = 0$ and $\sigma = \sigma' = 1/2$. The quantum numbers with a neutron spectator are:

$$ \begin{array}{llll} l=0 & s=1/2 & j=s=1/2 & t=t_c+1/2 \\ \lambda=0 & \sigma=1/2 & \mathbf{j}=\sigma=1/2 & \mathbf{t}=1/2 \\ L=0 & S=0 & J=S=0 & T=t_c+1. \end{array} \tag{4.35}$$

Here we have assumed that we will only look at halo nuclei for which the core has as many or more neutrons as protons. This is true for all of the known $2n$ halo nuclei candidates (for example, ^{11}Li, ^{14}Be, or ^{20}C), except for the triton (where the core is just one proton). Therefore, the isospin of the core t_c will be one half the number of neutrons minus the number of protons in the core, and the additional halo neutrons will then increase the total isospin, leading to the relations $t = t_c + 1/2$ and $T = t_c + 1$. Also, due to the Pauli-exclusion principle, the halo neutrons must have opposite spin, and therefore the total spin of the three-body system must be the same as the core spin, which we have assumed to be zero: $S = s_c = 0$. Using these quantum numbers and the relation for the function G as found in App. B, it is a simple exercise to show that $G = -1/2$, and therefore:

$$ {}_{n_1}\langle pq \mid P \mid p'q' \rangle_{n_1} = -\frac{1}{2}\int_{-1}^{1} dx \, \frac{\delta(p - \tilde{\pi}(q,q'))}{p\tilde{\pi}(q,q')} \frac{\delta(p' - \tilde{\pi}(q',q))}{p'\tilde{\pi}(q',q)}, \tag{4.36} $$

where

$$ \tilde{\pi}(q,q') = \sqrt{\left(\frac{1}{A+1}\right)^2 q^2 + q'^2 + \frac{2}{A+1} qq'x}. \tag{4.37} $$

Next we turn to the overlap-matrix element corresponding to switching the core as spectator for a neutron spectator: ${}_n\langle pq \mid p'q' \rangle_c$. The two-body subsystem of the left-hand state is again the c-n subsystem. Therefore, all the unprimed quantum numbers are exactly the same as those in Eq. (4.35). The other two-body subsystem is now the n-n subsystem, which to leading order is also in the S-wave. The quantum numbers with a core spectator are:

$$ \begin{array}{llll} l' = 0 & s' = 0 & j' = s' = 0 & t' = 1 \\ \lambda' = 0 & \sigma' = 0 & \mathbf{j}' = \sigma' = 0 & \mathbf{t}' = t_c \\ L = 0 & S = 0 & J = S = 0 & T = t_c + 1. \end{array} \tag{4.38} $$

Here we use the same arguments for the spin and isospin numbers as for the c-n case. In this case, using these quantum numbers, we find that $G = 1/2$, and therefore:

$$ {}_n\langle pq \mid p'q' \rangle_c = \frac{1}{2}\int_{-1}^{1} dx \, \frac{\delta(p - \tilde{\pi}_1(q,q'))}{p\tilde{\pi}_1(q,q')} \frac{\delta(p' - \tilde{\pi}_2(q,q'))}{p'\tilde{\pi}_2(q,q')}, \tag{4.39} $$

where

$$ \tilde{\pi}_1(q,q') = \sqrt{\left(\frac{A}{A+1}\right)^2 q^2 + q'^2 + \frac{2A}{A+1} qq'x}, \tag{4.40} $$

and

$$ \tilde{\pi}_2(q,q') = \sqrt{q^2 + \frac{1}{4}q'^2 + qq'x}\,. \tag{4.41} $$

We finally have all the pieces necessary for writing down the Faddeev equations used to solve the bound $2n$ halo nucleus problem. Returning to Eqs. (3.38, 3.39), we substitute in the results for the T-matrix element, Eq. (4.27), and the overlap-matrix elements above. For brevity we define the function $\psi_i(p,q) \equiv {}_i\langle pq \mid \psi\rangle_i$. After performing all of the integrations involving delta functions, we find:

$$\begin{aligned}\psi_n(p,q) &= G_0^n(p,q;B_3)g(p)t_n(q;B_3)\frac{1}{2}\int_0^\infty dq'q'^2\int_{-1}^1 dx \\ &\quad\times\Big[\, g(\tilde{\pi}(q,q'))\psi_n(\tilde{\pi}(q',q),q') + g(\tilde{\pi}_1(q,q'))\psi_c(\tilde{\pi}_2(q,q'),q') \,\Big],\end{aligned} \tag{4.42}$$

$$\begin{aligned}\psi_c(p,q) &= G_0^c(p,q;B_3)g(p)t_c(q;B_3)\int_0^\infty dq'q'^2\int_{-1}^1 dx \\ &\quad\times\, g(\tilde{\pi}_2(q',q))\psi_n(\tilde{\pi}_1(q',q),q').\end{aligned} \tag{4.43}$$

This is a system of coupled homogeneous integral equations with one shifted variable.

However, we can simplify these equations further using a relation between the Faddeev components and the so called spectator functions $F_i(q)$, which represent the dynamics of the core ($i = c$) and the halo neutron ($i = n$), and depend on only one variable:

$$\psi_i(p,q) = G_0^i(p,q;B_3)g(p)t_i(q;B_3)F_i(q). \tag{4.44}$$

Using these spectator functions, to find the bound state of a halo nucleus composed of two valence neutrons and a core with spin zero, the resulting coupled integral equations are simply a generalization of the three-boson equation[2] (see [Pl04a] and references within):

$$\begin{aligned}F_n(q) &= \frac{1}{2}\int_0^\infty dq'q'^2\int_{-1}^1 dx\Big[g\left(\tilde{\pi}(q,q')\right)g\left(\tilde{\pi}(q',q)\right) \\ &\quad\times G_0^n\left(\tilde{\pi}(q',q),q';B_3\right)t_n(q';B_3)F_n(q') \\ &\quad+ g\left(\tilde{\pi}_1(q,q')\right)g\left(\tilde{\pi}_2(q,q')\right) \\ &\quad\times G_0^c\left(\tilde{\pi}_2(q,q'),q';B_3\right)t_c(q';B_3)F_c(q')\Big],\end{aligned} \tag{4.45}$$

$$\begin{aligned}F_c(q) &= \int_0^\infty dq'q'^2\int_{-1}^1 dx\Big[g\left(\tilde{\pi}_1(q',q)\right)g\left(\tilde{\pi}_2(q',q)\right) \\ &\quad\times G_0^n\left(\tilde{\pi}_1(q',q),q';B_3\right)t_n(q';B_3)F_n(q')\Big].\end{aligned} \tag{4.46}$$

[2]In fact, the equations are the same for any bound three-body system of two identical particles and a core with spin zero, which interact through the pair-wise zero-range potentials given in Eq. (4.2).

The three-body binding energies are given by the values of B_3 for which the coupled integral equations have a nontrivial solution. However, the coupled equations are most easily solved by discretizing the variables q and q', and solving the resulting matrix equation:

$$\begin{bmatrix} F_n \\ F_c \end{bmatrix} = \begin{bmatrix} K_{nn} & K_{nc} \\ K_{cn} & 0 \end{bmatrix} \begin{bmatrix} F_n \\ F_c \end{bmatrix}, \tag{4.47}$$

with kernels K_{ij} taken from the coupled Faddeev equations above. Then, the binding energies are given by the values of B_3 for which the kernel matrix has an eigenvalue of 1.

4.3 Universal Properties of Bound States

Three-body halo nuclei composed of a core and two valence neutrons are of particular interest due to the possibility of these systems to display the Efimov effect [Ef70]. Efimov found that in three-body systems of non-relativistic particles, if at least two of the three pairs of particles have a large scattering length $|a|$ compared to the range R of the interaction, there occurs a sequence of three-body bound states whose binding energies are spaced geometrically between $\hbar^2/mR^2$ and $\hbar^2/ma^2$. The number of bound states grows to infinity, with an accumulation point at the three-body scattering threshold, in the limit $\pm a \to \infty$. The sequence of three-body bound states have universal properties that are independent of the details of the two-body potential at short distances.

4.3.1 The Efimov Effect in $2n$ Halo Nuclei

The three-body binding energies are given by the values of B_3 for which the coupled integral equations, Eqs. (4.45, 4.46), have a nontrivial solution, or accordingly the kernel of the matrix equation, Eq. (4.47), has an eigenvalue of 1. In principle, Eqs. (4.45, 4.46) should also include a three-body force term which is required for proper renormalization. However, due to the limit cycle behavior of this three-body force, it is always possible to choose a cutoff where the three-body force vanishes. As a consequence, we can simply drop the three-body force and work with a finite cutoff Λ as in Ref. [Pl04a]. Tuning this cutoff to reproduce a given three-body observable, we can predict other low-energy observables by using the same cutoff [Br06b, Kh72]. The cutoff is inversely related to the interaction radius (see [Ef90] and references within), thus taking the cutoff to infinity is equivalent to taking the range of our potential to zero. It is at this limit that the Thomas collapse [Thom35] will occur and the energy of the three-body ground state will diverge.

The Thomas collapse is closely related to the Efimov effect in that the deepest three-body bound states of the Thomas collapse can be identified with the deepest Efimov states [Adh88]. The sequence of three-body Efimov states can be found from

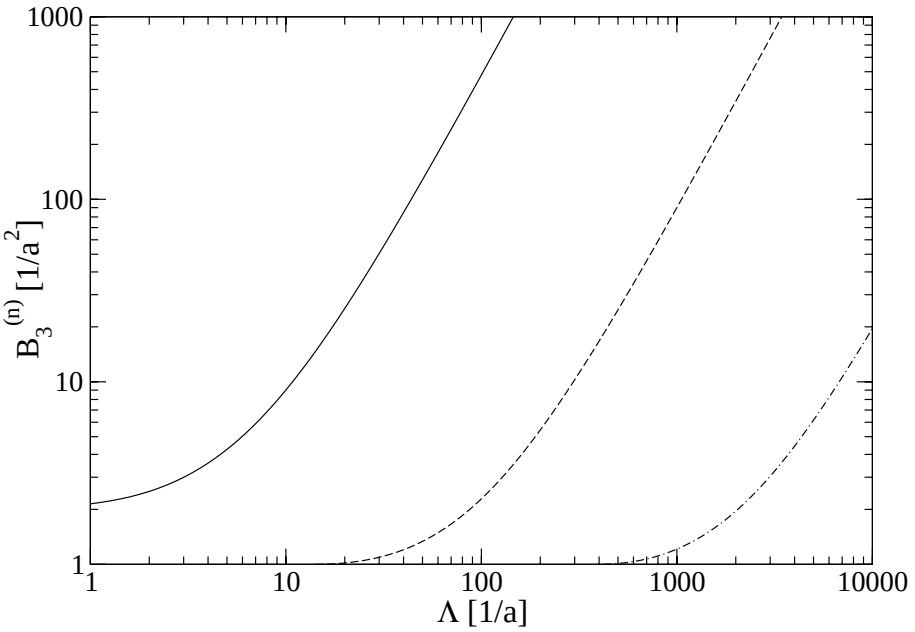

Figure 4.1: The three-body binding energy $B_3^{(n)}$ as a function of the cutoff parameter Λ, for three particles with equal mass. The two-body scattering lengths are such that, $|a_{nn}| = |a_{nc}| = a$, but $a_{nn} < 0$ and $a_{nc} > 0$. Only the first three bound states are shown: $n = 0$ (solid), $n = 1$ (dashed), and $n = 2$ (dotted-dashed).

our integral equations with sufficiently large scattering lengths by finding the spectrum of binding energies for a fixed cutoff. By increasing the cutoff new three-body bound states appear in the spectrum at critical values of Λ, which are geometrically separated. Accordingly, the energies of the deeper bound states increase in magnitude. This dependence of the spectrum of binding energies on the cutoff is seen in Fig. 4.1, where we work in units such that $\hbar = c = 1$ and the nucleon mass $m = 1$. The Thomas effect is seen by the divergence of the deepest bound state energy for $\Lambda \to \infty$. However, the states below the natural cutoff $1/R^2$ are physically irrelevant. They are outside the range of validity of the effective theory and can be ignored.

Conversely, the sequence of three-body Efimov states have universal properties that are insensitive to the details of the two-body potential at short distances, and hence independent of the cutoff. One such property is that for the resonant limit, $a \to \pm\infty$, at which there are infinitely many arbitrarily-shallow three-body bound states, the ratio of the binding energies of neighboring bound states approaches a universal factor λ_0 as the threshold is approached:

$$B_3^{(n)}/B_3^{(n+1)} \longrightarrow (\lambda_0)^2, \tag{4.48}$$

as $n \to +\infty$ with $a = \pm\infty$. This universal scaling factor λ_0 depends on the masses of the particles. In our case, the masses of the two neutrons are equal, $m_1 = m_2$, and the core mass $A = m_3/m_1$. The values of $B_3^{(n)}$ for $n = 1, 2, 3$ as a function of the core

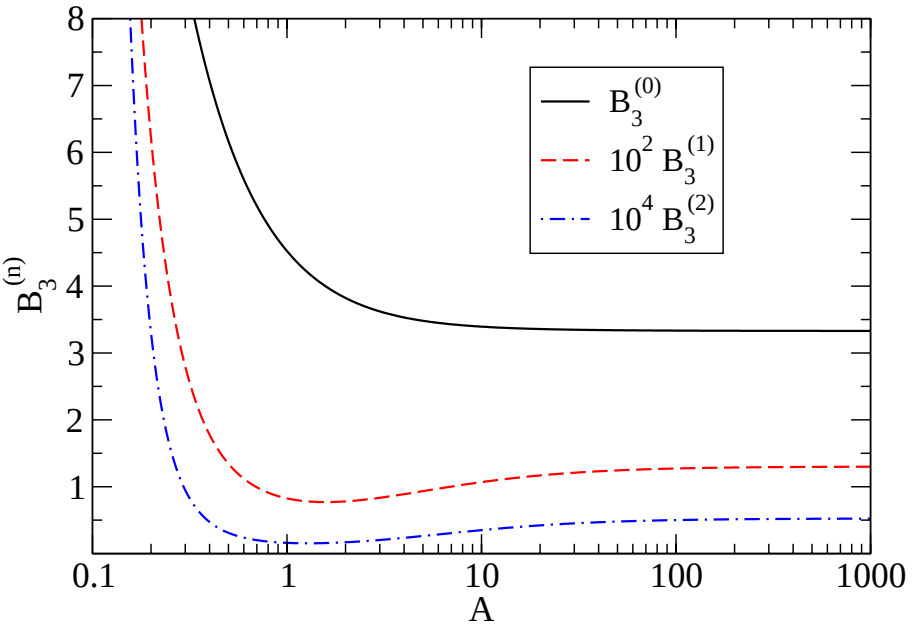

Figure 4.2: Spectrum of three-body bound states, when two of the particles have equal mass $m_1 = m_2$, as a function of the mass ratio $A = m_3/m_1$ in the resonant limit $a \to \pm\infty$. The cutoff parameter was fixed at a value of $\Lambda = 10.0$ (the units of Λ and $B_3^{(n)}$ are arbitrary, for details see text).

mass A are shown in Fig. 4.2 for a finite value of $\Lambda = 10$. Note that because we have taken $a \to \pm\infty$, Λ is given in units of an arbitrary momentum scale κ. All energies are then given in units of κ^2. One interesting feature is the appearance of a minimum in the binding energy. The absence of this minimum in the $B_3^{(0)}$ curve is due to the fact that the magnitude of $B_3^{(0)}$ is near the order of magnitude of Λ, and details of the regularization scheme become important. Also, we see that the binding energy quickly reaches an asymptotic value for very large A, and diverges for $A \to 0$.

The dependence of the discrete scaling factor λ_0 on the core mass A is well known, and an analytic expression for calculating this dependence has been derived (see [Br06b] and references therein). We have confirmed the results of our code by numerically reproducing this core mass dependence of the scaling factor, which can be seen in Fig. 4.3. Due to the small values of the binding energies in comparison to the cutoff Λ for $n > 0$, we find an almost exact reproduction of the discrete scaling factor using the ratio $\sqrt{B_3^{(1)}/B_3^{(2)}}$ taken from the results of Fig. 4.2. The numerical results only start to vary from the analytical results as $A \ll 1$, and the binding energies start to increase dramatically. In particular, the discrete scaling factor is largest for all equal masses, where it has the same value $\lambda_0 \approx 22.7$ as for three identical bosons. In the very large core limit, $A \gg 1$, the discrete scaling factor approaches 15.7. In the vanishing core limit, $A \ll 1$, it approaches 1 as all three-body binding energies diverge.

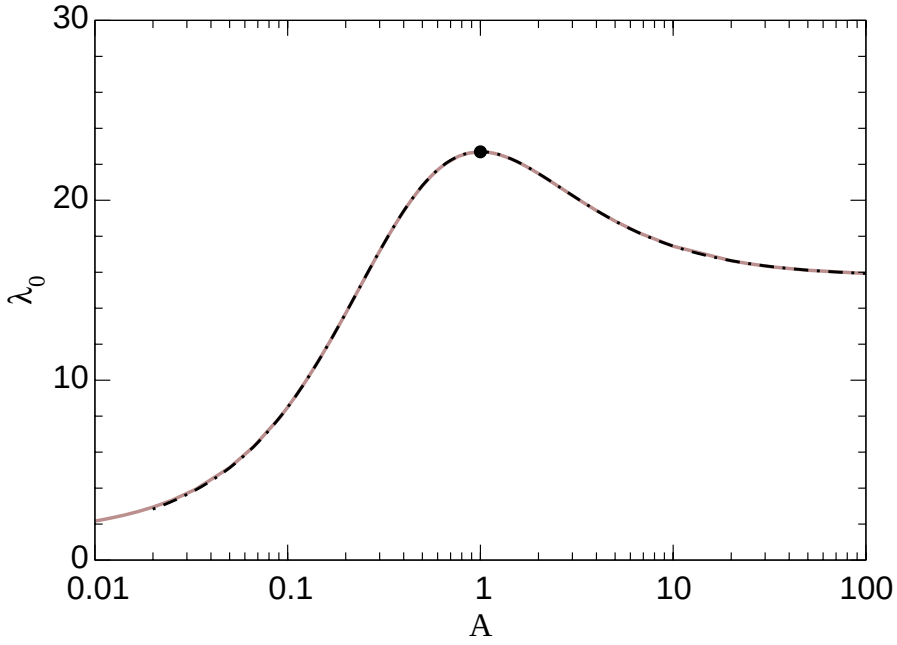

Figure 4.3: Discrete scaling factor λ_0, when two particles have equal mass $m_1 = m_2$, as a function of the mass ratio $A = m_3/m_1$, in the resonant limit $a \to \pm\infty$. Solid line: Result found from solutions of an analytic expression, taken from [Br06b], Fig. 52. Dotted-dashed line: Numerical result found taking the ratio $\sqrt{B_3^{(1)}/B_3^{(2)}}$ from the results of Fig. 4.2. The dot indicates the case of three identical bosons.

4.3.2 Possibility of Efimov Excited States in $2n$ Halo Nuclei

Our main aim in this section is to assess which halo nuclei have the possibility of possessing an excited Efimov state. The ground state energy and the two-body energies can not be predicted by our theory and are taken from experiment. In other words, we would generally like to know what the values of the two-body energies must be, or correspondingly how large the scattering lengths must be, in order to produce an excited Efimov state, knowing the ground state binding energy.

To this end, we construct a parametric region defined by the ratios $\sqrt{E_{nc}/B_3^{(n)}}$ versus $\sqrt{E_{nn}/B_3^{(n)}}$. The boundary curves representing the existence of an excited Efimov state for various values of the core mass are shown in Fig. 4.4. An analogous study was carried out in Ref. [Amo96] (see below). All points which lie within the boundary curve have at least one excited Efimov state above the state with energy $B_3^{(n)}$, while points outside the curve have no excited states above this state. The curve itself is built up of the points for which the $B_3^{(n+1)}$ binding energy is equal to the scattering threshold; i.e. $B_3^{(n+1)} = E_{ni}$ for E_{nn} or E_{nc} bound, where E_{ni} is the larger of E_{nn} and E_{nc}, and $B_3^{(n+1)} = 0$ for E_{nn} and E_{nc} virtual. The boundary curves

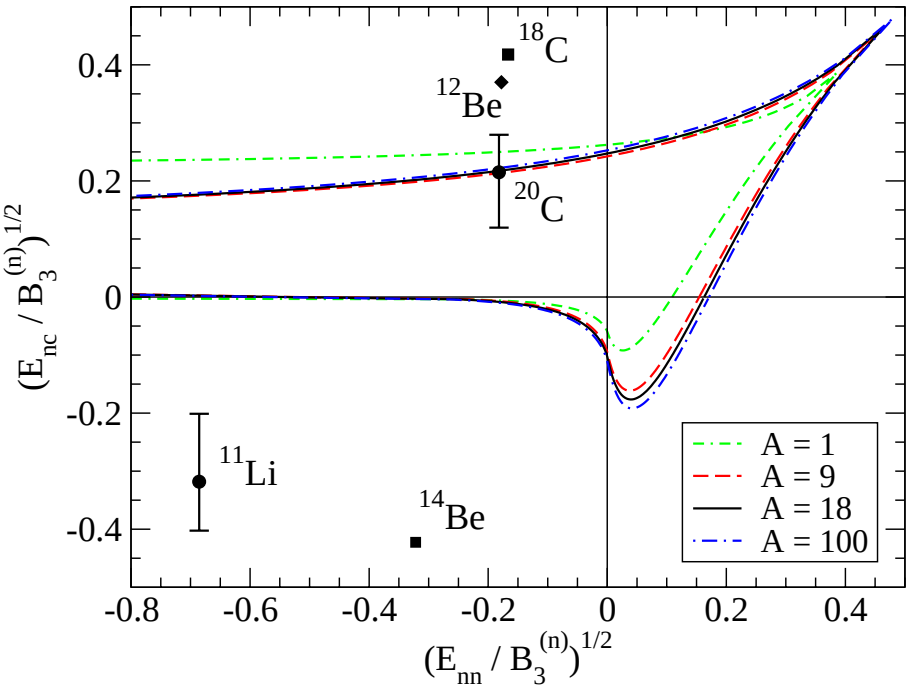

Figure 4.4: Boundary curves in the $\sqrt{E_{nc}/B_3^{(n)}}$ vs. $\sqrt{E_{nn}/B_3^{(n)}}$ plane, where the binding energy of the excited Efimov state $B_3^{(n+1)}$ is exactly at threshold. Negative values on the axes correspond to virtual two-body states. Boundary curves shown for various core masses A =1, 9, 18, and 100. Experimental data shown for ^{20}C, ^{18}C, ^{11}Li, ^{12}Be, and ^{14}Be are taken from Ref. [TUNL].

in Fig. 4.4 were found with $n = 1$ in order to minimize the regulator effects. Due to the scaling symmetry of the sequence of three-body bound states, the nth state can always be interpreted as the ground state and the $(n+1)$th state as the first excited state.[3]

Here it is of interest to note that these results differ from the results found by Amorim, et al. in an analogous study [Amo96] using a hard momentum cutoff rather than the Gaussian regulator scheme. We found that the results agree almost exactly for a core mass equal to the nucleon mass, $A = 1$, but differ significantly for all other values of the core mass. While the qualitative conclusions on the likelihood of Efimov states in $2n$ halo nuclei are the same, the quantitative results are different. In fact, in doing the numerical calculations with a hard cutoff ourselves, we found results that match those presented here.

These results represent the leading order calculations with the effective potential described in Eq. (4.2). The theoretical uncertainty in calculating the binding energy

[3]Because of the regulator effects, the curves found with $n = 0$ are slightly different from the curves in Fig. 4.4. The curves are practically the same for larger values of n, as the numerical values of $B_3^{(n)}$ are much smaller than the cutoff Λ for $n > 0$.

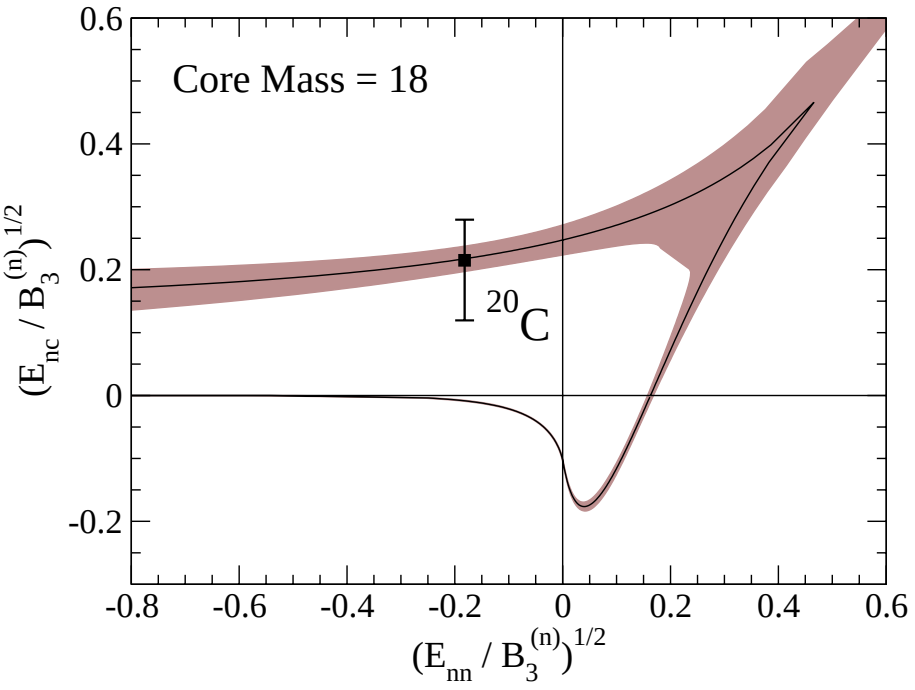

Figure 4.5: Boundary curve in the $\sqrt{E_{nc}/B_3^{(n)}}$ vs. $\sqrt{E_{nn}/B_3^{(n)}}$ plane with leading order error bands. Boundary curve shown for a core mass of $A = 18$ with the experimental data for ^{20}C from Ref. [TUNL, Aud95].

is of the order $\approx r_0/a$, where r_0 is the effective range of the potential, and a is the scattering length. As stated before, the cutoff parameter is related to the inverse of the range of the potential, such that we can approximate $r_0 \approx 1/\Lambda$. However, it is important in this error estimate that the Λ used comes from the result with $n = 0$, the true ground state, rather than $n = 1$. This corresponds to taking the "natural" value for the cutoff Λ. We therefore estimate the leading fractional error of our boundary curves as $\approx \sqrt{2\mu_{ni}E_{ni}}/\Lambda$, for $i = n$ and c, respectively. The resulting boundary curve including leading order error bands, using the case of core mass $A = 18$, is shown in Fig. 4.5. This graph is a good representation of the error bands for other core masses. The uncertainty of our leading order calculation becomes large for values of $\sqrt{E_{nn}/B_3^{(n)} + E_{nc}/B_3^{(n)}}$ near 1 and greater. At this point the low-energy observables approach the order of magnitude of Λ, where the effective potential is no longer a good description of the three-body system.

Now we discuss the implications of Figs. 4.4 and 4.5 for the existence of excited Efimov states in halo nuclei in more detail. The four quadrants of the parametric plane in these figures correspond to the four different types of three-body halo nuclei, determined by the different types of two-body subsystems. The upper-right quadrant corresponds to both the n-n and the n-c subsystems being bound, and is accordingly called *All Bound*. The lower-right quadrant is that in which the n-n subsystem is

bound, but the *n*-*c* subsystem is unbound, and receives the name *Tango* [Ro99]. Of course, because we are concerned with $2n$ halo nuclei, where the n particle is truly a neutron, these two quadrants are not of much interest in the present study. The upper-left quadrant corresponds to the unbound *n*-*n* subsystem with a bound *n*-*c* subsystem, for which we use the name *Samba* as recommended in [Yam06]. The final quadrant corresponds to the three-body systems for which none of the two-body subsystems is bound. This system is referred to as a *Borromean* system.

We can now use our plot to analyze the likelihood of the Efimov effect for the different types of three-body systems, with a focus on $2n$ halo nuclei. As one would expect, the *Borromean* systems offer the smallest chance of having an excited Efimov state, as the two-body energy would have to be very small, or accordingly the scattering length very large, to produce even one excited state. However, this can be achieved in ultracold atoms, as the presence of so called *Feshbach resonances* allows one to tune the two-body scattering length to a very large value [Ti93]. Interestingly, the *Samba* systems have the largest region supporting the occurrence of excited Efimov states. As long as the *n*-*c* scattering length is large enough, there can be a large variation in the *n*-*n* scattering length that would still allow for the Efimov effect. This agrees with the findings of Efimov [Ef70], that as long as 2 of the 3 two-body interactions have a large scattering length, the sequence of three-body binding energies can occur.

Looking at possible halo nuclei candidates, we have plotted the positions of ^{20}C, ^{18}C, ^{11}Li, ^{12}Be, and ^{14}Be in Fig. 4.4 using the experimental values of the "Nuclear Data Evaluation Project" of TUNL [TUNL] for the *n*-*c* and three-body ground state energy data, and the standard value of the *n*-*n* scattering length, $a_{nn} = (-18.7 \pm 0.6)$ fm [Gon99] to calculate the *n*-*n* two-body energy according to Eq. (4.1). The only halo candidate that has any possibility of an excited Efimov state is ^{20}C, due to the large uncertainty in the *n*-^{18}C bound state energy. We will return to this nucleus shortly. The positions and relatively small experimental errors in the other halo nuclei data rule out the chance of finding excited Efimov states in these nuclei. Other halo nuclei candidates which exist have values of the two-body energies which are too large to even appear on our plot.

4.3.3 Efimov Excited State for ^{20}C

The central value for the *n*-^{18}C bound state energy, $E_{nc} = (162 \pm 112)$ keV [Aud95], lies almost exactly on the boundary region for $A = 18$ in Fig. 4.5. The large error in this value, however, dips well into the region where at least one excited Efimov state can occur. The error in the three-body ground state energy of ^{20}C is small compared to E_{nc}. Thus, we can calculate the value of the excited state energies as a function of E_{nc}, using the standard value for a_{nn}, and fixing our cutoff to reproduce the experimental value of the ground state energy $B_3^{(0)} = 3506.0$ keV [TUNL, Aud95]. The result is plotted in Fig. 4.6, where the solid line is the excited state energy, and the dashed line represents the scattering threshold. The inset graph shows the excited state energy relative to the scattering threshold. We find only one excited

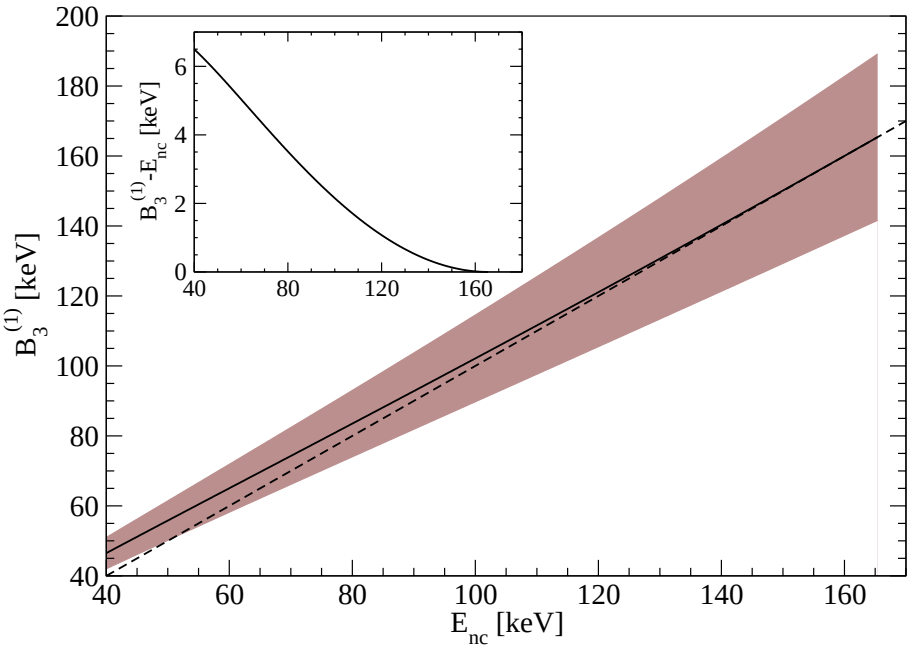

Figure 4.6: Binding energy of the ^{20}C excited Efimov state as a function of the n-^{18}C bound state energy (solid line) with leading order error bands. The dashed line represents the scattering threshold which is given by $B_3^{(1)} = E_{nc}$. The inset shows the excited state energy relative to the scattering threshold.

Efimov state, existing when $E_{nc} < 165$ keV. For larger values of E_{nc}, the ^{20}C system moves outside of the boundary curve, and the excited Efimov state is destroyed. This rules out the possibility of finding an excited Efimov state using a competing value for the n-^{18}C bound state energy: $E_{nc} = (530 \pm 130)$ keV [Na99].

The binding energy relative to the scattering threshold is always below 7 keV, a value very small in comparison with the ground state energy. Also, the error bands are large compared to the relative energy of the excited state to the scattering threshold, with the lower error band almost always below the scattering threshold.

We have again estimated this error using the theoretical uncertainty of our effective potential. In this first order calculation, the uncertainty in binding energies calculated using the two-body effective potential of Eq. (4.2) is $\approx r_0/a$. Our effective potential, made up of contact interactions, will break down for momenta of the order of the pion mass scale. We therefore use the inverse of the pion mass $m_\pi = 140$ MeV to estimate the effective range $r_0 \approx 1/m_\pi$. The uncertainty in the binding energy of the excited state is then the quadratic sum of the uncertainties from the n-n and n-^{18}C interactions: $\sqrt{2\mu_{nn}E_{nn}/m_\pi^2 + 2\mu_{nc}E_{nc}/m_\pi^2}$. These uncertainties are of the same order of magnitude as those found assuming that the effective range is related to the inverse of the cutoff, $r_0 \approx 1/\Lambda$.

This result is in overall qualitative agreement with the previous studies of Amorim

et al. [Amo96] and Mazumdar et al. [Maz00], who also found the presence of a very weakly bound excited Efimov state in ^{20}C for sufficiently small values of E_{nc}. However, both of these studies have a larger value for the excited state energy, with the Mazumdar group also finding a second excited state for $E_{nc} < 100$ keV. Also, the disagreement with the results of the Amorim paper mentioned before casts doubts on the quantitative results of [Amo96], as a more recent study from the same group [Yam08a] suggests better agreement with the results presented here. This newer analysis is one of a few recent studies extending the trajectory of this excited state into the scattering region to explore the possibility of finding a resonance in the n-^{19}C scattering sector [Yam08a, Yam08b, Aro04, Maz06].

4.4 Form Factors and Mean Square Radii

We are now interested in calculating other low-energy physical properties of three-body halo nuclei, specifically the matter density form factors and the mean square radii. The information needed to calculate such quantities is held in the wave functions of the known bound states. In the next subsection, the full three-body wave function will be reconstructed from the Faddeev spectator functions F_n and F_c. Once the three-body wave function is known, the corresponding one- and two-body matter density form factors will be computed (Sec. 4.4.2). In Sec. 4.4.3, the mean square distances between two of the three particles as well as the mean square distance of one of the particles from the center of mass will be extracted from the proper form factor.

4.4.1 Reconstruction of the Wave Function

The full wave function of the bound $2n$ halo nucleus can be reconstructed from the solutions for the spectator functions F_n and F_c found from our coupled integral equations, Eqs. (4.45, 4.46). However, the form of the wave function depends on the choice of two-body subsystem and corresponding spectator particle. In this subsection, we derive the expressions for the S-wave part of the full wave functions: ${}_i\langle pq|\Psi\rangle \equiv \Psi_i(p,q)$, where the index $i = n, c$ labels the chosen spectator particle. In the wave functions, the p Jacobi momentum describes the relative momentum between the two particles in the chosen two-body subsystem, while q describes the momentum of the spectator particle relative to the center of mass of the two-body subsystem.

For the neutron as spectator particle, using the relation for the wave function in terms of its Faddeev components, Eq. (3.13), we find:

$$\begin{aligned}
\Psi_n(p,q) &= {}_n\langle pq \mid 1 - P \mid \psi\rangle_n + {}_n\langle pq \mid \psi\rangle_c \\
&= \psi_n(p,q) - \int dp' p'^2 dq' q'^2 \; {}_{n_2}\langle pq \mid p'q'\rangle_{n_1} \; \psi_n(p',q') \\
&\quad + \int dp' p'^2 dq' q'^2 \; {}_n\langle pq \mid p'q'\rangle_c \; \psi_c(p',q'). \qquad (4.49)
\end{aligned}$$

The results of the overlap-matrix elements are similar to those found in App. B, however, we now wish to find a form with which the dp' and dq' integrals can be performed with delta functions. The general result for this case can be found in [No01]. The results for S-waves are simple:

$$ {}_{n_2}\langle pq \mid p'q' \rangle_{n_1} = -\frac{1}{2}\int_{-1}^{1} dx \; \frac{\delta(p' - \tilde{\pi}_{nn})}{p'\tilde{\pi}_{nn}} \frac{\delta(q' - \tilde{\pi}'_{nn})}{q'\tilde{\pi}'_{nn}}, \tag{4.50} $$

where

$$ \tilde{\pi}_{nn} \equiv \tilde{\pi}_{nn}(p,q) = \sqrt{\frac{1}{(A+1)^2}\,p^2 + \frac{A^2(A+2)^2}{(A+1)^4}\,q^2 + \frac{A(A+2)}{(A+1)^3}\,2pqx}, \tag{4.51} $$

$$ \tilde{\pi}'_{nn} \equiv \tilde{\pi}'_{nn}(p,q) = \sqrt{p^2 + \frac{1}{(A+1)^2}\,q^2 - \frac{1}{A+1}\,2pqx}; \tag{4.52} $$

and

$$ {}_{n}\langle pq \mid p'q' \rangle_{c} = \frac{1}{2}\int_{-1}^{1} dx \; \frac{\delta(p' - \tilde{\pi}_{nc})}{p'\tilde{\pi}_{nc}} \frac{\delta(q' - \tilde{\pi}'_{nc})}{q'\tilde{\pi}'_{nc}}, \tag{4.53} $$

where

$$ \tilde{\pi}_{nc} \equiv \tilde{\pi}_{nc}(p,q) = \sqrt{\frac{1}{4}\,p^2 + \frac{(A+2)^2}{4(A+1)^2}\,q^2 + \frac{A+2}{2(A+1)}pqx}, \tag{4.54} $$

$$ \tilde{\pi}'_{nc} \equiv \tilde{\pi}'_{nc}(p,q) = \sqrt{p^2 + \frac{A^2}{(A+1)^2}\,q^2 - \frac{A}{A+1}2pqx}. \tag{4.55} $$

We substitute these relations back in, and use the expression defining the Faddeev component in terms of the spectator function, Eq. (4.44). After performing the integrations with the delta functions we find:

$$ \begin{aligned} \Psi_n(p,q) &= \psi_n(p,q) + \frac{1}{2}\int_{-1}^{1} dx \; \left[\psi_n(\tilde{\pi}_{nn}, \tilde{\pi}'_{nn}) + \psi_c(\tilde{\pi}_{nc}, \tilde{\pi}'_{nc})\right] \\ &= G_0^n(p,q;B_3)g(p)t_n(q;B_3)F_n(q) \\ &\quad + \frac{1}{2}\int_{-1}^{1} dx \; G_0^n(\tilde{\pi}_{nn}, \tilde{\pi}'_{nn};B_3)g(\tilde{\pi}_{nn})t_n(\tilde{\pi}'_{nn};B_3)F_n(\tilde{\pi}'_{nn}) \\ &\quad + \frac{1}{2}\int_{-1}^{1} dx \; G_0^c(\tilde{\pi}_{nc}, \tilde{\pi}'_{nc};B_3)g(\tilde{\pi}_{nc})t_c(\tilde{\pi}'_{nc};B_3)F_c(\tilde{\pi}'_{nc}), \end{aligned} \tag{4.56} $$

where the regulator function g and the T-matrices t_n and t_c are given in Eqs. (4.3, 4.28, 4.29). The expressions for the propagators G_0^n and G_0^c can be found in Eqs. (4.17, 4.18). One can show through substitution that $G_0^n(\tilde{\pi}_{nn}, \tilde{\pi}'_{nn}; B_3) = G_0^n(p, q; B_3)$, and $G_0^c(\tilde{\pi}_{nc}, \tilde{\pi}'_{nc}; B_3) = G_0^n(p, q; B_3)$, and the propagators simplify.

If the core is the spectator particle, we follow the same procedure, but start by projecting onto the other Jacobi basis state:

$$\begin{aligned}\Psi_c(p,q) &= {}_c\langle pq \mid 1 - P \mid \psi\rangle_n + {}_c\langle pq \mid \psi\rangle_c \\ &= 2\int dp' p'^2 dq' q'^2 \; {}_c\langle pq \mid p'q'\rangle_n \; \psi_n(p',q') \; + \psi_c(p,q). \end{aligned} \tag{4.57}$$

Again, we need to calculate the overlap-matrix element such that it eliminates the integrations over dp' and dq'. The result for S-waves is:

$${}_c\langle pq \mid p'q'\rangle_n = \frac{1}{2}\int_{-1}^{1} dx \; \frac{\delta(p' - \tilde{\pi}_{cn})}{p'\tilde{\pi}_{cn}} \frac{\delta(q' - \tilde{\pi}'_{cn})}{q'\tilde{\pi}'_{cn}} \tag{4.58}$$

where

$$\tilde{\pi}_{cn} \equiv \tilde{\pi}_{cn}(p,q) = \sqrt{\frac{A^2}{(A+1)^2}\,p^2 + \frac{(A+2)^2}{4(A+1)^2}\,q^2 + \frac{A(A+2)}{2(A+1)^2}\,2pqx}, \tag{4.59}$$

$$\tilde{\pi}'_{cn} \equiv \tilde{\pi}'_{cn}(p,q) = \sqrt{p^2 + \frac{1}{4}q^2 - pqx}. \tag{4.60}$$

After the proper substitutions and integrations we find:

$$\begin{aligned}\Psi_c(p,q) &= \int_{-1}^{1} dx \; G_0^n(\tilde{\pi}_{cn}, \tilde{\pi}'_{cn}; B_3) g(\tilde{\pi}_{cn}) t_n(\tilde{\pi}'_{cn}; B_3) F_n(\tilde{\pi}'_{cn}) \\ &\quad + G_0^c(p,q; B_3) g(p) t_c(q; B_3) F_c(q). \end{aligned} \tag{4.61}$$

Again, one can show through substitution that $G_0^n(\tilde{\pi}_{cn}, \tilde{\pi}'_{cn}; B_3) = G_0^c(p, q; B_3)$.

The full wave functions are now given in terms of the spectator functions, however, in each expression there exists a spectator function which must be calculated at a shifted momentum. Numerically, the value of the function at the shifted momentum must be found through an interpolation. We use a cubic hermitian Spline interpolation of the form:

$$F_i(\tilde{\pi}') \approx \sum_j S_j(\tilde{\pi}') F_i(q_j), \tag{4.62}$$

where S_j are the Spline elements.

4.4.2 One- and Two-Body Matter Density Form Factors

The three-body wave functions found in the previous subsection can be used to calculate other low-energy properties of the three-body bound state. With the Jacobi momentum states it is straightforward to calculate the Fourier transform of the one- and two-body matter densities with respect to the momentum transfer squared. These are defined as the one- and two-body matter density form factors $\mathcal{F}_i(k^2)$ and $\mathcal{F}_{ni}(k^2)$, respectively, where $i = n, c$. In the wave functions, the $\vec{p}$ Jacobi momentum describes the relative momentum between the two particles in the chosen two-body subsystem, while $\vec{q}$ describes the momentum of the spectator particle relative to the center of mass of the two-body subsystem.[4] Therefore, the one-body form factors can be obtained as follows:

$$\mathcal{F}_i(k^2) = \int d^3p\ d^3q\ \Psi_i(\vec{p},\vec{q})\Psi_i(\vec{p},\vec{q}-\vec{k}), \tag{4.63}$$

where $i = n, c$ depending on the desired two-body subsystem. The two-body form factors can be solved similarly:

$$\mathcal{F}_{nc}(k^2) = \int d^3p\ d^3q\ \Psi_n(\vec{p},\vec{q})\Psi_n(\vec{p}-\vec{k},\vec{q}), \tag{4.64}$$

and

$$\mathcal{F}_{nn}(k^2) = \int d^3p\ d^3q\ \Psi_c(\vec{p},\vec{q})\Psi_c(\vec{p}-\vec{k},\vec{q}). \tag{4.65}$$

These relations can be simplified further by using the fact that at leading order only S-waves contribute. Consequently, we project the three-body wave functions onto the S-wave, and then perform the angular integrations. In our normalization, the wave functions obey the relation:

$$\Psi_i(p,q) = 4\pi < \Psi_i(\vec{p},\vec{q}) >, \tag{4.66}$$

where $< ... >$ denotes the angular average. This relation is then substituted into the above form factor relations, and the trivial angular integrations can be performed. Furthermore, the form factors will be normalized in the end such that $\mathcal{F}(k^2 = 0) = 1$, so any constant overall factor can be dropped. For the one-body form factors we have:

$$\mathcal{F}_i(k^2) \ = \ \int dp\ p^2 \int dq\ q^2 \int_{-1}^{1} dx\ \Psi_i(p,q)\Psi_i(p,\sqrt{q^2+k^2-2qkx}), \tag{4.67}$$

and for the two-body form factors we have:

$$\mathcal{F}_{nc}(k^2) \ = \ \int dp\ p^2 \int dq\ q^2 \int_{-1}^{1} dx\ \Psi_n(p,q)\Psi_n(\sqrt{p^2+k^2-2pkx},q), \tag{4.68}$$

[4] Recall that we use the spectator notation for the wave functions, where the index i on Ψ_i refers to the spectator particle.

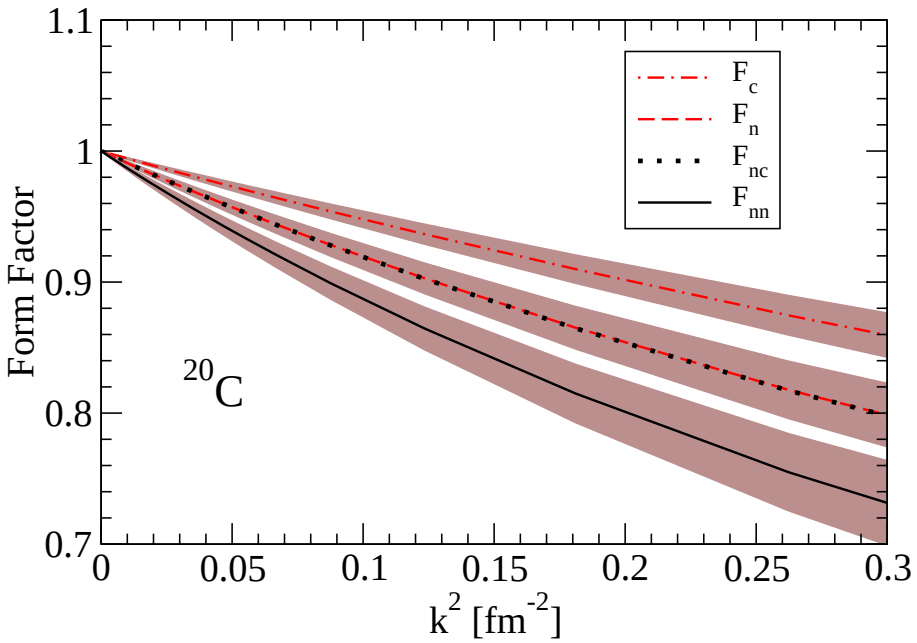

Figure 4.7: The various one- and two-body matter density form factors with leading order error bands for the ground state of ^{20}C in the low-energy region: $\mathcal{F}_{nn}(k^2)$ black solid line; $\mathcal{F}_{nc}(k^2)$ black dotted line; $\mathcal{F}_{n}(k^2)$ lighter (red) dashed line; $\mathcal{F}_{c}(k^2)$ lighter (red) dot-dashed line.

and

$$\mathcal{F}_{nn}(k^2) \;=\; \int dp\; p^2 \int dq\; q^2 \int_{-1}^{1} dx\; \Psi_c(p,q)\Psi_c(\sqrt{p^2+k^2-2pkx},q). \quad (4.69)$$

The expressions relating $\Psi_n(p,q)$ and $\Psi_c(p,q)$ to the solutions $F_n(q)$ and $F_c(q)$ of Eqs. (4.45, 4.46) are given in Sec. 4.4.1. We are now in the position to calculate these form factors for halo nuclei.

As a general example, we have plotted the form factors for the ground state of ^{20}C, in the low-energy region in Fig. 4.7, using a bound state energy of 3506.0 keV, a n-n two-body virtual energy of 116.04 keV, and a n-c bound state energy of 161.0 keV. The theory breaks down for momentum transfers of the order of the pion-mass squared ($k^2 \approx 0.5$ fm^{-2}) where the one-pion exchange interaction cannot be approximated by short-range contact interactions anymore. Here one can see that for low momentum transfer the one-body neutron $\mathcal{F}_n(k^2)$ and the two-body core-neutron $\mathcal{F}_{nc}(k^2)$ form factors lie nearly on top of each other. This is due to the fact that the core consists of 18 nucleons and, therefore, the center of mass is very near the core. This fact is also seen in the shallow slope of the one-body core form factor $\mathcal{F}_c(k^2)$.

The theoretical error bands for the form factors are an estimate arising from the theoretical uncertainty of our two-body effective potential, Eq. (4.2). In this first order calculation, the uncertainty in the effective potential comes from the next term

in the expansion, which is related to the effective range. Therefore, the theoretical uncertainty is $\approx r_0/a$. As discussed in Sec. 4.3.3, we use the inverse of the pion mass $m_\pi = 140$ MeV to approximate the effective range, $r_0 \approx 1/m_\pi$. With the form factors normalized to $\mathcal{F}(k^2 = 0) = 1$, and because $|E_{nc}| > |E_{nn}|$, the theory error is estimated to be $\approx (1 - \mathcal{F})\sqrt{2\mu_{nc}E_{nc}}/m_\pi$.

4.4.3 Mean Square Radii and Geometry of $2n$ Halo Nuclei

The mean square radii for our three-body bound states are calculated from the matter density form factors in the low momentum transfer region. The matter density form factor is defined as the Fourier transform of the matter density:

$$\mathcal{F}(k^2) = \int \rho(\vec{x}) e^{i\vec{k}\cdot\vec{x}} d^3x, \tag{4.70}$$

with the normalization $\mathcal{F}(k^2 = 0) = 1$. In the low momentum transfer region, the exponential can be expanded, and assuming a spherically symmetric matter density, we see that the slope of the form factor determines the mean square radius $\langle r^2 \rangle$:

$$\begin{aligned} \mathcal{F}(k^2) &= \int \rho(\vec{x}) \left(1 + i\vec{k}\cdot\vec{x} - \frac{(\vec{k}\cdot\vec{x})^2}{2} + \ldots \right) d^3x \\ &= 1 - \frac{1}{6}k^2 \left\langle r^2 \right\rangle + \ldots . \end{aligned} \tag{4.71}$$

Of course, the mean square radius acquired depends on the choice of one- or two-body form factor. Since $\vec{p}$ describes the relative momentum of the two particles in the two-body subsystem chosen, the slope of $\mathcal{F}_{ni}(k^2)$ will give the mean square distance between the two particles in the chosen two-body subsystem, either $\langle r^2_{nn} \rangle$ or $\langle r^2_{nc} \rangle$. Analogously, because $\vec{q}$ describes the momentum of the spectator particle relative to the center of mass of the two-body subsystem, the slope of $\mathcal{F}_i(k^2)$ will give the mean square distance of the spectator particle from the center of mass of the two-body subsystem, either $\left\langle r^2_{c-nn} \right\rangle$ or $\left\langle r^2_{n-nc} \right\rangle$. However, it is more useful to calculate the distance of the individual particles from the center of mass of the three-body bound state. If b_i is the slope of the one-body form factor $\mathcal{F}_i(k^2)$ at the limit $k^2 = 0$, the mean square radius of one of the bodies i ($i = n, c$) from the three-body center of mass is given by:

$$\left\langle r_i^2 \right\rangle = -6b_i \left(1 - \frac{m_i}{2m_n + m_c} \right)^2, \tag{4.72}$$

where m_i is the mass of the desired particle i, and m_n and m_c are the neutron and core masses, respectively. The various radii of the three-body system are illustrated in Fig. 4.8(a).

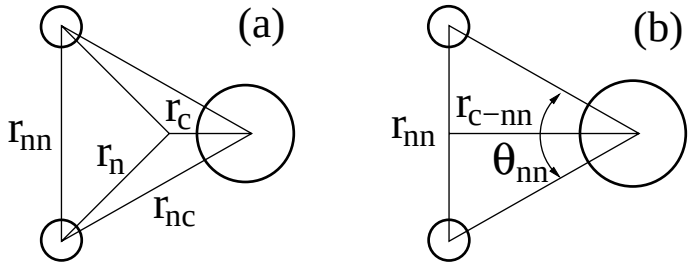

Figure 4.8: (a) The various radii of the three-body system. (b) Further geometry of the $2n$ halo nucleus, specifically looking at the two neutron opening angle θ_{nn}.

We have extracted the radii by fitting a polynomial in k^2 to the form factor results for small k^2. We have used polynomials of varying degree up to 5th order in k^2 in order to verify the stability and convergence of the fit. We have found a satisfactory stability in the slope when fitting to a polynomial to the fourth order in k^2, up to a value of k^2 at which the form factor has dropped less than 10 percent.

As with the binding energies in the sequence of three-body Efimov states, as discussed in Sec. 4.3.1, the mean square radii of these states also display universal properties that are insensitive to the details of the two-body potential at short distances. One such property is that for the resonant limit, $a \to \pm\infty$, at which there are infinitely many arbitrarily-shallow three-body bound states, the ratio of the radii of neighboring states approaches a universal factor as the threshold is approached. This universal scaling factor is exactly the inverse of the universal scaling factor found for the ratio of binding energies (see Eq. (4.48)):

$$\left\langle r^2 \right\rangle^{(n)} / \left\langle r^2 \right\rangle^{(n+1)} \longrightarrow (\lambda_0)^{-2}, \tag{4.73}$$

as $n \to +\infty$ with $a = \pm\infty$. Therefore, we can construct a dimensionless quantity from the root of the product of the mean square radius and the three-body binding energy $\sqrt{\langle r^2 \rangle B_3}$. The ratio of this quantity for neighboring states approaches unity in the resonant limit as the threshold is approached.

The extracted radii for known halo nuclei are shown in Table 4.1. As input we have used the standard value of the n-n scattering length, $a_{nn} = (-18.7 \pm 0.6)$ fm [Gon99], to calculate the n-n two-body virtual energy, $E_{nn} = 116.04$ keV, along with the experimental values of the n-c two-body energies E_{nc} shown in the third column of Table 4.1 (negative values correspond to virtual energies). As a three-body input, the cutoff is tuned to reproduce the experimental ground state binding energy $B_3^{(0)}$ shown in the second column of Table 4.1. These experimental values for the two-body and three-body energies are taken from the most recent results of the "Nuclear Data Evaluation Project" of TUNL [TUNL], except where otherwise noted. In the last column, we have given the experimental values for the n-n mean square radius, as given by Marqués et al. [Mar00]. These experimental values for $\sqrt{\langle r_{nn}^2 \rangle}$ were found using the technique of intensity interferometry along with the two neutron correlation

Nucleus	B_3 [keV]	E_{nc} [keV]	$\sqrt{\langle r_{nn}^2 \rangle}$ [fm]	$\sqrt{\langle r_{nc}^2 \rangle}$ [fm]	$\sqrt{\langle r_n^2 \rangle}$ [fm]	$\sqrt{\langle r_c^2 \rangle}$ [fm]	$\sqrt{\langle r_{nn}^2 \rangle_{exp}}$ [fm]
^{11}Li	247	-25	8.7±0.7	7.1±0.5	6.5±0.5	1.0±0.1	
	247	-800 [Wil75]	6.8±1.8	5.9±1.5	5.3±1.4	0.9±0.2	6.6±1.5
	320	-800 [Wil75]	6.2±1.6	5.3±1.4	4.8±1.3	0.8±0.2	
	170	-800 [Wil75]	7.9±2.1	6.7±1.8	6.0±1.6	1.0±0.3	
^{14}Be	1120	-200 [Thoe00]	4.1±0.5	3.5±0.5	3.2±0.4	0.40±0.05	5.4±1.0
^{12}Be	3673	503	3.0±0.6	2.5±0.5	2.3±0.5	0.32±0.07	
^{18}C	4940	731	2.6±0.7	2.2±0.6	2.1±0.5	0.18±0.05	
^{20}C	3506	161	2.8±0.3	2.4±0.3	2.3±0.3	0.19±0.02	
	3506	60	2.8±0.2	2.3±0.2	2.2±0.2	0.18±0.01	
	3506	0.0	2.7±0.2	2.2±0.2	2.1±0.2	0.18±0.01	
^{20}C*	65.0±6.8	60	42±3	38±3	41±3	2.2±0.2	
^{20}C*	1.02±0.08	0.0	130±10	97±7	93±7	6.9±0.5	

Table 4.1: Various mean square radii of different halo nuclei. The second two columns show the input values for the three-body ground state energy and the two-body n-c energy (negative values corresponding to virtual energies), respectively, as given by [TUNL], except where otherwise noted. The experimental values for the n-n root mean square radii, shown in the last column, are taken from [Mar00]. The rows marked by ^{20}C* show the results for the excited Efimov state of ^{20}C, with binding energy displayed in the second column, which is found above the ground state ($B_3 = 3506$ keV).

function to study the dissociation at intermediate energies of two neutrons in halo nuclei. However, the large uncertainty in these values is indicative of the need for more precise measurements of the mean square distances in $2n$ halo nuclei. Also, the recent work by Orr [Or08] discusses the care which must be taken in interpreting the results of [Mar00]. Specifically, he mentions that the technique is sensitive to the population of states in the continuum by the dissociation process rather than being a true ground state measurement. For more details on this issue, see Ref. [Or08].

Our results agree overall with the study done by Yamashita et al. using a similar three-body model [Yam04]. Our study expands on this previous work by showing the leading order theoretical uncertainty as well as the results for an excited Efimov state in the case of ^{20}C.

The leading order theoretical error is again estimated by the uncertainty of the two-body effective potential, Eq. (4.2), which is $\approx r_0/a$, where r_0 is the effective range of the interaction, and a the scattering length. Using the inverse of the pion mass to estimate the effective range, $r_0 \approx 1/m_\pi$, the uncertainty in the radii is then calculated from the greater of the error arising from the n-n or n-c interaction: $\sqrt{2\mu_{nc}E_{nc}}/m_\pi$ or $\sqrt{2\mu_{nn}E_{nn}}/m_\pi$.

We will now discuss the results for the various known three-body halo nuclei as shown in Table 4.1:

For ^{11}Li, there is a relatively large uncertainty in the experimental values of both the ground state energy, $B_3^{(0)} = (247 \pm 80)$ keV [TUNL], and the n-c virtual energy,

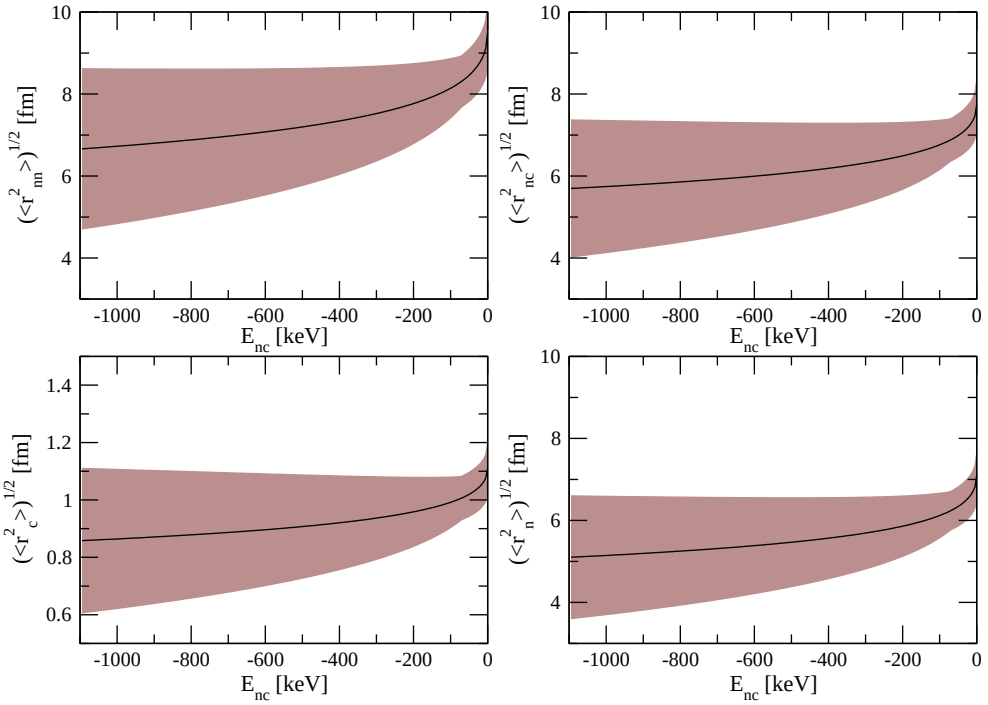

Figure 4.9: The various mean square radii for ^{11}Li as a function of the n-^{9}Li two-body energy (negative values correspond to the virtual state) with error bands from the theoretical uncertainty. As input, the n-n two-body energy $E_{nn} = -116.04$ keV, and the three-body binding energy $B_3^{(0)} = 247$ keV were used.

with two competing values: $E_{nc} = (-25 \pm 15)$ keV [TUNL], and $E_{nc} = (-800 \pm 250)$ keV [Wil75]. For this reason it is advantageous to plot the various mean square radii over the full range of potential E_{nc} values. The results, using the central value for the three-body binding energy as input, $B_3^{(0)} = 247$ keV, can be seen in Fig. 4.9, with error bands estimated from the theoretical uncertainty, as described above. These plots are a good general example of the relation between the mean square radii and the virtual two-body n-c energy for *Borromean* halo nuclei, where none of the two-body subsystems are bound. As the n-c virtual energy decreases in magnitude the three-body bound state increases slowly in size, with a more rapid increase in size as the energy approaches zero and crosses over into the *Samba* configuration, where the n-c subsystem becomes bound.

In Table 4.1, we have highlighted, using the central value of the three-body binding energy, the central values of the competing n-c energies. While the two-body virtual energy reported in [Wil75], $E_{nc} = -800$ keV leads to $\sqrt{\langle r^2_{nn}\rangle} = (6.8 \pm 1.8)$ fm, in close agreement with the experimental result $\sqrt{\langle r^2_{nn}\rangle}_{exp} = (6.6 \pm 1.5)$ fm, a definite conclusion can not be reached due to the large error bars of the radii. We have also listed the upper and lower limits of the three-body binding energy, $B_3^{(0)} = 170$ and 320 keV, along with our preferred value of $E_{nc} = -800$ keV, which shows a more general

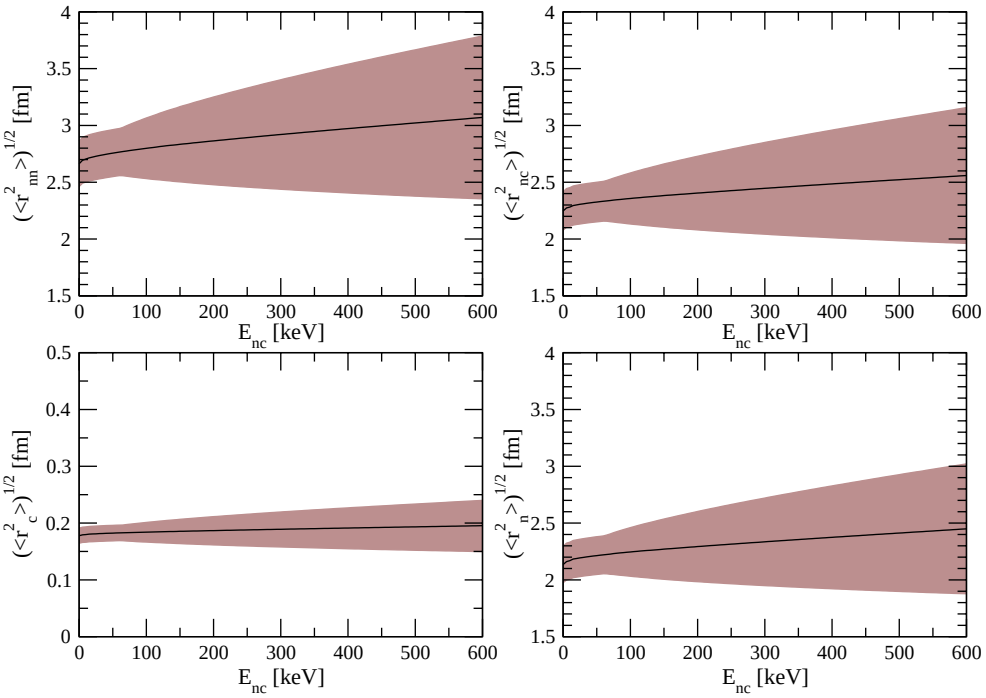

Figure 4.10: The various mean square radii for ^{20}C as a function of the n-^{18}C two-body energy with error bands from the theoretical uncertainty. As input, the n-n two-body energy $E_{nn} = -116.04$ keV, and the three-body binding energy $B_3^{(0)} = 3506$ keV were used.

result: for halo nuclei, the larger the three-body binding energy, the smaller the mean square radii. In terms of the plots in Fig. 4.9, using a larger(smaller) value for $B_3^{(0)}$ as input would shift the curve down(up) in each plot. Due to the large uncertainties in both the theoretical and experimental values for ^{11}Li, there exists a large range of E_{nc} values which would produce a $\sqrt{\langle r_{nn}^2 \rangle}$ value in agreement with the experimental value of Marqués et al. [Mar00].

As another example of a *Borromean* halo nucleus, we see that the calculated result for the n-n mean square radius of ^{14}Be, $\sqrt{\langle r_{nn}^2 \rangle} = (4.1 \pm 0.5)$ fm, is smaller than the experimental value $\sqrt{\langle r_{nn}^2 \rangle}_{exp} = (5.4 \pm 1.0)$ fm [Mar00], but still within one error bar. Here we have used the central value of the two-body n-c virtual energy as reported by [Thoe00], $E_{nc} = -200$ keV. In using the resonant limit, $E_{nc} = 0.0$ keV, we see that the largest theoretical value for $\sqrt{\langle r_{nn}^2 \rangle} = (4.6 \pm 0.3)$ fm, which allows an unbound n-c two-body subsystem, is still smaller than the experimental value. Another reported value for the two-body virtual energy, $E_{nc} = (-1900 \pm 500)$ keV [TUNL], would produce even smaller mean square radii, even farther away from the experimental value.

We now turn our attention to the so called *Samba* halo nuclei in which the n-c subsystem is bound. As examples, we have listed the results for ^{12}Be and ^{18}C, using

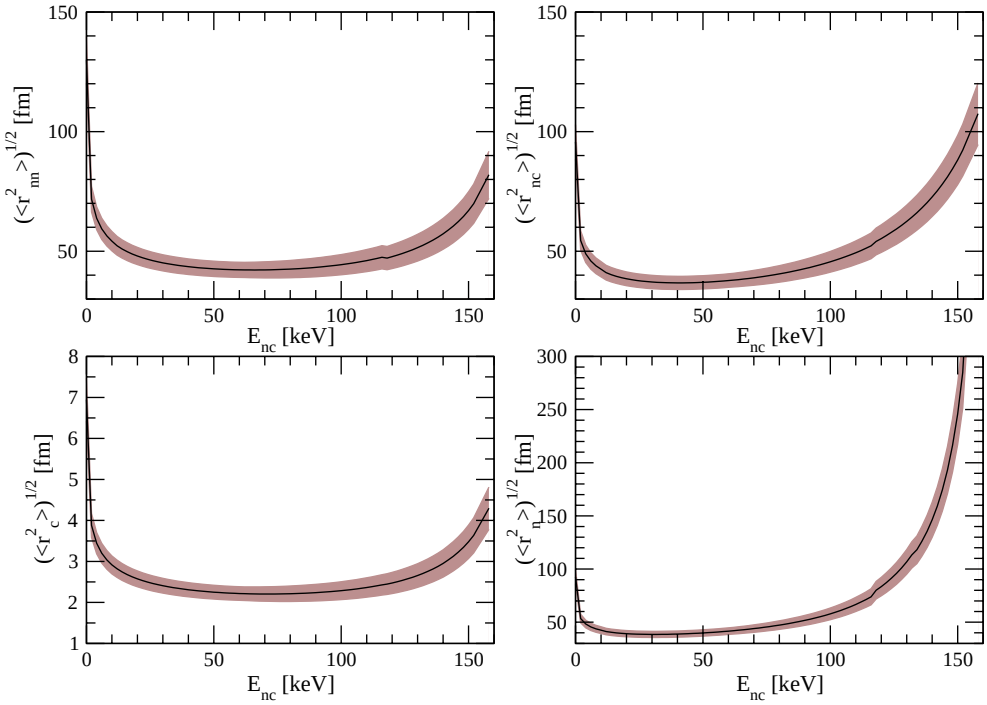

Figure 4.11: The various mean square radii for the Efimov excited state of ^{20}C as a function of the n-^{18}C two-body energy with error bands from the theoretical uncertainty. As input, the n-n two-body energy $E_{nn} = -116.04$ keV, and the three-body binding energy $B_3^{(0)} = 3506$ keV were used.

the central values of the experimental energies [TUNL] in Table 4.1.

Of greater interest are the results from the case of ^{20}C, as the large uncertainty in the n-c energy, with two competing values, $E_{nc} = (162 \pm 112)$ keV [TUNL], and $E_{nc} = (530 \pm 130)$ keV [Na99], suggests that we look at the mean square radii over a range of E_{nc} values. The results, using the central value for the three-body binding energy as input, $B_3^{(0)} = 3506$ keV, can be seen in Fig. 4.10, with error bands estimated from the theoretical uncertainty, as described above. These plots are a good general example of the relation between the mean square radii and the two-body n-c binding energy for *Samba* halo nuclei. As the n-c binding energy decreases in magnitude the three-body bound state decreases slowly in size, with a slightly more rapid decrease in size as the energy approaches zero and crosses over into the *Borromean* configuration, where the n-c subsystem becomes unbound. This suggests that as the two-body n-c state is more weakly bound, the particles must be closer together in order for the three-body state to be bound with the same energy.

As was shown in Sec. 4.3.3, there possibly exists one Efimov excited state in ^{20}C for $E_{nc} < 165$ keV. The mean square radii for this excited state were calculated over a range of E_{nc} values and plotted, with leading order error bands, in Fig. 4.11. Here we see the interesting phenomenon that although the radii remain relatively constant in

the middle of the range of n-c energies which allow the excited state, as the endpoints are approached, the radii begin to increase rapidly, and then to diverge, both when $E_{nc} \to 165$ and $\to 0.0$ keV. It is at these points that the ^{20}C system moves outside the boundary curve depicted in Fig. 4.5, the Efimov excited state is destroyed, and the three particles consequently fly apart.

In Table 4.1, we have highlighted the result using the central value of the accepted n-c two-body binding energy, as well as two values which lead to an Efimov excited state, including the resonant limit $E_{nc} = 0.0$ keV. The rows marked by ^{20}C* represent the results of the Efimov excited state. The three-body binding energy of this excited state is listed in the second column with leading order theoretical uncertainty calculated as described in Sec. 4.3.3.

Next we looked at a further geometrical property of $2n$ halo nuclei, specifically the two neutron opening angle. As defined in Fig. 4.8(b), it is straightforward to calculate θ_{nn} using the pair of mean square radii found from the three-body wave function Ψ_c, $\sqrt{\langle r_{nn}^2 \rangle}$ and $\sqrt{\langle r_{c-nn}^2 \rangle}$:

$$\tan\left(\frac{\theta_{nn}}{2}\right) = \frac{\frac{1}{2}\sqrt{\langle r_{nn}^2 \rangle}}{\sqrt{\langle r_{c-nn}^2 \rangle}}. \tag{4.74}$$

Our results for known halo nuclei are shown in Table 4.2 using the central values of the experimental two-body and three-body energies as inputs (compare with Table 4.1). We show the results for the competing values of the n-c virtual energy for the case of ^{11}Li. For the case of ^{20}C we also show the result with $E_{nc} = 0.0$ keV, along with its corresponding Efimov excited state. The opening angle has been calculated from experimental data in two recent works by Bertulani et al. [Ber07], and Hagino et al. [Hag07], and their results are shown in the last two columns, respectively. The study by Bertulani et al. uses the experimental values of $\sqrt{\langle r_{nn}^2 \rangle}$ found by Marqués et al. [Mar00] seen in the last column of Table 4.1, along with two different determinations of $\sqrt{\langle r_{c-nn}^2 \rangle}$ (see [Ber07] and references within): using laser spectroscopy data (results displayed in first row for ^{11}Li and ^{14}Be), and also using the $B(E1)$ strength (second row for ^{11}Li). However, the result for ^{14}Be also uses a theoretical calculation for one of the inputs, rather than being a pure experimental result. On the other hand, the study by Hagino et al. uses the experimental values of $B(E1)$ to calculate $\sqrt{\langle r_{c-nn}^2 \rangle}$, along with two different determinations of $\sqrt{\langle r_{nn}^2 \rangle}$ (see [Hag07] and references within): using experimental values of the nuclear matter radii (first row for ^{11}Li), and using the results of Marqués et al. [Mar00] (second row for ^{11}Li). Also, results found using a three-body model with density dependent two-body contact interactions were found in [Hag07], and are displayed in the third row for ^{11}Li. As would be expected, our results agree very well with the results from the three-body theoretical model used in [Hag07]. Our result for ^{11}Li using our preferred choice of $E_{nc} = -800$ keV, also agrees very well with the experimental results obtained using the value for $\sqrt{\langle r_{nn}^2 \rangle}_{exp}$ from Marqués et al., which would be expected as our $\sqrt{\langle r_{nn}^2 \rangle}$ value also agrees with this experimental value. Overall there is a good agreement between our calculated results and the results of [Ber07] and [Hag07], as all θ_{nn} values

Nucleus	$\sqrt{\langle r_{nn}^2 \rangle}$ [fm]	$\sqrt{\langle r_{c-nn}^2 \rangle}$ [fm]	θ_{nn}	θ_{nn} [Ber07]	θ_{nn} [Hag07]
^{11}Li	8.7±0.7	5.5±0.4	$77^{\circ+8}_{-9}$	$58^{\circ+10}_{-14}$	$56.2^{\circ+17.8}_{-21.3}$
	6.8±1.8	5.0±1.3	$68^{\circ+31}_{-25}$	$66^{\circ+22}_{-18}$	$65.2^{\circ+11.4}_{-13.0}$
					[65.29]
^{14}Be	4.1±0.5	2.8±0.4	$72^{\circ+16}_{-13}$	$64^{\circ+9}_{-10}$	
^{12}Be	3.0±0.6	1.9±0.4	$77^{\circ+23}_{-22}$		
^{18}C	2.6±0.7	1.6±0.4	$78^{\circ+30}_{-27}$		
^{20}C	2.8±0.3	2.0±0.2	$70^{\circ+11}_{-11}$		
	2.7±0.2	1.8±0.1	$74^{\circ+7}_{-7}$		
^{20}C*	130±10	69±5	$87^{\circ+8}_{-9}$		

Table 4.2: Various two neutron opening angles of different $2n$ halo nuclei calculated from the results for the mean square radii shown. Compared with results of [Ber07] and [Hag07] shown in the last two columns, respectively.

lie within one error bar of each other. However, the size of these error bars suggest that further study should be done to improve both the experimental and theoretical results.

4.5 Conclusion

In this chapter, we have investigated universal aspects of three-body halo nuclei within an effective quantum mechanics approach to leading order. Assuming that the halo nuclei have resonant S-wave interactions between the neutron and the core, the effective potential at leading order reduces to a separable S-wave potential. We have shown that the renormalization of this potential to reproduce the scattering length is analogous to results using an EFT approach [Br06b]. The corrections at next-to- and next-to-next-to-leading order in the expansion in M_{low}/M_{high} are determined by the S-wave effective ranges [Ham01, Pl06a]. Corrections from P-wave interactions appear at even higher orders [Bed02]. An important improvement compared to previous calculations is the inclusion of error bands based on the omitted higher order terms in the effective theory.

We have calculated the parametric region within which at least one excited Efimov state will occur for different values of the core mass A. The boundary of this region is given by a curve in the plane described by the root of the ratio of the two-body bound(virtual) state energies to the ground state energy [Amo96]. We have calculated the boundary of this region for various values of the core mass A and provided error bands for the boundary curves. From the current experimental data, we conclude that none of the known halo nuclei is likely to have an excited Efimov state. One possible exception is ^{20}C which could have one excited state with a binding energy of less than 7 keV.

We have also studied the structure of known $2n$ halo nuclei, calculating the one- and two-body matter density form factors. From these form factors we were able to extract the mean square distances between the two particles in the chosen two-body subsystem, as well as the mean square distance of the spectator particle from the center of mass. We found that our results for the n-n mean square radii agree well with the experimental data for the *Borromean* halo nuclei ^{11}Li and ^{14}Be [Mar00]. We have explicitly not studied the case of ^{6}He, which is dominated by a P-wave resonance in the n-c interaction ("^{5}He") and requires a different counting scheme. While various schemes to treat such P-wave resonances in EFT have been developed [Ber02, Bed03b], their application to three-body systems remains to be worked out. To the expected accuracy, our effective theory gives a good description of the studied halo nuclei. Using our results for the mean square distances, we have also calculated the two neutron opening angle, and found a good general agreement with the recent results of [Ber07] and [Hag07].

Throughout this work, we have estimated the theoretical error of the leading order effective potential, Eq. (4.2). This uncertainty was quantified in our results through error bands. In the next chapter, we will systematically improve the theoretical error through the inclusion of a momentum dependent next-to-leading order term in the effective potential which can be matched to the effective range of the interaction.

Another interesting application of this effective theory will be the study of Coulomb excitation data from existing and future facilities with exotic beams (such as FAIR and FRIB). In these experiments a nuclear beam scatters off the Coulomb field of a heavy nucleus. Such processes can populate excited states of the projectile which subsequently decay, leading to its "Coulomb dissociation" [Ber88]. Effective theories offer a systematic framework for a full quantum-mechanical treatment of these reactions. In summary, with new improved experimental data for these weakly bound nuclei, much more knowledge can be obtained about the structure of these interesting systems as well as discovering whether they show universal behavior and excited Efimov states.

Chapter 5

Three-Body Halo Nuclei to Next-to-Leading Order

In principle, the low-energy behavior of a few-body system with a scattering length $|a|$ much larger than the range R of the underlying two-body interaction can be described up to an arbitrary level of accuracy proportional to powers of the low-momentum scale M_{low} over the high-momentum scale M_{high} [Br06b]. This is achieved by taking advantage of the separation of scales inherent in the system, thereby using the ratio $R/|a|$ as a small expansion parameter in perturbative calculations. The theoretical uncertainty can then be systematically improved by including increasingly higher order terms in the expansion. In this chapter, we improve upon the results of the previous chapter by including the momentum dependent next-to-leading order (NLO) term in a short-range effective potential made up of contact interactions. At this order, the effective range r_0 of the two-body interaction comes into play. We should, therefore, be able to predict effective range corrections to low-energy results up to a precision given by $(r_0/a)^2 \sim (M_{low}/M_{high})^2$.

Effective field theories with contact interactions have already been used to study the NLO range corrections to various few-body systems with a large scattering length, mostly focused on the three-nucleon system. The range corrections to S-wave neutron-deuteron scattering in the doublet channel were calculated in perturbation theory in Ref. [Ham01]. In Refs. [Bed03a, Pl06a, Pl06b], low-energy observables in the three-nucleon system were calculated up to next-to-next-to-leading order (N2LO) with a formalism using the resummation of range effects. Also, the three-body recombination of atoms with a large scattering length were calculated with effective range corrections in a similar EFT in Ref. [Ham06]. For a more exhaustive list of such NLO studies, see Ref. [Bed03a] and references therein.

There has also been interest lately in calculating the effective range corrections to the Efimov effect for three identical bosons. The study done by Thøgersen et al. [Thog08] focused on the range corrections for ultracold atoms caught in an optical trap. Also, an effective theory, using once-subtracted momentum-space integral equations, has explored the corrections to the Efimov spectrum linear in r_0 [Pl08]. It was

shown that discrete scale invariance connects the relative corrections for different Efimov states through a discrete scaling factor related to the factor found in the well known LO results [Br06b] (also see Sec. 4.3.1). In this chapter, we critically examine these studies, using an extension of the effective theory derived to leading order in the previous chapter. While this is very similar to the work done in Ref. [Pl08], our approach allows for further analysis of the linear range corrections to the Efimov spectrum (Sec. 5.3.1). We also explore the effective range corrections to the structure of Efimov states, specifically looking at the corrections to the mean square distance of the spectator particle from the center of mass, as well as the mean square distance of the two particles in the two-body dimer subsystem (Sec. 5.3.2).

As mentioned before, the first experimental evidence of the Efimov effect has recently been found in ultracold Cesium atoms through their signature in three-body recombination rates [Kr06]. There appears a resonant enhancement of the measured recombination rate in the lowest hyperfine state of ultracold ^{133}Cs atoms at $a \sim -850a_0$, due to the presence of an Efimov trimer at the three-body threshold. Effective field theories using a zero-range model have been very successful at describing this data [Br04a, Br08c]. Other more recent experiments have possibly found evidence of Efimov states for both positive and negative scattering lengths in various ultracold atom experiments [Kn08, Ot08, Hu08, Ba09]. In order to provide a more precise theoretical representation of these results, it is important to improve our understanding of the effective range dependence of the Efimov spectrum.

While these NLO corrections to the Efimov effect for three identical bosons are very interesting, we also are interested in the corrections to $2n$ halo nuclei results arising from a non-zero effective range. The effective range of the neutron-neutron interaction has been measured to be $r_{nn} = (2.75 \pm 0.11)$ fm [Mi90], which is of the same order of magnitude as the natural low-energy length scale of the halo nucleus system, as defined by the pion mass scale: $\ell \approx \hbar/m_\pi c = 1.4$ fm. However, the effective ranges for the various neutron-core interactions of $2n$ halo nuclei are not well known. We therefore estimate r_{nc} to also be of the order of the low-energy length scale and use the inverse of the pion mass: $r_{nc} \approx 1.4$ fm. We can then use this estimate for the effective range to calculate the NLO corrections to the results of the previous chapter. We discuss the impact that the inclusion of the effective range has on the possibility of known $2n$ halo nuclei to have an excited Efimov state, and look at the corrections to the binding energy of a possible ^{20}C excited state (Sec. 5.4.1). We then calculate the shift in the mean square radii of various halo nuclei due to the non-zero effective range (Sec. 5.4.2).

The structure of this chapter is as follows: We start with a detailed look into the underlying two-body system (Sec. 5.1), first deriving the NLO T-matrix from the effective potential, including the rather involved process of renormalization (Sec. 5.1.1). We then discuss important features of the two-body effective theory: the T-matrix pole structure in Sec. 5.1.2, an important constraint on the effective range known as the *Wigner Bound* in Sec. 5.1.3, and the renormalization group behavior of our NLO effective theory in Sec. 5.1.4. We then use the two-body T-matrix result in the three-

body Faddeev equations in Sec. 5.2. However, to properly renormalize the three-body problem, we also must add a three-body force term to the Faddeev equations, which we do analogously to an EFT formalism [Br06b]. After this, the results for the NLO corrections to the Efimov effect for three identical bosons are shown in Sec. 5.3, and the NLO results for $2n$ halo nuclei in Sec. 5.4. We end the chapter with conclusions.

5.1 The Two-Body NLO T-Matrix

In this section, we focus on the short-range two-body interaction, taken to next-to-leading order (NLO), which will be used to describe the interactions between the pairs of particles in the subsystems of the three-body problem. Due to divergences in the theory, a process of renormalization must be performed in order to reproduce physical low-energy observables. Starting from an effective interaction potential, the process of renormalization is used in deriving the interaction T-matrix (Sec. 5.1.1). Important to physical applications and the numerical calculations is the pole structure of the T-matrix, which we describe in Sec. 5.1.2. In the following section, Sec. 5.1.3, we detail an important restriction found for the parameters of the T-matrix which results from our renormalization procedure. Finally, the renormalization of the S-wave interaction can be understood in terms of a renormalization group, which we describe in Sec. 5.1.4.

5.1.1 The NLO Effective Potential

We are now interested in extending the effective quantum mechanics framework of Refs. [Ca08, Pl05, Pl04a, Pl04b] to the next-to-leading order (NLO). The low-energy behavior of the system will then be reproduced with a level of accuracy proportional to the low-momentum scale M_{low} over the high-momentum scale M_{high} squared. For this level of accuracy, we require two coupling parameters C_0 and C_2 tuned to reproduce the scattering length a and effective range r_0 of the interaction.

We, therefore, return to the effective interaction potential introduced in Sec. 4.1, but include the NLO interaction in the momentum expansion:

$$\langle \vec{p} \mid V_{eff} \mid \vec{p}' \rangle = g(p)g(p')(C_0 + C_2(p^2 + p'^2) + \dots), \tag{5.1}$$

where the dots indicate even higher order momentum dependent interactions. The potential can be written in a more explicitly separable form as a matrix equation:

$$\begin{aligned} \langle \vec{p} \mid V_{eff} \mid \vec{p}' \rangle &= g(p)g(p') \begin{pmatrix} 1 & p^2 \end{pmatrix} \begin{pmatrix} C_0 & C_2 \\ C_2 & 0 \end{pmatrix} \begin{pmatrix} 1 \\ p'^2 \end{pmatrix} && (5.2) \\ &= g(p)g(p')v_\mu^T(p^2)\mathbf{C}_{\mu\nu}v_\nu(p'^2), && (5.3) \end{aligned}$$

where we have defined the coupling parameter matrix $\mathbf{C}_{\mu\nu}$, and momentum dependent column vector $v_\mu(p^2)$. We assume Einstein's summation convention throughout.

As in the previous chapter, $g(p)$ is the regulator function (sometimes called the form factor) of the theory. Of course, the low-energy observables must be independent of the regularization scheme, and one can choose the scheme most convenient for calculations. In this section focusing on the two-body system, we continue to use a momentum cutoff scheme, multiplying the coupling constants with the Gaussian regulator function $g(p) = \exp(-p^2/\Lambda^2)$, where Λ is the cutoff parameter. This regulator function suppresses the contributions of momenta $p, p' \gg \Lambda$, where the effective potential would break down and no longer be valid. However, when we later move on to the three-body system, it will become more convenient to use a strong cutoff regularization technique, in which the effective potential is set to zero for momenta greater than Λ. The strong cutoff allows a simpler inclusion of a three-body force term. The details for switching to a strong cutoff from the Gaussian regulator are discussed in Sec. 5.2.2. A natural choice for the value of Λ is $\Lambda \sim M_{high}$, but observables are independent of Λ after renormalization, up to higher order corrections which scale with $1/\Lambda$. However, there is an interesting constraint on Λ depending on the value of the effective range r_0 known as the *Wigner Bound*. This condition is discussed in detail in Sec. 5.1.3.

One convenient property of a separable potential is that the two-body scattering amplitude, known as the T-matrix, can be solved exactly. However, inclusion of the NLO interaction makes the derivation of the T-matrix more complicated. We start with the definition of the T-matrix through the Lippmann-Schwinger equation:

$$\begin{aligned} T(\vec{p},\vec{p}') &\equiv \langle \vec{p} \mid t \mid \vec{p}' \rangle = V(\vec{p},\vec{p}') + \int d^3q \, \frac{V(\vec{p},\vec{q})}{E - \frac{q^2}{2\mu} + i\epsilon} T(\vec{q},\vec{p}') \\ &= g(p)g(p')v_\mu^T(p^2)\mathbf{C}_{\mu\nu}v_\nu(p'^2) \\ &\quad + g(p)v_\mu^T(p^2)\mathbf{C}_{\mu\nu}\int d^3q \, \frac{g(q)v_\nu(q^2)}{E - \frac{q^2}{2\mu} + i\epsilon} T(\vec{q},\vec{p}') \qquad (5.4) \\ &= g(p)g(p')v_\mu^T(p^2)\mathbf{C}_{\mu\nu}v_\nu(p'^2) + g(p)v_\mu^T(p^2)\mathbf{C}_{\mu\nu}B_\nu, \qquad (5.5) \end{aligned}$$

where in the last line we have introduced an intermediate column vector function B_ν. When we iterate Eq. (5.4) once, we can by comparison find an iterative relation for B_ν:

$$\begin{aligned} B_\nu &= \int d^3q \, \frac{g(q)^2 v_\nu(q^2)v_\rho^T(q^2)}{E - \frac{q^2}{2\mu} + i\epsilon} g(p')\mathbf{C}_{\rho\sigma}v_\sigma(p'^2) \\ &\quad + \int d^3q \, \frac{g(q)^2 v_\nu(q^2)v_\rho^T(q^2)}{E - \frac{q^2}{2\mu} + i\epsilon} \mathbf{C}_{\rho\sigma}B_\sigma \\ &= g(p')\mathbf{A}_{\nu\rho}\mathbf{C}_{\rho\sigma}v_\sigma(p'^2) + \mathbf{A}_{\nu\rho}\mathbf{C}_{\rho\sigma}B_\sigma, \qquad (5.6) \end{aligned}$$

where we have now defined the integral as a matrix function $\mathbf{A}_{\nu\rho}$. We will return to the exact form of $\mathbf{A}_{\nu\rho}$ shortly. First, we solve for the column vector B. After some manipulation using the properties of matrix multiplication we find

$$B_\lambda = g(p')(\mathbf{1} - \mathbf{AC})^{-1}_{\lambda\nu}\mathbf{A}_{\nu\rho}\mathbf{C}_{\rho\sigma}v_\sigma(p'^2). \tag{5.7}$$

Substituting this back into the Lippmann-Schwinger equation, Eq. (5.5), after some more manipulation using matrix multiplication, we find a solution for the T-matrix:

$$T(\vec{p},\vec{p}') = g(p)g(p')v^T_\mu(p^2)(\mathbf{C}^{-1} - \mathbf{A})^{-1}_{\mu\nu}v_\nu(p'^2). \tag{5.8}$$

Here we see that the T-matrix of the NLO separable potential is again separable. Also, the similarities and reduction to the LO result can be seen through comparison with Eq. (4.9).

We now return to the definition of the $\mathbf{A}_{\mu\nu}$ integral matrix. We write $\mathbf{A}_{\mu\nu}$ in its matrix form by multiplying the vectors $v_\mu(q^2)v^T_\nu(q^2)$ and simplify by performing the trivial angular integration:

$$\begin{aligned}\mathbf{A}_{\mu\nu} &= 4\pi 2\mu \int_0^\infty dq\, \frac{q^2 \exp\left(\frac{-2q^2}{\Lambda^2}\right)}{2\mu E - q^2 + i\epsilon} \begin{pmatrix} 1 & q^2 \\ q^2 & q^4 \end{pmatrix} \\ &\equiv \begin{pmatrix} A_1 & A_2 \\ A_2 & A_3 \end{pmatrix}. \end{aligned} \tag{5.9}$$

Since we will be chiefly concerned with bound states, we can assume that $E < 0$ and we can solve for the A_i integrals. The derivation of the recursive relationship between the A_i integrals, as well as the solutions related to the complementary error function can be found in App. A. Each A_i integral includes terms proportional to powers of the cutoff, which diverge in the limit $\Lambda \to \infty$. These are high-energy effects which can be removed through a process of renormalization, first redefining the coupling parameters until we have a form for the T-matrix which is suitable for matching to low-energy observables.

We start this process by substituting in the definitions for the column vectors $v(p^2)$ and the matrices $\mathbf{A}$ and $\mathbf{C}$ and performing the multiplications in Eq. (5.8). We also assume the on-shell condition for the two-body T-matrix, $p^2 = p'^2 = 2\mu E$. This gives a new form for the NLO interaction T-matrix:

$$T(\vec{p},\vec{p}') = g(p)g(p')\frac{C_0 + 2C_2 2\mu E + C_2^2(A_3 - 2A_2 2\mu E + A_1(2\mu E)^2)}{1 - C_0A_1 - 2C_2A_2 - C_2^2(A_1A_3 - A_2^2)}. \tag{5.10}$$

As a next step, we substitute the solutions for the A_i integrals, found in App. A, into the T-matrix. Looking only at the numerator of the above equation, we find that most of the Λ dependent terms cancel each other and we are left with:

$$\begin{aligned} &C_0 + 2C_2 2\mu E + C_2^2(A_3 - 2A_2 2\mu E + A_1(2\mu E)^2) = \\ &C_0 - 2\pi^2 2\mu C_2^2\, 3\left(\tfrac{\Lambda}{2}\right)^5\sqrt{\tfrac{2}{\pi}} + 2\mu E\left(2C_2 + 2\pi^2 2\mu C_2^2\left(\tfrac{\Lambda}{2}\right)^3\sqrt{\tfrac{2}{\pi}}\right). \end{aligned} \tag{5.11}$$

Here we see two terms dependent on Λ which represent high-energy effects. Since all such effects should be described by the coupling parameters, we can redefine the C's to absorb these terms:

$$C_0^R \equiv C_0 - 2\pi^2 2\mu C_2^2\, 3\left(\frac{\Lambda}{2}\right)^5 \sqrt{\frac{2}{\pi}}, \tag{5.12}$$

$$2C_2^R \equiv 2C_2 + 2\pi^2 2\mu C_2^2 \left(\frac{\Lambda}{2}\right)^3 \sqrt{\frac{2}{\pi}}. \tag{5.13}$$

With these redefined coupling parameters, we rewrite Eq. (5.11) in a compact form:

$$C_0 + 2C_2 2\mu E + C_2^2(A_3 - 2A_2 2\mu E + A_1(2\mu E)^2) = C_0^R\left[1 + 2\frac{C_2^R}{C_0^R}2\mu E\right], \tag{5.14}$$

and we notice that the redefinitions simply absorbed the terms proportional to C_2^2 on the left hand side of the equation. The redefinitions work in the same way on the denominator of the T-matrix, Eq. (5.10), absorbing the high-energy effects that arise from the terms proportional to C_2^2:

$$1 - C_0 A_1 - 2C_2 A_2 - C_2^2(A_1 A_3 - A_2^2) = 1 - C_0^R A_1 - 2C_2^R A_2. \tag{5.15}$$

For the next step in redefining the coupling parameters, we substitute the solutions of A_1 and A_2, found in App. A, into the above equation for the denominator of the T-matrix which we then write in the following form:

$$\begin{aligned} 1 - C_0^R A_1 - 2C_2^R A_2 \;=\; & -2\pi^2 2\mu C_0^R \left[-\left(\frac{1}{2\pi^2 2\mu C_0^R} + 2\frac{C_2^R}{C_0^R}\left(\frac{\Lambda}{2}\right)^3\sqrt{\frac{2}{\pi}}\right)\right. \\ & \left. -\left(1 + 2\frac{C_2^R}{C_0^R}2\mu E\right)\left(\left(\frac{\Lambda}{2}\right)\sqrt{\frac{2}{\pi}} - \sqrt{-2\mu E}\exp\left(\tilde{x}^2\right)\operatorname{erfc}\left(\tilde{x}\right)\right)\right], \end{aligned} \tag{5.16}$$

where, for brevity, we have defined the variable $\tilde{x}$:

$$\tilde{x} \equiv \frac{\sqrt{2(-2\mu E)}}{\Lambda}. \tag{5.17}$$

Here we have another term dependent on Λ which contributes only to the high-energy effects and can be absorbed into the coupling parameters by a second redefinition:

$$\frac{1}{2\pi^2 2\mu C_0^{R_2}} \equiv \frac{1}{2\pi^2 2\mu C_0^R} + 2\frac{C_2^R}{C_0^R}\left(\frac{\Lambda}{2}\right)^3\sqrt{\frac{2}{\pi}}, \tag{5.18}$$

$$\frac{1}{2\pi^2 2\mu C_2^{R_2}} \equiv \frac{1}{2\pi^2 2\mu C_2^R} + 2\left(\frac{\Lambda}{2}\right)^3\sqrt{\frac{2}{\pi}}, \tag{5.19}$$

where the second redefinition of C_2 was done so that

$$\frac{C_2^{R_2}}{C_0^{R_2}} = \frac{C_2^R}{C_0^R}. \tag{5.20}$$

These are the final redefinitions of the coupling parameters that can be performed in order to absorb high-energy effects arising from cutoff dependent terms in the T-matrix.

Now that we have derived relations for the numerator, Eq. (5.14), and the denominator, Eq. (5.16), of the T-matrix, we apply the second redefinitions of the coupling parameters and find the following form for the interaction T-matrix:

$$\begin{aligned} T(\vec{p},\vec{p}') &= g(p)g(p')\frac{-1}{2\pi^2 2\mu}\left[1+2\frac{C_2^{R_2}}{C_0^{R_2}}2\mu E\right] \\ &\quad\times\left[\frac{-1}{2\pi^2 2\mu C_0^{R_2}} - \frac{\Lambda}{2}\sqrt{\frac{2}{\pi}} + \sqrt{-2\mu E}\exp\left(\tilde{x}^2\right)\operatorname{erfc}\left(\tilde{x}\right)\right. \\ &\quad\left.-2\frac{C_2^{R_2}}{C_0^{R_2}}2\mu E\left(\left(\frac{\Lambda}{2}\right)\sqrt{\frac{2}{\pi}} - \sqrt{-2\mu E}\exp\left(\tilde{x}^2\right)\operatorname{erfc}\left(\tilde{x}\right)\right)\right]^{-1} \qquad (5.21) \\ &= g(p)g(p')\frac{-1}{2\pi^2 2\mu}\left[\frac{-1}{2\pi^2 2\mu C_0^{R_2}}\frac{1}{1+2\frac{C_2^{R_2}}{C_0^{R_2}}2\mu E}\right. \\ &\quad\left.-\frac{\Lambda}{2}\sqrt{\frac{2}{\pi}} + \sqrt{-2\mu E}\exp\left(\tilde{x}^2\right)\operatorname{erfc}\left(\tilde{x}\right)\right]^{-1}. \qquad (5.22) \end{aligned}$$

We have written the T-matrix in the two different forms above because each form is useful in certain applications. The second form will be used in the process of renormalization, in order to match the coupling parameters to the scattering length a and the effective range r_0. After this renormalization, the resulting relations will be substituted into the first form to give our final result for the two-body S-wave T-matrix to NLO.

We wish to renormalize our NLO theory by tuning the coupling parameters to reproduce the first two parameters in the effective range expansion. The effective range expansion is an expansion of the inverse of the T-matrix in powers of the two-body energy. Therefore, we expand the denominator of Eq. (5.22) up to NLO, ignoring terms of E^2 and higher. This is done by the following binomial expansion:

$$\frac{1}{1+2\frac{C_2^{R_2}}{C_0^{R_2}}2\mu E} = 1 - 2\frac{C_2^{R_2}}{C_0^{R_2}}2\mu E + O(E^2) + \dots . \tag{5.23}$$

This is then substituted into Eq. (5.22), and terms of like order in E are collected:

$$T^{-1} \propto -\left[\frac{1}{2\pi^2 2\mu C_0^{R_2}} + \left(\frac{\Lambda}{2}\right)\sqrt{\frac{2}{\pi}}\right] + 2\frac{C_2^{R_2}}{2\pi^2 2\mu (C_0^{R_2})^2} 2\mu E + \sqrt{-2\mu E}\exp\left(\tilde{x}^2\right)\mathrm{erfc}\left(\tilde{x}\right) + O(E^2) + \dots . \tag{5.24}$$

We now require a suitable form of the effective range expansion which also includes the effects of the Gaussian regulator functions, which appear in the T-matrix through the $\exp(\tilde{x}^2)\mathrm{erfc}(\tilde{x})$ factor. Specifically, the effective range expansion should reproduce the same pole structure, while including the regulator effects. By comparing with the LO result, Eq (4.15), we write an analogous form of the inverse T-matrix, but include the NLO term in the expansion:

$$T^{-1} \propto -\frac{1}{a}\exp\left(\tilde{x}_0^2\right)\mathrm{erfc}\left(\tilde{x}_0\right) + \frac{r_0}{2} 2\mu E \exp\left(\tilde{x}_0^2\right)\mathrm{erfc}\left(\tilde{x}_0\right) + \sqrt{-2\mu E}\exp\left(\tilde{x}^2\right)\mathrm{erfc}\left(\tilde{x}\right) + O(E^2) + \dots , \tag{5.25}$$

where we define $\tilde{x}_0$ in the same way as $\tilde{x}$:

$$\tilde{x}_0 \equiv \frac{\sqrt{2(-2\mu E_2)}}{\Lambda}, \tag{5.26}$$

with E_2 the pole of the effective range expanded two-body T-matrix up to the NLO term. In other words, $E_2 < 0$ is the solution of

$$0 = -\frac{1}{a} + \frac{r_0}{2} 2\mu E_2 + \sqrt{-2\mu E_2}. \tag{5.27}$$

A more detailed discussion of the pole structure, with its implications to the two-body systems involved in $2n$ halo nuclei will be given in Sec. 5.1.2.

By matching the like terms in Eqs. (5.24, 5.25), we find the relations needed to tune the coupling parameters to reproduce low-energy observables, specifically the S-wave scattering length and effective range. The LO coupling parameter as a function of the cutoff $C_0^{R_2}(\Lambda)$ can be related to the scattering length:

$$\frac{1}{C_0^{R_2}} = 2\pi^2 2\mu \left[\frac{1}{a}\exp\left(\tilde{x}_0^2\right)\mathrm{erfc}\left(\tilde{x}_0\right) - \left(\frac{\Lambda}{2}\right)\sqrt{\frac{2}{\pi}}\right], \tag{5.28}$$

which is analogous to the LO result, Eq. (4.12), except now the pole in the two-body system is calculated to the NLO, including corrections from the effective range parameter. As expected, if $r_0 = 0$, then $2\mu E_2 = 1/a^2$, and Eq. (5.28) reduces exactly to Eq. (4.12).

For the effective range parameter r_0 we match the terms proportional to $2\mu E$ to find the relation:

$$\frac{r_0}{2}\exp\left(\tilde{x}_0^2\right)\mathrm{erfc}\left(\tilde{x}_0\right) = 2\frac{C_2^{R_2}}{2\pi^2 2\mu (C_0^{R_2})^2}. \tag{5.29}$$

Therefore, using the relation between $C_0^{R_2}(\Lambda)$ and a, we can relate $C_2^{R_2}(\Lambda)$ to r_0:

$$C_2^{R_2} = \frac{1}{4\pi^2 2\mu}\left[\frac{\frac{r_0}{2}\exp\left(\tilde{x}_0^2\right)\mathrm{erfc}\left(\tilde{x}_0\right)}{\left(\frac{1}{a}\exp\left(\tilde{x}_0^2\right)\mathrm{erfc}\left(\tilde{x}_0\right) - \left(\frac{\Lambda}{2}\right)\sqrt{\frac{2}{\pi}}\right)^2}\right], \tag{5.30}$$

which leads to the useful relation:

$$2\frac{C_2^{R_2}}{C_0^{R_2}} = \frac{\frac{r_0}{2}\exp\left(\tilde{x}_0^2\right)\mathrm{erfc}\left(\tilde{x}_0\right)}{\frac{1}{a}\exp\left(\tilde{x}_0^2\right)\mathrm{erfc}\left(\tilde{x}_0\right) - \left(\frac{\Lambda}{2}\right)\sqrt{\frac{2}{\pi}}}. \tag{5.31}$$

These results are analogous to the findings of EFT using a strong cutoff regularization scheme [Br06b].

Using these relations, for a chosen Λ, we can determine what values of $C_0^{R_2}$ and $C_2^{R_2}$ will reproduce the experimentally determined values of a and r_0. Due to the dependence of both coupling parameters on E_2, which is of course dependent on a and r_0, both C's must be tuned in order to reproduce these low-energy observables to this order. However, if Λ is large compared to the momentum scale of the pole $\Lambda \gg \sqrt{2\mu E_2}$, then $\exp(\tilde{x}_0^2)\mathrm{erfc}(\tilde{x}_0) \to 1$ and only $C_0^{R_2}$ must be tuned in order to reproduce the scattering length a. Once this is done, we can tune the value of $C_2^{R_2}$ in order to reproduce r_0.

With the potential now renormalized, we can return to the two-body T-matrix for an S-wave interaction to next-to-leading order. By substituting Eqs. (5.28, 5.31) into Eq. (5.21) we find for $E < 0$:

$$\begin{aligned} T(\vec{p},\vec{p}') &= g(p)g(p')\frac{-1}{2\pi^2 2\mu}\left(1 - 2\mu E\frac{\frac{r_0}{2}\exp(\tilde{x}_0^2)\mathrm{erfc}(\tilde{x}_0)}{\left(\frac{\Lambda}{2}\right)\sqrt{\frac{2}{\pi}} - \frac{1}{a}\exp(\tilde{x}_0^2)\mathrm{erfc}(\tilde{x}_0)}\right) \\ &\quad\times\left[-\frac{1}{a}\exp(\tilde{x}_0^2)\mathrm{erfc}(\tilde{x}_0) + \sqrt{-2\mu E}\exp(\tilde{x}^2)\mathrm{erfc}(\tilde{x})\right. \\ &\quad\left.+\frac{r_0}{2}\exp(\tilde{x}_0^2)\mathrm{erfc}(\tilde{x}_0)2\mu E\left(\frac{\left(\frac{\Lambda}{2}\right)\sqrt{\frac{2}{\pi}} - \sqrt{-2\mu E}\exp(\tilde{x}^2)\mathrm{erfc}(\tilde{x})}{\left(\frac{\Lambda}{2}\right)\sqrt{\frac{2}{\pi}} - \frac{1}{a}\exp(\tilde{x}_0^2)\mathrm{erfc}(\tilde{x}_0)}\right)\right]^{-1}. \end{aligned} \tag{5.32}$$

If the cutoff is chosen large compared to all momentum scales involved in the problem: $\Lambda \gg 1/|a|, \sqrt{2\mu E}, \sqrt{2\mu E_2}$, this T-matrix reproduces the usual effective range expansion at next-to-leading order.

5.1.2 The NLO T-Matrix Pole Structure

In this subsection, we discuss the pole structure of the S-wave T-matrix in the NLO effective range expansion. We also discuss the implications that this pole structure has on $2n$ halo nuclei with large scattering lengths, and how the pole structure of the full NLO two-body T-matrix found in Eq. (5.32) changes with a finite cutoff.

The value of the T-matrix pole E_2 is important to our theory, as it is needed as a parameter arising from the regularization scheme (see Eqs. (5.26, 5.27)). The position of the poles to NLO is dependent on the value of the scattering length a and the effective range parameter r_0. The poles found in momentum space κ are the solutions of the quadratic equation:

$$0 = -\frac{1}{a} + \frac{r_0}{2}\kappa^2 - i\kappa, \tag{5.33}$$

which has the two solutions:

$$\kappa = i\gamma_\pm \quad \text{where} \quad \gamma_\pm = \frac{1 \pm \sqrt{1 - 2r_0/a}}{r_0}. \tag{5.34}$$

As long as $2r_0/a < 1$, $\gamma_\pm$ are both real, and the poles lie on the imaginary axis. For $\gamma_\pm > 0$ the pole is on the positive imaginary axis, corresponding to a two-body bound state at energy $2\mu B_2 = \gamma_\pm^2$. For $\gamma_\pm < 0$, the pole is on the negative imaginary axis, corresponding to a two-body virtual state at energy $2\mu E_v = \gamma_\pm^2$.

Three-body halo nuclei are characterized by their large S-wave scattering lengths compared to the range of the interaction, $a \gg r_0$. For this case we find that one of the poles always appears in the high-momentum region, where our theory breaks down and is no longer valid. This is most easily seen by taking the expansion of $\gamma_\pm$ for small r_0/a:

$$\gamma_+ = \frac{2}{r_0} - \frac{1}{a}\left(1 + \frac{r_0}{2a} + O(r_0^2/a^2) + \ldots\right), \tag{5.35}$$

$$\gamma_- = \frac{1}{a}\left(1 + \frac{r_0}{2a} + O(r_0^2/a^2) + \ldots\right). \tag{5.36}$$

For $a \gg r_0$, γ_+ is in the high-momentum region. We, therefore, set the value of $E_2 < 0$ needed in our full NLO T-matrix, Eq. (5.32), using the γ_- pole

$$|2\mu E_2| = \left(\frac{1 - \sqrt{1 - 2r_0/a}}{r_0}\right)^2. \tag{5.37}$$

For $a > 0 (a < 0)$, this pole lies on the positive(negative) imaginary axis, corresponding to a two-body bound(virtual) state with two-body energy $B_2 = E_2 (E_v = E_2)$. In the LO limit, $r_0 = 0$, this reduces exactly to the universal formula for the two-body binding energy given in Eq. (4.1).

In the cases where $r_0 < 0$, the γ_+ pole gives rise to a virtual state, which decreases from infinity as $|r_0|$ is increased. On the other hand, when $r_0 > 0$, the γ_+ pole is a simple bound state, starting at infinity and decreasing quickly as r_0 increases. For the condition $a \gg r_0$, this bound state stays in the high-momentum region and can be ignored. However, it can cause numerical problems in calculations using the NLO effective range expansion for values of $r_0 \to a/2$.

For completeness, in the case $2r_0/a > 1$, we see from Eq. (5.34), that the poles become a complex conjugate pair with solutions:

$$\gamma_\pm = \frac{1}{r_0} \pm i\frac{\sqrt{2r_0/a - 1}}{r_0}. \tag{5.38}$$

These complex-conjugated poles generate a resonance in the phase shift, centered around an energy $2\mu E_r = 2/ar_0$. Just such a case occurs with the $2n$ halo nucleus ^{6}He, in the α-n two-body subsystem, according to the partial wave analysis done in Ref. [Arn73]. This agrees with the absence of a ^{5}He bound state, although the S-wave scattering length is positive. The α-n scattering is dominated by a resonant P-wave, and, therefore, a study of the ^{6}He halo nucleus is not done explicitly here. The case $2r_0/a > 1$ is not dealt with in this work, as it does not fulfill the condition of large scattering length compared to the range of the interaction, $a \gg r_0$, and therefore, can not be accurately described by our effective theory.

As stated before, the NLO T-matrix found from the effective potential with Gaussian regulator functions, Eq. (5.32), reproduces the effective range expansion in the limit that the cutoff $\Lambda \to \infty$, and therefore, in this limit, has the same pole structure described above. However, for a finite cutoff, the pole structure changes, most importantly the position of the high-energy bound state pole γ_+, which appears for $r_0 > 0$. As Λ decreases from infinity, the magnitude of this bound state pole increases, and another simple pole appears from infinity and decreases toward γ_+^2. At a particular value of the cutoff Λ_B the two poles annihilate each other. For values of $\Lambda < \Lambda_B$, there is no longer a pole in the high-energy region for the NLO T-matrix of Eq. (5.32). This is exactly the expected effect of a momentum cutoff. A finite cutoff suppresses the details of the potential for momentum larger than Λ, and thus at some sufficiently small value of Λ the high-energy pole is destroyed. The position of Λ_B for various values of a, r_0 has been numerically calculated and found to be, within a certain level of accuracy, equal to the position of the Wigner bound, a constraint on the maximum value of the cutoff (see Sec. 5.1.3). Therefore, for the values of Λ allowed by the Wigner bound, no pole appears in the high-energy region for the NLO T-matrix of Eq. (5.32), and we do not have to worry about numerical difficulties arising from such a divergence.

While decreasing the cutoff from infinity eventually destroys the pole structure in the high-energy region, there is relatively little change in the pole found in the low-energy region. As desired, the position of the pole created by γ_- remains almost unchanged for sufficiently small values of r_0 as long as Λ is not so small as to enter the low-energy region.

5.1.3 The S-Wave Wigner Bound

It has been shown that the renormalization of an effective potential made up of contact interactions in a momentum expansion, regularized by a momentum cutoff scheme, as is the case of our effective potential, Eq. (5.1), can only be performed if certain constraints are placed on the effective range [Ph97]. Specifically, the effective range must be negative in the zero-range limit of the potential. This constraint follows directly from the general bound on the derivatives of the phase shifts derived first by Wigner in 1954 [Wig55], and is hence known as the *Wigner bound*. Wigner derived this bound from the fundamental principles of causality and unitarity, holding that a scattered wave cannot leave the scatterer before the incident wave has reached it.

A more recent study showed analytically the relation between the Wigner bound on the derivatives of phase shifts with the constraint on the effective range for short-range potentials [Ph96]. In this work it was shown explicitly that for any energy-independent potential in position space $V(r, r')$ which only acts up to a certain range R,

$$V(r, r') = 0 \quad \text{for all} \quad r, r' > R, \tag{5.39}$$

the effective range is bounded by

$$r_0 \;\leq\; 2\left(R - \frac{R^2}{a} + \frac{R^3}{3a^2}\right). \tag{5.40}$$

It is then obvious that for the zero-range limit, the effective range must be equal to or less than zero. It was also shown that this bound applies even if the potential does not go strictly to zero, but merely decreases fast enough for the wave function to approach the asymptotic solution sufficiently quickly. These position space arguments were then translated into momentum space in a following study [Ph97], and the $r_0 \leq 0$ bound for zero-range potentials was shown to hold true no matter how many terms in the momentum expansion are included in the potential.

We now show that the bound on the effective range can be derived straightforwardly in momentum space from the process of renormalization, done in Sec. 5.1.1, for our effective potential, Eq. (5.1).

In the renormalization process, the bare coupling constants C_0 and C_2 were redefined twice in order to absorb high-energy effects proportional to powers of the cutoff parameter. The exact form of the redefinitions are found in Eqs. (5.12, 5.13) and Eqs. (5.18, 5.19). The bare couplings are then related to the final couplings by:

$$C_0 = \frac{C_0^{R_2}}{1 - 4\pi^2 2\mu C_2^{R_2} \left(\frac{\Lambda}{2}\right)^3 \sqrt{\frac{2}{\pi}}} + 3\left(\frac{\Lambda}{2}\right)^5 \sqrt{\frac{2}{\pi}} 2\pi^2 2\mu C_2^2, \tag{5.41}$$

and

$$C_2 = \frac{1}{2\pi^2 2\mu \left(\frac{\Lambda}{2}\right)^3 \sqrt{\frac{2}{\pi}}} \left(-1 \pm \sqrt{\frac{1}{1 - 4\pi^2 2\mu C_2^{R_2} \left(\frac{\Lambda}{2}\right)^3 \sqrt{\frac{2}{\pi}}}}\right). \tag{5.42}$$

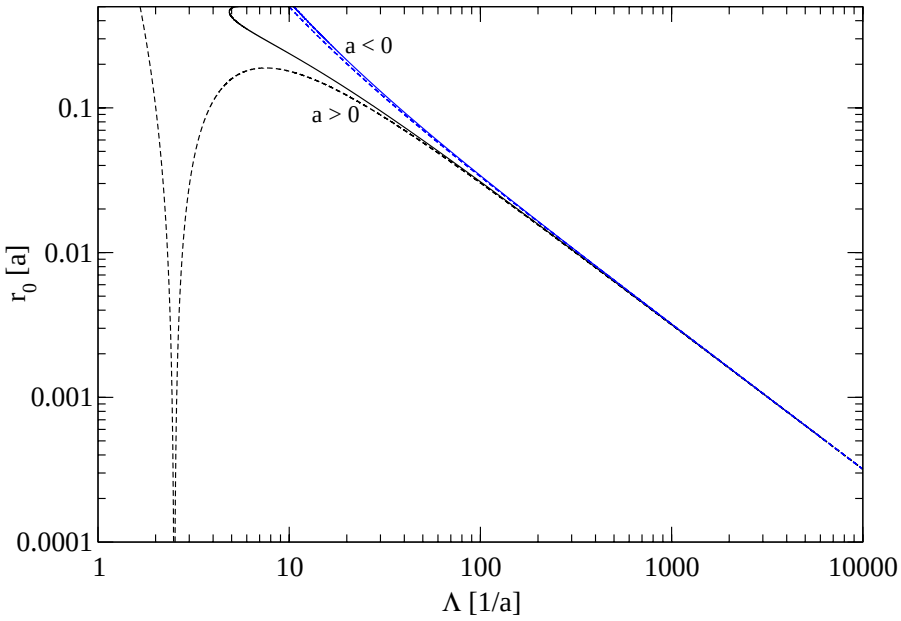

Figure 5.1: The Wigner bound, a constraint on the maximum value of the effective range r_0 depending on the value of the cutoff parameter Λ, or vice versa. Solid lines taken from Eq. (5.44) including the full effects of the Gaussian regulator scheme. Dashed lines taken from Eq. (5.45), the limit assuming large Λ. Upper(lower) curves found for negative(positive) scattering length.

Here one sees that there are real values of $C_2^{R_2}$ for which the bare couplings are complex. This would lead to an unphysical complex potential. Therefore, we must place a constraint on the value of $C_2^{R_2}$:

$$4\pi^2 2\mu C_2^{R_2} \left(\frac{\Lambda}{2}\right)^3 \sqrt{\frac{2}{\pi}} \;\leq\; 1. \tag{5.43}$$

The renormalization of the effective potential was completed by tuning the redefined coupling constants to reproduce the scattering length and the effective range. Substituting the expression which relates $C_2^{R_2}$ to a and r_0, Eq. (5.30), into the above equation, we find the Wigner bound on the effective range which results using a Gaussian regulator scheme:

$$\left(\frac{\Lambda}{2}\right)^3 \sqrt{\frac{2}{\pi}} \frac{\frac{r_0}{2}\exp\left(\tilde{x}_0^2\right)\operatorname{erfc}\left(\tilde{x}_0\right)}{\left(\frac{1}{a}\exp\left(\tilde{x}_0^2\right)\operatorname{erfc}\left(\tilde{x}_0\right) - \left(\frac{\Lambda}{2}\right)\sqrt{\frac{2}{\pi}}\right)^2} \leq 1, \tag{5.44}$$

where $\tilde{x}_0$ is a parameter dependent on Λ and the two-body T-matrix pole E_2, which in turn is dependent on a and r_0 (see Eq. (5.26), as well as Sec. 5.1.2). If the cutoff is much larger than the momentum scale of the T-matrix pole, $\Lambda \gg \sqrt{2\mu E_2}$, then

$\exp(\tilde{x}_0^2)\mathrm{erfc}(\tilde{x}_0) \to 1$ and we find a momentum space analog to Eq. (5.40):

$$r_0 \;\leq\; 2\left(\frac{2}{\Lambda}\sqrt{\frac{2}{\pi}} - \frac{8}{a\Lambda^2} + \frac{8}{a^2\Lambda^3}\sqrt{\frac{\pi}{2}}\right). \tag{5.45}$$

The Wigner bounds, comparing the results including the Gaussian regulator factors with the large cutoff limit, for both positive and negative scattering length, are displayed in Fig. 5.1.

5.1.4 The Renormalization Group

In this section, we analyze the renormalization of our two-body effective potential, done in Sec. 5.1.1, in terms of the *renormalization group* (RG). We follow the analysis of similar works on renormalization groups, Refs. [Kap98, Br06b]. These works assume the limit in which the cutoff parameter is much larger than the momentum scale of the two-body system, $\Lambda \gg \sqrt{2\mu E_2}$. For the Gaussian regulator scheme, this leads to the limit $\exp(\tilde{x}_0^2)\mathrm{erfc}(\tilde{x}_0) \to 1$. However, for the present analysis, we do not assume this limit, thereby including the regulator effects for small values of Λ.

First, we write the redefined coupling constants $C_0^{R_2}$ and $C_2^{R_2}$ in a dimensionless form:

$$\hat{C}_0(\Lambda) \equiv \frac{2\pi^2 2\mu\Lambda}{\sqrt{2\pi}} C_0^{R_2}\,, \qquad \hat{C}_2(\Lambda) \equiv \frac{4\pi 2\mu\Lambda^2}{r_0 \exp(\tilde{x}_0^2)\mathrm{erfc}(\tilde{x}_0)} C_2^{R_2}\,, \tag{5.46}$$

where the physical two-body system determines the fixed values for the reduced mass μ and the effective range r_0. The regulator parameter $\tilde{x}_0$, defined in Eq. (5.26), is proportional to the inverse of Λ and the square root of the two-body pole energy E_2, which in turn is dependent on a and r_0 (see Sec. 5.1.2 for details). Using the tuning equations for these coupling constants, Eqs. (5.28, 5.30), we find the relations:

$$\hat{C}_0(\Lambda) = -\frac{a\Lambda}{a\Lambda - \sqrt{2\pi}\exp(\tilde{x}_0^2)\mathrm{erfc}(\tilde{x}_0)}\,, \tag{5.47}$$

$$\hat{C}_2(\Lambda) = \left(\frac{a\Lambda}{a\Lambda - \sqrt{2\pi}\exp(\tilde{x}_0^2)\mathrm{erfc}(\tilde{x}_0)}\right)^2. \tag{5.48}$$

Here, the similarity between C_0 and C_2 can be seen as $\hat{C}_2 = \hat{C}_0^2$.

For a fixed scattering length a and effective range r_0, varying Λ produces the renormalization group trajectory for the dimensionless coupling constants. With the physical observables fixed, all points along a given trajectory correspond to the same physical two-body system. The trajectories for a few different values of r_0, for both positive and negative a are displayed in Fig. 5.2, in which all quantities are scaled with the magnitude of $|a|$. These are compared to the trajectories for which the limit

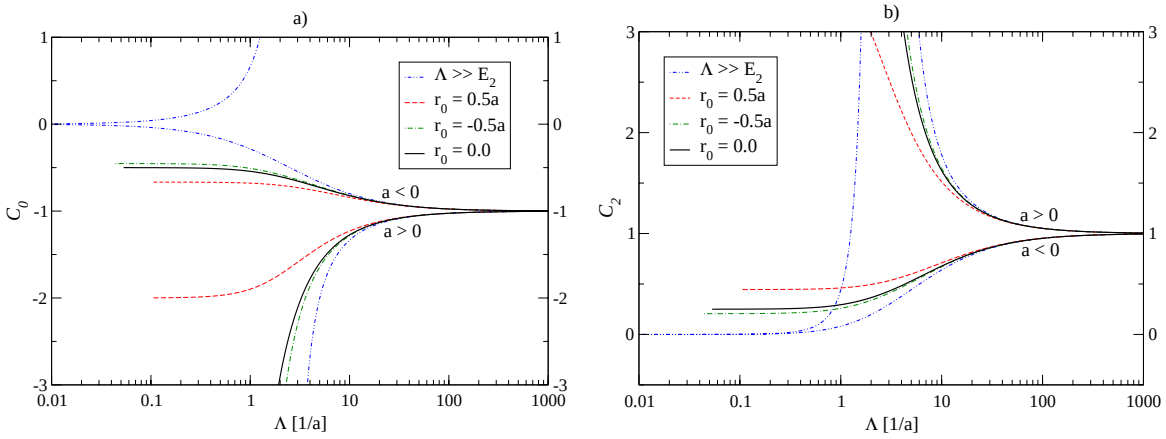

Figure 5.2: The dimensionless 2-body coupling constants a) $\hat{C}_0$ and b) $\hat{C}_2$ as functions of the ultraviolet cutoff Λ for both positive and negative scattering length a and several values of the effective range r_0; Solid(black): $r_0 = 0$, Dashed(red): $r_0 = 0.5a$, Dotted-dashed(dark green): $r_0 = -0.5a$. The double dotted-dashed(blue) lines correspond to the trajectories when Λ is always assumed to be larger than the momentum scale of the two-body system.

$\exp(\tilde{x}_0^2)\mathrm{erfc}(\tilde{x}_0) \to 1$ was taken (thin double dotted-dashed(blue) lines). For positive values of a with negative values of r_0 (and also for the vanishing $\tilde{x}_0$ limit), there is a divergence in both $\hat{C}_0$ and $\hat{C}_2$, while for negative values of a or positive values of r_0 there exists no such divergence.

One can see clearly the failure of the the vanishing $\tilde{x}_0$ limit for smaller values of Λ. When this limit is assumed both coupling constants vanish as the cutoff approaches zero. This was interpreted as a value of $\Lambda = 0$ corresponding to the noninteracting system with $a = 0$ [Br06b]. However, including the regulator effects we find that

$$\hat{C}_0 = \left(-1 + \frac{1}{a\sqrt{2\mu E_2}}\right)^{-1} \qquad \text{as } \Lambda \to 0\,, \tag{5.49}$$

and as stated before $\hat{C}_2 = \hat{C}_0^2$. For example, if the effective range vanishes, $r_0 = 0$, the two-body pole energy obeys the universal relation $\sqrt{2\mu E_2} = 1/|a|$, and we find that for negative a the coupling constant $\hat{C}_0 \to -1/2$, while for positive a the coupling constant diverges, $\hat{C}_0 \to -\infty$. Only for the case of an infinitely negative effective range, $r_0 = -\infty$, will the coupling constants vanish as the cutoff approaches zero. However, the vanishing cutoff does not fulfill the requirement that Λ be larger than the momentum scale of the two-body system. In this case, the regulation scheme affects the details of the potential in the low-energy scale, and can not be used to reliably reproduce the physics of the desired system.

At the other end of the trajectory, the cutoff is much larger than the momentum scale of the two-body system, and we see that all trajectories approach the same limit.

Both $\hat{C}_0$ and $\hat{C}_2$ flow toward fixed-points as the cutoff is increased:

$$\hat{C}_0(\Lambda) \to -1\,, \qquad \text{and } \hat{C}_2(\Lambda) \to +1 \qquad \text{as } \Lambda \to \infty\,. \tag{5.50}$$

According to Eq. (5.28), this fixed-point corresponds to the two-body problem in the *resonant limit*, $a \to \pm\infty$. Since the scaling limit, in which the natural low-energy length scale $\ell \to 0$, was implicitly taken in the effective potential through the use of only two-body contact interactions, the $\Lambda \to \infty$ fixed-points correspond to the special case of taking the resonant and scaling limits simultaneously. Although an arbitrary system has a finite fixed value of a, the flow of all trajectories toward the fixed-points suggests that as the energy scale increases to values larger and larger compared to $1/a^2$, the system behaves more and more like the resonant limit. In an actual physical system, there is a natural cutoff corresponding to the natural low-energy length scale $\Lambda \sim 1/\ell$, beyond which two-body contact interactions are not sufficient to describe the physics. The behavior of the system will become more complicated for $\Lambda > 1/\ell$, and will no longer flow toward the fixed-points. This value for Λ is the momentum, or corresponding energy, at which our effective theory breaks down and a more fundamental theory would be needed.

The properties of the renormalization group flow in the large cutoff (vanishing $\tilde{x}_0$) limit can also be seen through the analysis of the *differential renormalization group equations*. Differentiating both sides of Eqs. (5.47, 5.48) with respect to Λ (after assuming $\exp(\tilde{x}_0^2)\mathrm{erfc}(\tilde{x}_0) \to 1$), one can derive the RG equations [Kap98]:

$$\Lambda\frac{d}{d\Lambda}\hat{C}_0 = \hat{C}_0(1+\hat{C}_0)\,, \qquad \Lambda\frac{d}{d\Lambda}\hat{C}_2 = 2\hat{C}_2\left(1 \pm \sqrt{\hat{C}_2}\right)\,, \tag{5.51}$$

where we must first resolve the problem of the $\pm\sqrt{\hat{C}_2}$. As has been already observed, there is a fixed-point in the $\hat{C}_2$ trajectory of $\hat{C}_2 = 1$ as $\Lambda \to \infty$, Eq. (5.50). Therefore, in order for the RG equation to reproduce this fixed-point, we must choose $-\sqrt{\hat{C}_2}$. Then the two RG equations produce the corresponding fixed-points already described at $\hat{C}_0 = -1$, and $\hat{C}_2 = +1$, as well as the spurious fixed-points $\hat{C}_0 = \hat{C}_2 = 0$ which appeared for $\Lambda \to 0$ when one first assumes $\tilde{x}_0 = 0$.

At the two fixed-points, the two-body system displays a scale invariance. Generally, the mapping of one theory onto another theory with a different scattering length a can be done through a continuous scaling symmetry

$$a \to \lambda a, \qquad E \to \lambda^{-2}E\,, \tag{5.52}$$

where λ is an arbitrary positive real number. For our case, at the fixed-point $a = \pm\infty$, the continuous scaling symmetry obviously does not change the value of a, so it maps the theory onto itself, a scaling invariance. The scale invariance at this fixed-point actually is part of the two-body system's invariance under a larger group of conformal symmetry transformations [Me00].

5.2 The NLO Faddeev Equations

The two-body NLO T-matrix derived in Sec. 5.1.1 can be used in the kernel of the Faddeev integral equations found in Sec. 3.3. In the following subsection we derive the Faddeev equations for the $2n$ halo nucleus problem using the Gaussian regulator functions. However, in order to properly renormalize the three-body system including effective range corrections, it is necessary to include a three-body force term in the Faddeev equations. It is most convenient to include the three-body term while working with a strong cutoff regularization, and the details of switching to this regularization scheme and including the three-body force term are discussed in Sec. 5.2.2.

5.2.1 The Faddeev Equations with Gaussian Regulators

We now wish to derive a form of the coupled Faddeev equations suitable for solving the bound $2n$ halo nucleus problem. However, for S-waves, this has already been done in Sec. 4.2. The resulting coupled integral equations are exactly those found in Eqs. (4.45, 4.46):

$$\begin{aligned} F_n(q) &= \frac{1}{2}\int_0^\infty dq' q'^2 \int_{-1}^{1} dx \Big[g\left(\tilde{\pi}(q,q')\right) g\left(\tilde{\pi}(q',q)\right) \\ &\quad \times G_0^n\left(\tilde{\pi}(q',q),q';B_3\right) t_n(q';B_3) F_n(q') \\ &\quad + g\left(\tilde{\pi}_1(q,q')\right) g\left(\tilde{\pi}_2(q,q')\right) \\ &\quad \times G_0^c\left(\tilde{\pi}_2(q,q'),q';B_3\right) t_c(q';B_3) F_c(q') \Big], \end{aligned} \tag{5.53}$$

$$\begin{aligned} F_c(q) &= \int_0^\infty dq' q'^2 \int_{-1}^{1} dx \Big[g\left(\tilde{\pi}_1(q',q)\right) g\left(\tilde{\pi}_2(q',q)\right) \\ &\quad \times G_0^n\left(\tilde{\pi}_1(q',q),q';B_3\right) t_n(q';B_3) F_n(q') \Big], \end{aligned} \tag{5.54}$$

where the propagators $G_0^i(p,q;B_3)$, with $i = n, c$, are defined in Eqs. (4.17, 4.18), the Gaussian regulator function $g(p)$ in Eq. (4.3), and the shifted momenta $\tilde{\pi}, \tilde{\pi}_1, \tilde{\pi}_2$ in Eqs. (4.37, 4.40, 4.41). The functions $F_i(q)$ are known as the Faddeev spectator functions, and their relation to the Faddeev components of the wave function is found in Eq. (4.44). The three-body binding energies are given by the values of B_3 for which the coupled integral equations have a nontrivial solution. However, the coupled equations are most easily solved by discretizing the variables q and q', and solving the resulting matrix equation (see Eq. (4.47)):

$$\begin{bmatrix} F_n \\ F_c \end{bmatrix} = \begin{bmatrix} K_{nn} & K_{nc} \\ K_{cn} & 0 \end{bmatrix} \begin{bmatrix} F_n \\ F_c \end{bmatrix}, \tag{5.55}$$

with kernels K_{ij} taken from the coupled Faddeev equations above. Then, the binding energies are given by the values of B_3 for which the kernel matrix has an eigenvalue of 1.

The only difference from the LO result is that the functions $t_i(q';B_3)$ now describe the effects of the NLO two-body interactions (see Eq. (5.32)):

$$\begin{aligned} t_n(q';B_3) &= \frac{1}{\pi}\frac{A+1}{A}\left(1+\tilde{E}_n(q';B_3)\frac{\frac{r_{nc}}{2}\exp(\tilde{x}_{nc}^2)\mathrm{erfc}(\tilde{x}_{nc})}{\left(\frac{\Lambda}{2}\right)\sqrt{\frac{2}{\pi}}-\frac{1}{a_{nc}}\exp(\tilde{x}_{nc}^2)\mathrm{erfc}(\tilde{x}_{nc})}\right) \\ &\times\left[-\frac{1}{a_{nc}}\exp(\tilde{x}_{nc}^2)\mathrm{erfc}(\tilde{x}_{nc})+\sqrt{\tilde{E}_n(q';B_3)}\exp(\tilde{x}_n^2)\mathrm{erfc}(\tilde{x}_n)\right. \\ &-\frac{r_{nc}}{2}\exp(\tilde{x}_{nc}^2)\mathrm{erfc}(\tilde{x}_{nc})\tilde{E}_n(q';B_3) \\ &\left.\times\left(\frac{\left(\frac{\Lambda}{2}\right)\sqrt{\frac{2}{\pi}}-\sqrt{\tilde{E}_n(q';B_3)}\exp(\tilde{x}_n^2)\mathrm{erfc}(\tilde{x}_n)}{\left(\frac{\Lambda}{2}\right)\sqrt{\frac{2}{\pi}}-\frac{1}{a_{nc}}\exp(\tilde{x}_{nc}^2)\mathrm{erfc}(\tilde{x}_{nc})}\right)\right]^{-1}, \end{aligned} \tag{5.56}$$

$$\begin{aligned} t_c(q';B_3) &= \frac{2}{\pi}\left(1+\tilde{E}_c(q';B_3)\frac{\frac{r_{nn}}{2}\exp(\tilde{x}_{nn}^2)\mathrm{erfc}(\tilde{x}_{nn})}{\left(\frac{\Lambda}{2}\right)\sqrt{\frac{2}{\pi}}-\frac{1}{a_{nn}}\exp(\tilde{x}_{nn}^2)\mathrm{erfc}(\tilde{x}_{nn})}\right) \\ &\times\left[-\frac{1}{a_{nn}}\exp(\tilde{x}_{nn}^2)\mathrm{erfc}(\tilde{x}_{nn})+\sqrt{\tilde{E}_c(q';B_3)}\exp(\tilde{x}_c^2)\mathrm{erfc}(\tilde{x}_c)\right. \\ &-\frac{r_{nn}}{2}\exp(\tilde{x}_{nn}^2)\mathrm{erfc}(\tilde{x}_{nn})\tilde{E}_c(q';B_3) \\ &\left.\times\left(\frac{\left(\frac{\Lambda}{2}\right)\sqrt{\frac{2}{\pi}}-\sqrt{\tilde{E}_c(q';B_3)}\exp(\tilde{x}_c^2)\mathrm{erfc}(\tilde{x}_c)}{\left(\frac{\Lambda}{2}\right)\sqrt{\frac{2}{\pi}}-\frac{1}{a_{nn}}\exp(\tilde{x}_{nn}^2)\mathrm{erfc}(\tilde{x}_{nn})}\right)\right]^{-1}, \end{aligned} \tag{5.57}$$

where a_{nn}, r_{nn}, and a_{nc}, r_{nc} are the n-n and n-c scattering lengths and effective ranges, respectively. Also, for brevity we have defined the variables $\tilde{x}_i$ and $\tilde{x}_{ni}$ where $i=n,c$ (see Sec. 5.1.1):

$$\tilde{x}_i \equiv \frac{\sqrt{2\tilde{E}_i(q';B_3)}}{\Lambda}, \tag{5.58}$$

$$\tilde{x}_{ni} \equiv \frac{\sqrt{2(2\mu E_{ni})}}{\Lambda}, \tag{5.59}$$

where E_{ni} is the two-body bound(virtual) state energy calculated from the pole of the two-body NLO T-matrix as prescribed in Eq. (5.37), and $\tilde{E}_i(q';B_3)$ is the two-body subsystem energy function defined in Eqs. (4.25, 4.26).

5.2.2 The Faddeev Equations with a Strong Cutoff

In calculating three-body observables to LO, it was not necessary to include a three-body force term, as the limit cycle behavior of the three-body force allows one to tune the cutoff to mimic the effects of a three-body force term (see Sec. 4.3.1). However, to NLO, the renormalization of the three-body problem is not as simple, and a proper renormalization can only be guaranteed by the inclusion of an explicit three-body force term [Ham06]. Unfortunately, the inclusion of a three-body force is fairly complicated when using Gaussian regulator functions [Pl04a]. Therefore, we now switch to a more convenient choice of regularization, a strong momentum cutoff. In this regularization scheme, the interaction potential, Eq. (5.1), is set to zero for momenta greater than the cutoff parameter Λ. In this case, the regulator functions $g(p)$ are not needed and can be ignored.

The derivation of the two-body interaction T-matrix using a strong cutoff is analogous to that done in Sec. 5.1.1. One would simply eliminate all exponential functions arising from the Gaussian regulator functions $g(p)$ and instead set the upper limit of all phase space integrals to Λ. One finds that the difference in the two regularization schemes arises from the results of the A_i integrals defined in Eq. (5.9), and discussed in detail in App. A. Solving the A_i integrals using a strong cutoff, we find that to switch from a Gaussian regulator to a strong cutoff one must simply replace the forms of the regulator factor and the Λ dependent terms in all equations using the following prescription:

Gaussian Regulator	Strong Cutoff
$\exp\left(\tilde{x}^2\right)\operatorname{erfc}\left(\tilde{x}\right)$	$\frac{2}{\pi}\arctan\left(\frac{\sqrt{2}}{\tilde{x}}\right)$
$(n-2)!!\left(\frac{\Lambda}{2}\right)^n\sqrt{\frac{2}{\pi}}$	$\frac{2}{\pi}\frac{1}{n}\Lambda^n.$

Here we see that in both cases the regulator factors quickly approach 1 as $\tilde{x} \to 0$.

Therefore, the coupled Faddeev integral equations using a strong cutoff will be similar to those found in Eqs. (5.53, 5.54) (see previous subsection), but with an upper limit of Λ on the momentum integrals, the elimination of the $g(\tilde{\pi})$ regulator functions, and the $t_i(q'; B_3)$ functions, Eq. (5.56, 5.57), having changed according to the above prescription. With the elimination of the $g(\tilde{\pi})$ functions, the only x dependence appears in the propagators $G_0^i(\tilde{\pi}, q'; B_3)$ in such a form that the dx integration can be performed analytically. The resulting coupled integral equations are:

$$\begin{aligned} F_n(q) &= \frac{1}{2}\int_0^\Lambda dq' q'^2 \Big[\tilde{G}_n(q, q'; B_3)\; t_n(q'; B_3)\; F_n(q') \\ &\quad + \tilde{G}_c(q, q'; B_3)\; t_c(q'; B_3)\; F_c(q') \Big], \end{aligned} \tag{5.60}$$

$$F_c(q) \;=\; \int_0^\Lambda dq' q'^2 \Big[\tilde{G}_c(q',q;B_3)\; t_n(q';B_3)\; F_n(q') \Big], \tag{5.61}$$

where

$$\tilde{G}_n(q,q';B_3) \;=\; \frac{A}{qq'} \ln \left(\frac{\frac{2A}{A+1}B_3 + q^2 + q'^2 + \frac{2}{A+1}qq'}{\frac{2A}{A+1}B_3 + q^2 + q'^2 - \frac{2}{A+1}qq'} \right), \tag{5.62}$$

$$\tilde{G}_c(q,q';B_3) \;=\; \frac{1}{qq'} \ln \left(\frac{B_3 + q^2 + \frac{A+1}{2A}q'^2 + qq'}{B_3 + q^2 + \frac{A+1}{2A}q'^2 - qq'} \right). \tag{5.63}$$

We can now straightforwardly add a three-body force term to the above integral equations by noticing that for the case of three identical particles in the LO limit, Eqs. (5.60, 5.61) reproduce the well known three-boson bound state equation obtained in Ref. [Br06b]. This study derived the three-body force term for identical bosons by using an EFT including a three-body contact interaction. However, this three-body interaction was simplified using the *diatom field* trick, in which the EFT was formulated with an explicit diatom field d, a local operator that annihilates two atoms at a point. The Lagrangian first derived by Bedaque, Hammer, and van Kolck [Bed99] has the following form:

$$\mathcal{L}_{\rm BHvK} \;=\; \psi^\dagger \left(i\frac{\partial}{\partial t} + \frac{1}{2}\nabla^2 \right) \psi + \frac{g_2}{4} d^\dagger d - \frac{g_2}{4} \left(d^\dagger \psi^2 + {\psi^\dagger}^2 d \right) - \frac{g_3}{36} d^\dagger d \psi^\dagger \psi \,, \tag{5.64}$$

where ψ is the particle field operator, g_2 is the leading order two-body coupling constant, and g_3 the three-body coupling constant. This Lagrangian can then be used to derive the integral equation for the three-boson amplitude, diagrammatically shown in Fig. 5.3, where the single and double lines represent the particle and diatom field, respectively, and the thick solid line represents the full diatom propagator (for details see Ref. [Br06b]). The homogeneous terms which appear in the bound state integral equation arise from the two diagrams in the second line of Fig. 5.3, where the first of these diagrams corresponds to the term dependent only on the two-body contact interaction, analogous to those already found in Eqs. (5.60, 5.61).

The last diagram in the integral equation then represents the missing three-body term. The dependence on the three-body coupling constant g_3 is found only in a factor proportional to the ratio g_3/g_2^2, and it is most convenient to define a dimensionless three-body function $H(\Lambda)$[1]:

$$H(\Lambda) = -2\frac{g_3}{9g_2^2}\Lambda^2. \tag{5.65}$$

[1]Note, the definition of $H(\Lambda)$ in the present work differs from that found in [Br06b] by a factor of 1/2.

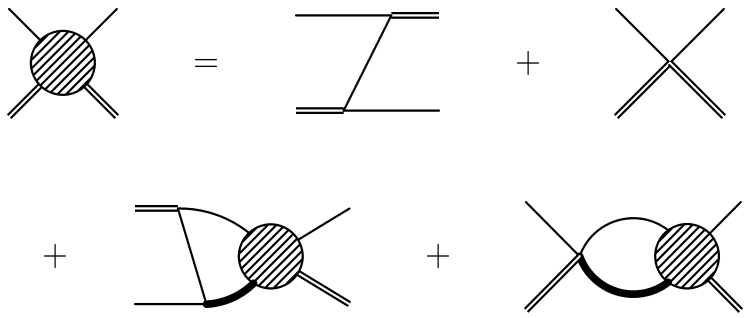

Figure 5.3: The integral equation for the three-body amplitude. Figure used with permission from Ref. [Br06b].

We, therefore, include a three-body force term analogously to our coupled integral equations for the $2n$ halo nucleus system:

$$F_n(q) = \frac{1}{2}\int_0^\Lambda dq' q'^2 \Bigg[\left(\tilde{G}_n(q,q';B_3) + \frac{H(\Lambda)}{\Lambda^2} \right) \; t_n(q';B_3) \; F_n(q') + \left(\tilde{G}_c(q,q';B_3) + \frac{H(\Lambda)}{\Lambda^2} \right) \; t_c(q';B_3) \; F_c(q') \Bigg], \tag{5.66}$$

$$F_c(q) = \int_0^\Lambda dq' q'^2 \Bigg[\left(\tilde{G}_c(q',q;B_3) + \frac{H(\Lambda)}{\Lambda^2} \right) \; t_n(q';B_3) \; F_n(q') \Bigg]. \tag{5.67}$$

The three-body binding energies are given by the values of B_3 for which the coupled integral equations have a nontrivial solution. The three-body system is determined by the n-c and n-n scattering lengths and effective ranges. However, in order to correctly renormalize the theory, one three-body parameter is required. For a fixed value of Λ, the three-body term $H(\Lambda)$ can be tuned to reproduce a given three-body observable and then other low-energy observables can be predicted using the same $H(\Lambda)$.

We are also interested in calculating other low-energy physical properties of three-body halo nuclei, specifically the matter density form factors and the mean square radii. The information needed to calculate such quantities is held in the wave functions of the known bound states. The full wave function of the bound $2n$ halo nucleus can be reconstructed from the solutions for the spectator functions F_n and F_c found from our coupled integral equations, Eqs. (5.66, 5.67). However, the form of the wave function, ${}_i\langle pq|\Psi\rangle \equiv \Psi_i(p,q)$, depends on the choice of two-body subsystem and corresponding spectator particle, where the index $i = n, c$ labels the chosen spectator particle. Recall that in the wave functions, the p Jacobi momentum describes the relative momentum between the two particles in the chosen two-body subsystem, while q describes the momentum of the spectator particle relative to the center of mass

of the two-body subsystem. The proper reconstruction of the full wave equations was derived in Sec. 4.4.1 for the case of Gaussian regulator functions without the presence of a three-body term. We now must derive the analogous relations for the strong cutoff regularization scheme, along with a three-body force term.

The make-up of the full wave function in terms of its Faddeev components ψ_i does not depend on the choice of regularization scheme, and for $2n$ halo nuclei is derived from Eq. (3.13). We, therefore, use the same relations found in Sec. 4.4.1 (see Eqs. (4.56, 4.57)):

$$\Psi_n(p,q) = \psi_n(p,q) + \frac{1}{2}\int_{-1}^{1} dx\ \left[\psi_n(\tilde{\pi}_{nn},\tilde{\pi}'_{nn}) + \psi_c(\tilde{\pi}_{nc},\tilde{\pi}'_{nc})\right], \tag{5.68}$$

$$\Psi_c(p,q) = \int_{-1}^{1} dx\ \psi_n(\tilde{\pi}_{cn},\tilde{\pi}'_{cn}) + \psi_c(p,q), \tag{5.69}$$

where the definitions of the various shifted momenta $\tilde{\pi}_{ij}$ are found in Sec. 4.4.1. The difference between using Gaussian regulator functions and the strong cutoff now appears in the definition of the Faddeev components ψ_i in terms of the spectator functions F_i, which for Gaussian regulator functions is found in Eq. (4.44). We can switch from the Gaussian regulator to a strong cutoff in the same way as before: dropping the Gaussian regulator function $g(p)$ and changing the $t_i(q;B_3)$ functions according to the prescription detailed at the beginning of this subsection.

However, we must now include the three-body term in order to properly reconstruct the wave function from the spectator functions. We see that the inclusion of the three-body force term $H(\Lambda)$ into the coupled integral equations, Eqs. (5.66, 5.67), occurs as a function added to the propagator factor $\tilde{G}_i$ such that, in operator notation, the operator corresponding to the propagator $G \to G+H$. Therefore, we include the three-body term in the same way to the definition of the Faddeev components in terms of the spectator functions, and find:

$$\psi_i(p,q) = \left(G_0^i(p,q;B_3) + H(\Lambda)/\Lambda^2\right) t_i(q;B_3) F_i(q), \tag{5.70}$$

where the propagators $G_0^i(p,q;B_3)$ for $i = n,c$ are defined in Eqs. (4.17, 4.18). Substituting this relation into Eqs. (5.68, 5.69), we again find that:

$$G_0^n(\tilde{\pi}_{nn},\tilde{\pi}'_{nn};B_3) = G_0^n(p,q;B_3), \tag{5.71}$$

$$G_0^c(\tilde{\pi}_{nc},\tilde{\pi}'_{nc};B_3) = G_0^n(p,q;B_3), \tag{5.72}$$

$$G_0^n(\tilde{\pi}_{cn},\tilde{\pi}'_{cn};B_3) = G_0^c(p,q;B_3). \tag{5.73}$$

Therefore, to reconstruct the full wave functions in the S-wave with either a neutron

or core spectator from the spectator functions we find:

$$\Psi_n(p,q) = \left(G_0^n(p,q;B_3) + \frac{H(\Lambda)}{\Lambda^2}\right)\Bigg[t_n(q;B_3)F_n(q) + \frac{1}{2}\int_{-1}^{1} dx\ t_n(\tilde{\pi}'_{nn};B_3)F_n(\tilde{\pi}'_{nn}) + t_c(\tilde{\pi}'_{nc};B_3)F_c(\tilde{\pi}'_{nc})\Bigg], \quad (5.74)$$

$$\Psi_c(p,q) = \left(G_0^c(p,q;B_3) + \frac{H(\Lambda)}{\Lambda^2}\right)\Bigg[t_c(q;B_3)F_c(q) + \int_{-1}^{1} dx\ t_n(\tilde{\pi}'_{cn};B_3)F_n(\tilde{\pi}'_{cn})\Bigg]. \quad (5.75)$$

The three-body wave functions can now be used to calculate other low-energy properties of the three-body bound state. With the Jacobi momentum states it is straightforward to calculate the Fourier transform of the one- and two-body matter densities with respect to the momentum transfer squared. These are defined as the one- and two-body matter density form factors $\mathcal{F}_i(k^2)$ and $\mathcal{F}_{ni}(k^2)$, respectively, where $i = n, c$. The derivation of the form factors from the three-body S-wave wave functions was done in Sec. 4.4.2, and we refer the reader to that subsection for more details. The result for the one-body form factors is:

$$\mathcal{F}_i(k^2) = \int dp\ p^2 \int dq\ q^2 \int_{-1}^{1} dx\ \Psi_i(p,q)\Psi_i(p,\sqrt{q^2+k^2-2qkx}), \quad (5.76)$$

and for the two-body form factors:

$$\mathcal{F}_{nc}(k^2) = \int dp\ p^2 \int dq\ q^2 \int_{-1}^{1} dx\ \Psi_n(p,q)\Psi_n(\sqrt{p^2+k^2-2pkx},q), \quad (5.77)$$

and

$$\mathcal{F}_{nn}(k^2) = \int dp\ p^2 \int dq\ q^2 \int_{-1}^{1} dx\ \Psi_c(p,q)\Psi_c(\sqrt{p^2+k^2-2pkx},q). \quad (5.78)$$

The mean square radii for our three-body bound states are calculated from the matter density form factors in the low momentum transfer region, as described in Sec. 4.4.3.

With the formalism now in place, we proceed in finding NLO corrections to the bound state spectrum and the mean square radii, first in the bound three-boson system (Sec. 5.3), and then in $2n$ halo nuclei systems (Sec. 5.4).

5.3 Effective Range Corrections to Three-Boson Bound States

As previously mentioned, the coupled Faddeev integral equations derived for $2n$ halo nuclei, Eqs. (5.66, 5.67), are a generalization of the three-boson equation. To reduce

to the NLO three-boson bound state equation we simply set the core mass equal to the nucleon mass, $A = 1$, along with setting the n-c scattering length and effective range equal to the n-n values: $a_{nc} = a_{nn} = a$, $r_{nc} = r_{nn} = r_0$. When this is done, Eq. (5.66) becomes identical to Eq. (5.67) and instead of a coupled set of integral equations, we now must solve just one integral equation. We find the bound state spectrum of the three-boson system by finding the energies B_3 for which this integral equation has a nontrivial solution, or in practice by discretizing the integral and finding the energies which give an eigenvalue of 1 for the kernel matrix. In using the NLO T-matrix in the kernel of the Faddeev equations, we explore the effective range corrections to the three-boson bound state spectrum, as well as universality in these corrections in Sec. 5.3.1. In the following subsection, Sec. 5.3.2, we look at the NLO effects on the geometry of the Efimov states, specifically the mean square separation of the particles in the two-body (dimer) subsystem as well as the mean square distance of the spectator particle from the three-body center of mass.

5.3.1 Range Corrections to the Efimov Effect

We find the spectrum of three-boson bound states for different scattering lengths in the region where the scattering length is much larger than the range of the interaction. The spectrum of bound state energies $B_3^{(n)}$ as a function of the two-body pole energy E_2, which is related to the scattering length a and effective range r_0 according to Eq. (5.37), is shown in Fig. 5.4, where negative values on the E_2-axis correspond to negative scattering lengths a. We have scaled the energies by a power of 1/8 so that a greater range of the bound state spectrum can be displayed, as the discrete scaling factor λ_0 is reduced from 22.7 to $22.7^{1/8} = 1.48$. Due to the discrete scale invariance of the system, all quantities are found in units of the appropriate power of an arbitrarily chosen momentum scale κ_*. As mentioned before, we require one three-body parameter in order to renormalize the three-body system. We have renormalized the binding energies by tuning the three-body term $H(\Lambda)$, for a fixed Λ, such that the state with index $n_* = 1$ has a binding energy of $B_3^{(1)} = 10.0\kappa_*^2$ in the resonant limit $E_2 = 0$. We use units such that the boson mass $m = 1$ as well as $\hbar = c = 1$. The leading order results are represented by the solid black lines, and agree with those presented in Ref. [Br06b].

The NLO results are renormalized in the same way, finding the shifted value of $H(\Lambda)$, for the same fixed Λ, such that $B_3^{(1)} = 10.0\kappa_*^2$ in the resonant limit $E_2 = 0$. Due to the Wigner bound, which limits the maximum positive effective range for a chosen finite Λ, or vice versa (see Sec. 5.1.3), some care must be taken in choosing Λ. For all results in Fig. 5.4, we have chosen $\Lambda = 200.0\kappa_*$, which constrains the effective range at the resonant limit to $r_0 \leq 0.019\kappa_*^{-1}$. The constraint on r_0 does not change dramatically for finite values of a as long as $a \gg r_0$. As a representative example of NLO corrections to the Efimov plot, we show the results for $r_0 = 0.01\kappa_*^{-1}$ and $r_0 = -0.01\kappa_*^{-1}$, represented by the dashed red lines and the dotted-dashed blue lines in Fig. 5.4, respectively.

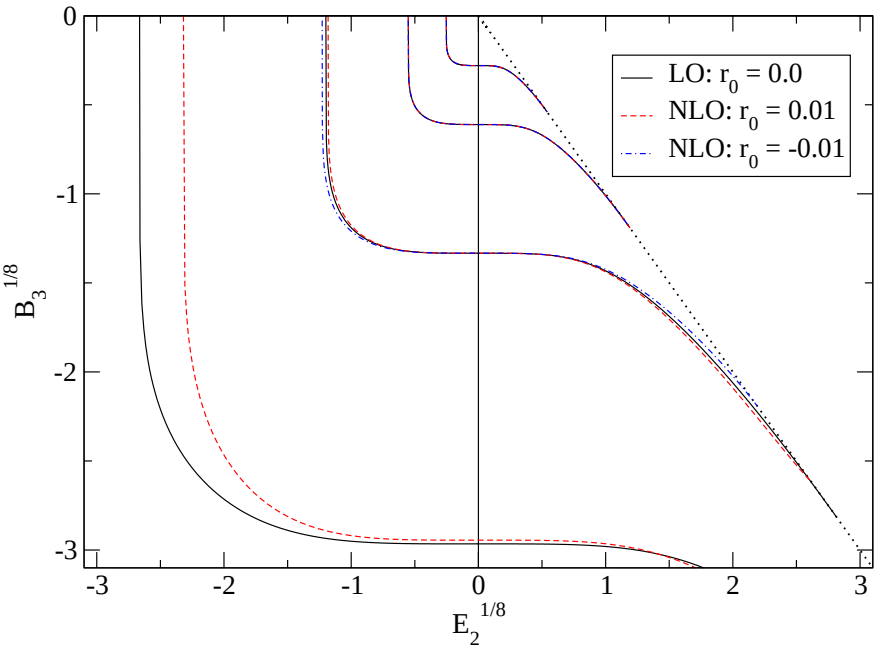

Figure 5.4: The spectrum of three-boson bound states with short-range interactions, as a function of the two-body pole energy E_2. Negative values on the E_2-axis correspond to negative scattering lengths a. All quantities in units of the appropriate power of an arbitrarily chosen momentum scale κ_* (see text for details). Binding energies B_3 and two-body pole energy E_2 are both scaled by a power of $1/8$ so that a greater range of bound states can be displayed. Black solid lines: LO case $r_0\kappa_* = 0.0$, red dashed lines: NLO case with $r_0\kappa_* = 0.01$, blue dotted-dashed lines: NLO case with $r_0\kappa_* = -0.01$, dotted line: atom-dimer breakup threshold.

We see that the shift in the binding energies $\Delta B_3^{(n)}$ caused by effective range corrections is only recognizable in the deeper Efimov states, although there are similar shifts in the shallower excited states. Also, the shift in the resonant limit vanishes (up to corrections $\sim 1/\Lambda$) for all states within the range of validity of our effective theory. The binding energy of the deepest state $B_3^{(0)}(E_2 = 0)$ is near the order of magnitude of the cutoff Λ and details of the regularization scheme become important for this state. It is for this reason that the NLO result with $r_0 = -0.01\kappa_*^{-1}$ is not displayed for this state. These calculations agree with the analytically derived result of Platter, Ji and Phillips in Ref. [Pl08], that in the resonant limit, if the shift $\Delta B_3^{(n_*)}$ is forced by the renormalization procedure to equal zero, the shift for all states $\Delta B_3^{(n)} = 0$ for all n. This conclusion holds for the limit $\Lambda \to \infty$, where the regularization and renormalization of the theory respect discrete scale invariance. For a finite Λ, there will be violations of discrete scale invariance, which result in $1/\Lambda$-suppressed corrections to $\Delta B_3^{(n)}$ [Pl08]. However, as long as Λ is kept large compared to the momentum scale of the system, these corrections will be of higher order than

considered here.

For small values of the effective range, we assume that the effective range corrections to the the binding energies can be treated perturbatively, with the first order correction linear in r_0. This leads to the universal function [Pl08]:

$$B_3^{(n)} = \kappa_*^2 \left[F^{(n)}\left(\frac{\sqrt{E_2}}{\kappa_*}\right) + r_0\kappa_* G^{(n)}\left(\frac{\sqrt{E_2}}{\kappa_*}\right) + \ldots \right], \tag{5.79}$$

where κ_* is an arbitrarily chosen momentum scale which can be set through renormalization. For our calculations, we continue to renormalize the three-body system such that the state $n_* = 1$ has $B_3^{(1)}(E_2 = 0) = 10.0\kappa_*^2$. The function $F^{(n)}$ gives the LO binding energy of the nth state at an arbitrary E_2, and can be found in Ref. [Br06b]. The function $G^{(n)}$ then gives the NLO corrections to the binding energy of the nth state which are linear in r_0. In Ref. [Pl08], it was hypothesized that, due to discrete scale invariance in the LO case, there should be an approximate discrete scaling factor which would relate $G^{(n)}$ to $G^{(n_*)}$. The analysis of linear range corrections in the resonant limit leads to the assumption of a κ^3 scaling between the first order corrections, which leads to the hypothesis for arbitrary E_2 [Pl08]:

$$G^{(n)}\left(\frac{\sqrt{E_2}}{\kappa_*}\right) = \theta^{(n)}\left(\frac{\sqrt{E_2}}{\kappa_*}\right) \lambda_0^{3(n_*-n)} G^{(n_*)}\left(\frac{\sqrt{E_2}}{\kappa_*}\lambda_0^{n_*-n}\right), \tag{5.80}$$

where λ_0 is the universal scaling factor defined by: $\lambda_0 = \exp(\pi/s_0)$, and $s_0 = 1.00624$ is a universal number [Br06b]. The function $\theta^{(n)}$ accounts for the effects that modify the scaling for finite E_2 and obeys the constraints:

$$\theta^{(n_*)}(x) = 1 \text{ for all } x, \tag{5.81}$$

$$\theta^{(n)}(0) = 1 \text{ for all } n. \tag{5.82}$$

It is assumed that $\theta^{(n)} \sim 1$ for all other E_2.

Computing the function $G^{(n)}(\sqrt{E_2/\kappa_*})$ involves finding the slope of a curve in the $B_3^{(n)}$ vs. r_0 plane for a desired E_2. In practice, we fit a straight line to $B_3^{(n)}$ vs. r_0 data, calculated at a fixed E_2 for effective ranges $|r_0| \leq 0.001\kappa_*^{-1}$. This allowed us to increase the cutoff parameter to a value of $\Lambda = 1000\kappa_*$, which corresponds to a Wigner bound of $r_0 \leq 0.0038\kappa_*^{-1}$. In order to find the slope in the $r_0 \to 0$ limit, the fit was then repeated using a smaller maximum $|r_0|$, and convergence was found for $|r_0| \leq 0.0001\kappa_*^{-1}$ for most bound states. This procedure was repeated for a range of E_2 values, or corresponding scattering lengths a, which span the entire existence of the nth bound state, for $n = 0, 1, 2$ and 3. Results of this procedure are shown in Figs. 5.5, 5.6, where we have now normalized the arbitrarily chosen κ_* scale such that in the resonant limit $B_3^{(1)}(E_2 = 0) = \kappa_*^2$. These results agree in large part with the results found in Ref. [Pl08], however our technique allows us to obtain sufficiently accurate results for multiple bound states in the negative scattering length region.

Our results for negative scattering length are shown in Fig. 5.5, where the solid black line represents the $n_* = 1$ state, to which we have renormalized our three-body

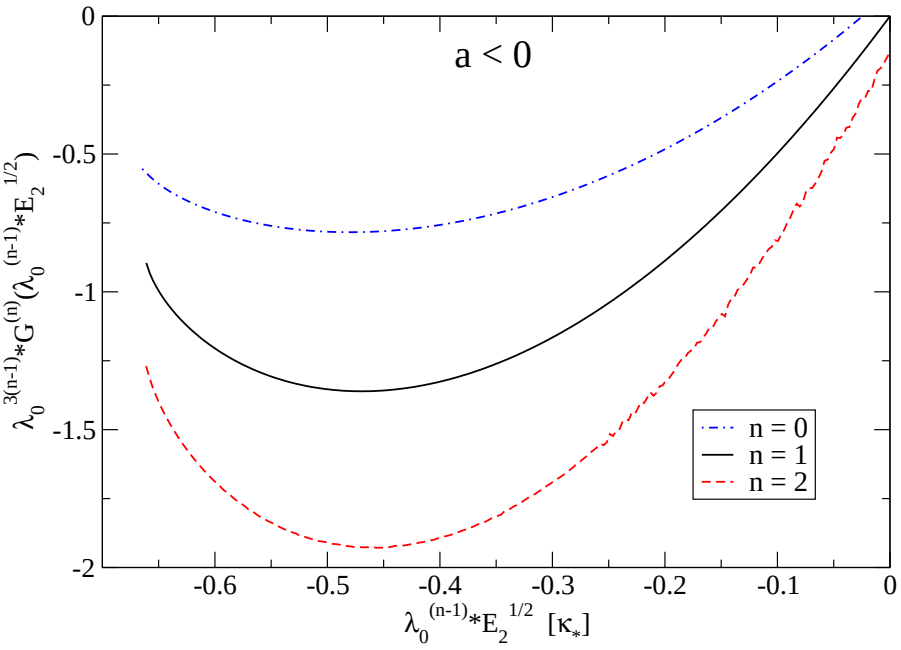

Figure 5.5: The function $G^{(n)}$ for negative scattering lengths, for $n = 0, 1, 2$. Solid black lines represent the results for the $n_* = 1$ state, the state to which our three-body system is renormalized. Results for other states $n \neq 1$ are scaled according to Eq. (5.80); red dashed lines: $n = 2$, blue dot-dashed line: $n = 0$.

system. The results for $n = 2$ (dashed red line) and $n = 0$ (dotted-dashed blue line) have been scaled according to Eq. (5.80). We see that scaling the two-body pole energy $\lambda_0^{n-1}\sqrt{E_2}$ does indeed bring all states onto the same horizontal scale. For all states, the functions $G^{(n)}$ vanish at the critical value of the scattering length, or corresponding $\sqrt{E_2}$, in the $r_0 \to 0$ limit, where the bound system breaks up into three bosons. In the LO limit, this critical scattering length is related to the binding energy in the resonant limit by a universal relation [Br06b]:

$$\sqrt{E_{2-}^{(n)}} = 1/a_-^{(n)} = -0.6633\sqrt{B_3^{(n)}(E_2 = 0)}. \tag{5.83}$$

Also, the minima in the rescaled $G^{(n)}$ functions are all at approximately the same position, $\sqrt{E_2} \approx -0.47\kappa_*$, however with the trend that the minimum position decreases slightly in magnitude in going from deeper to shallower states. On the vertical scale, the scaling assumed in Eq. (5.80), $\lambda_0^{3(n-1)}G^{(n)}$, does allow the results for all Efimov states to be plotted on the same scale. However, there is an obvious deviation from a pure λ_0^3 scaling between neighboring states. Here there is also a recognizable trend, with shallower states having an increasingly larger magnitude of $|G^{(n)}|$ after rescaling. This deviation in discrete scaling is encoded in the $\theta^{(n)}$ function, and an investigation into the form of this function will be done in a future work.

We also note that only $G^{(1)}$ goes to zero in the resonant limit, although it was

stated before, that the NLO effective range corrections of all states should be zero as long as the corrections for the n_* state are forced to be zero by renormalization. This is due to both the higher order corrections which appear when using a finite Λ, as well as the numerical uncertainty in our calculations. The binding energies for the $n = 0$ state for scattering lengths near the resonant limit approach the order of magnitude of Λ and, therefore, the details of the regulator scheme become important. The results for $G^{(2)}$, it should be recalled, are scaled by a factor $\lambda_0^3 = 11688.2$, such that even a small deviation from zero at the resonant limit becomes magnified by four orders of magnitude. For practical purposes, the deviation from $G^{(n)} = 0.0$ at $\sqrt{E_2} = 0.0$ for the results corresponding to $n \neq n_*$, can be used as an estimation of the relative uncertainty in these curves.

The results for $n = 1$ for negative scattering length agree in large part to those found by Platter, Ji and Phillips in Ref. [Pl08], especially on the horizontal scale, where the position of the minimum is almost exactly the same. However, the magnitude of $|G^{(1)}|$ in our study is larger than that found in [Pl08] by a factor of ≈ 1.6. This discrepancy could be due to numerical inaccuracy inherent in extracting such small values of the function $G^{(n)}$, or could be attributed to higher order effects stemming from the use of a finite Λ.

For future studies, it will be important to improve the numerical accuracy of our calculations. The fluctuations seen in the $n = 2$ results in both Figs. 5.5, 5.6 are due to limited numerical accuracy both in calculating the binding energies of these states, and then performing a straight line fit to this data. While these fluctuations are originally of an acceptable order of magnitude ($\approx 10^{-5}$), one must consider that the scaling factor $\lambda_0^3 = 11688.2$ magnifies these fluctuations by four orders of magnitude. Results for the $n = 3$ state, although calculated, can not be displayed, as the numerical inaccuracy of calculating such small binding energies, now magnified by eight orders of magnitude, becomes much too large.

We now turn to our results for positive scattering lengths, displayed in Fig. 5.6, where the $n_* = 1$ and scaled $n = 2$ results are represented by the solid black and the dashed red lines, respectively. For positive scattering length, the binding energies of the $n = 0$ state quickly move out of the range of validity of our theory, and thus this state does not appear in our graph. Again, we find that the horizontal scale of all states is related by the scaling of the two-body pole energy, $\lambda_0^{n-1}\sqrt{E_2}$. Once again, the functions $G^{(n)}$ vanish at the critical value of the scattering length, or corresponding $\sqrt{E_2}$, in the $r_0 \to 0$ limit, where the bound system now breaks up into an atom-dimer pair. In the LO limit, this critical scattering length is related to the binding energy in the resonant limit by the universal relation [Br06b]:

$$\sqrt{E_{2+}^{(n)}} = 1/a_+^{(n)} = 14.13\sqrt{B_3^{(n)}(E_2 = 0)}. \tag{5.84}$$

Also, the position of the maximum in the rescaled function is at approximately the same position, $\sqrt{E_2} \approx 10.0\kappa_*$, as for the $n_* = 1$ state, although again showing a trend of a slight decrease in the value of the maximum position in going from deeper to

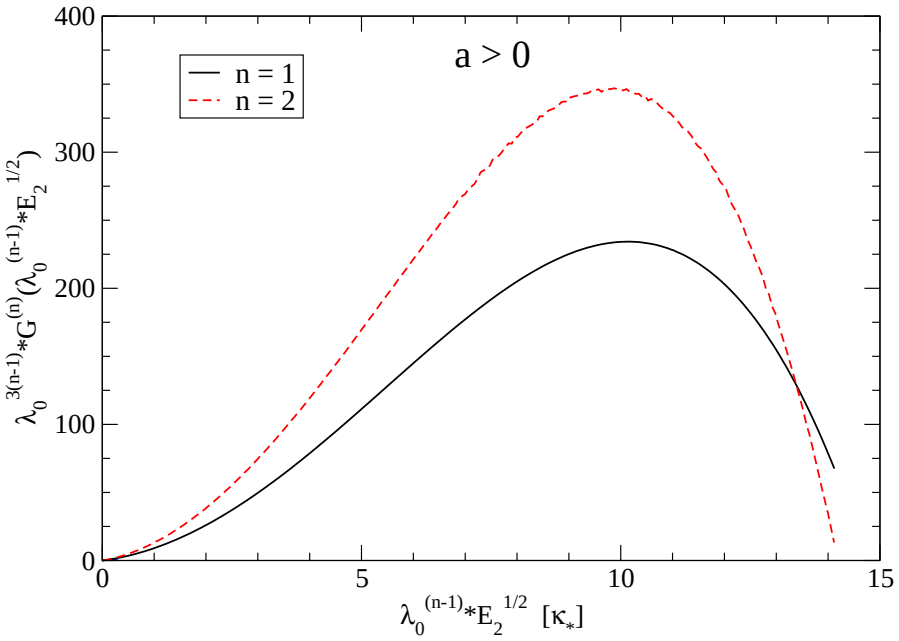

Figure 5.6: The function $G^{(n)}$ for positive scattering lengths, for $n = 1, 2$. Solid black lines represent the results for the $n_* = 1$ state, the state to which our three-body system is renormalized. Results for other states $n \neq 1$ are scaled according to Eq. (5.80); red dashed lines: $n = 2$.

shallower states. The position of this maximum agrees very well with the results for both $n = 1, 2$ found in Ref. [Pl08]. On the vertical scale, the scaling of $G^{(n)}$ according to Eq. (5.80) does bring quantities which differ by four orders of magnitude onto the same scale. However, there is again an obvious deviation from a pure λ_0^3 scaling between neighboring states. As with negative scattering lengths, the trend appears to be toward a larger magnitude of $|G^{(n)}|$ for shallower bound states, except for values approaching the critical scattering length, where $G^{(2)}$ drops much more quickly than $G^{(1)}$. As stated before, the deviation in discrete scaling is encoded in the $\theta^{(n)}$ function, and an investigation into the form of this function will be done in a future work. For positive scattering length, we find a much better agreement on the vertical scale with the results of Ref. [Pl08]. Although the maximum of our $n = 2$ curve does not reach as high, the $n = 1$ results appear to be in close quantitative agreement.

As stated before, in the LO limit, there are universal relations between the three-boson binding energy in the resonant limit and the critical scattering lengths at which the bound state breaks up into three bosons (for $a < 0$, Eq. (5.83)) or an atom-dimer pair (for $a > 0$, Eq. (5.84)). In Fig. 5.4, it can be seen that the positions of these critical scattering lengths are shifted due to NLO corrections. The positions of these critical scattering lengths are important in cold atomic gases in determining the positions of extrema of the three-body recombination rate near a Feshbach resonance [Kr06]. In such Feshbach systems, the effective range of the interaction is related to

n	$C_-^{(n)}$	$C_+^{(n)}$
0	1.4	–
1	2.6	-1.4
2	3.7	-2.0
3	4.8	-2.7
4	6.2	–

Table 5.1: Extracted slopes for the NLO corrections to the critical scattering length which are linear in the effective range, as defined in Eq. (5.85), for both negative ($C_-^{(n)}$) and positive ($C_+^{(n)}$) scattering length. However, the uncertainty in extracting these slopes leads us to an estimated error of $\approx 100\%$ (see text for details).

the width of the Feshbach resonance [Pet06].

For small values of the effective range, we assume that the effective range corrections to the the critical scattering lengths can be treated perturbatively, with the first order correction linear in r_0. We calculate these critical values by finding the value of a for which the kernel of the three-boson integral equation has an eigenvalue of one when the binding energy is set to threshold. Discrete scale invariance in the LO limit suggests that there should be an approximate discrete scaling relation between the NLO corrections for different Efimov states. Therefore, we look at the linear effective range corrections to the critical scattering lengths normalized by the LO critical a scale:

$$\frac{a_\pm^{(n)}(r_0)}{a_\pm^{(n)}(0)} = \frac{\tilde{a}_\pm^{(n)}(0)}{a_\pm^{(n)}(0)} + C_\pm^{(n)} \frac{r_0}{|a_\pm^{(n)}(r_0)|} + \dots \ , \tag{5.85}$$

where $a_\pm^{(n)}(0)$ is the LO critical scattering length calculated from the integral equation, and $\tilde{a}_\pm^{(n)}(0)$ is found from the fit to our data. The slope $C_\pm^{(n)}$ is extracted by fitting a straight line to $a(r_0)/a(0)$ vs. $r_0/|a(r_0)|$ data for small values of $|r_0|$. The extraction of this slope is numerically delicate, as a small change in r_0 produces only a minor shift in $a_\pm$. Therefore, there is a large uncertainty in fitting a straight line to the data. The uncertainty that this creates in the quantitative results presented here will be discussed shortly.

Results for extracted values of $C_\pm^{(n)}$ are displayed in Table 5.1. These results were extracted from two different sets of data, using two different three-body parameters in the renormalization of the three-body system. For $C_-^{(0)}$ and all $C_+^{(n)}$, in order to have critical scattering lengths which were large in comparison to the range of r_0 values used in the fit, we renormalized the three-body system such that, for all r_0 values, we fixed the cutoff to $\Lambda = 1000\kappa_*$, and then tuned the three-body term $H(\Lambda)$ so that the binding energy of the $n = 1$ state in the resonant limit was $B_3^{(1)}(a = \pm\infty) = 10.0\kappa_*^2$. However, for the results found for $C_-^{(n)}$ when $n > 0$ we required that the critical scattering lengths be far enough away from the resonant limit as to reduce numerical

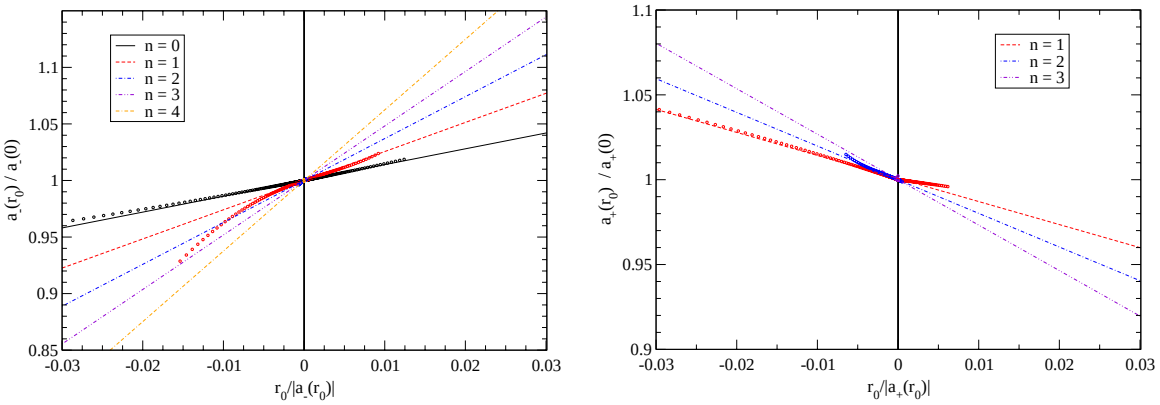

Figure 5.7: Left panel: The negative critical scattering length, where a bound three-boson state breaks up into three bosons, as a function of the effective range of the interaction. Right panel: The positive critical scattering length, where a bound three-boson state breaks up into an atom-dimer pair, as a function of the effective range of the interaction. Circles: data points computed from the NLO three-boson bound state integral equation. Lines: linear fit to the data for small r_0.

inaccuracy. For this reason, we fixed $\Lambda = 10000\kappa_*$, and tuned the three-body term so that the $n = 2$ state had a binding energy $B_3^{(2)}(a = \pm\infty) = 10.0\kappa_*^2$. These renormalization procedures allowed for a cutoff large enough to reduce higher order $1/\Lambda$-suppressed corrections. Even with this renormalization, $a_+^{(0)}$ is at a threshold energy which is too high to fall within the validity of our effective theory. Also, data collected for $a_+^{(4)}$ was dominated by numerical fluctuations, and could not be used. The slopes were then extracted from a straight line fit to values of $|r_0| \leq 0.0001\kappa_*^{-1}$. Interestingly, we found that the extracted values for $C_-^{(1)}$ and $C_-^{(2)}$ were approximately the same using both sets of data. In Fig. 5.7 we have plotted the data sets used in extracting the slopes found in Table 5.1, along with the corresponding linear fits.

Qualitatively, we can conclude that for increasing effective range r_0 the absolute value of the negative critical scattering length $|a_-|$ increases, while the absolute value of the positive critical scattering length $|a_+|$ decreases. Also, the relative magnitude of this shift appears to increase when going from deeper to shallower states (similarly to the magnitude of the $G^{(n)}$ function).

Quantitatively, the relatively large uncertainty in extracting the slopes from our data, along with other theoretical considerations, raise troubling questions about the accuracy of our quantitative results, as displayed in Table 5.1. As mentioned before, the shift in $a_\pm$ is very small for the small r_0 values used in our data sets. The shift due to r_0 is often smaller than the relative shift in $a_\pm$ when using a different cutoff Λ in the renormalization procedure. Also, the smallest reliable numerical accuracy is often of the same order of magnitude as the $a_\pm$ shift. From this, we would conclude that the extracted slopes have an error of the same order of magnitude as the result.

It is, therefore, somewhat surprising that the extracted slope for the $n = 0$ state, $C_-^{(0)} = 1.4$, matches well with the similar study done by Thøgersen et al.: $C_-^{(0)} = 1.3$ [Thog08]. Also, the data points found in [Thog08] for $n = 1, 2$, fall very close to the corresponding linear fits presented here.

More questions arise when theoretical considerations of the discrete scaling invariance are taken into account. Due to this scale invariance, there is no way for the system to know which state n corresponds to the ground state of the physical system. In the LO limit, one can find the exact same low-energy physics by taking one system and multiplying all quantities by the appropriate power of the discrete scaling factor λ_0. Consequently, to LO, an arbitrary state n can always be interpreted as the ground state, with the $(n+1)$th state the first excited state, *etc.* Accordingly, we could renormalize two different systems such that, for example, in the first system the $n = 1$ and in the second system the $n = 2$ state both reproduce the same three-body observable. To LO, due to discrete scale invariance, these two systems would be identical, and give (up to higher order effects) the same results. Therefore, for this discrete scale invariance to also appear in the NLO corrections, we would assume that the slopes found from two different renormalizations, as long as we renormalize in such a way as to reproduce the same three-body observable, should be the same. However, this is not the case found here. As explained above, we extracted slopes from two different sets of data. In the first, the $n = 1$ state was renormalized such that $B_3^{(1)}(a = \pm\infty) = 10.0\kappa_*^2$, and in the second, the $n = 2$ state was renormalized such that $B_3^{(2)}(a = \pm\infty) = 10.0\kappa_*^2$. Discrete scale invariance would then suggest that $C_\pm^{(1)}$ from the first set would be equal to $C_\pm^{(2)}$ from the second set. But, this is not what we have found from our results. This could, of course, be due to the uncertainty in the linear fit, as described above, or it could suggest a deviation from the simple discrete scale invariance for finite values of the scattering length similar to that seen in the $G^{(n)}$ function.

Lastly, we find that there is also a rather large uncertainty arising from the chosen value of Λ used in the renormalization procedure. Although low-energy observables should be independent of Λ, the extracted slopes found when using different cutoffs show a much larger Λ dependence than expected. As a general trend, the absolute value of the slopes $|C_\pm^{(n)}|$ decreases slowly as Λ increases.

We conclude that although the qualitative results for the shift in the critical scattering lengths confirms those found previously [Pl08, Thog08], a much more rigorous investigation must be done to make definite quantitative conclusions.

5.3.2 Range Corrections to Three-Boson Mean Square Radii

Since the first studies of the Efimov effect [Ef70], it has been interpreted that the bound three-body state decays into three free particles as the threshold at negative critical scattering length is crossed, while on the other end of the spectrum, the decay is into an atom-dimer pair at the positive critical scattering length. This implies that

the structure of the three-body bound state moves toward three free particles at large distance from each other, or a bound dimer state with a loosely bound atom at large distance, as the respective thresholds are approached [Br06b].

This feature of the three-body state near the critical scattering lengths, along with the corresponding effective range corrections arising at NLO, is best seen in the mean square radii. The mean square radii for our three-body bound states are calculated from the matter density form factors in the low momentum transfer region. The matter density form factor is defined as the Fourier transform of the matter density:

$$\mathcal{F}(k^2) = \int \rho(\vec{x}) e^{i\vec{k}\cdot\vec{x}} d^3x, \tag{5.86}$$

with the normalization $\mathcal{F}(k^2 = 0) = 1$. In the low momentum transfer region, the exponential can be expanded, and assuming a spherically symmetric matter density, we see that the slope of the form factor determines the mean square radius $\langle r^2 \rangle$:

$$\begin{aligned} \mathcal{F}(k^2) &= \int \rho(\vec{x}) \left(1 + i\vec{k}\cdot\vec{x} - \frac{(\vec{k}\cdot\vec{x})^2}{2} + \dots \right) d^3x \\ &= 1 - \frac{1}{6} k^2 \left\langle r^2 \right\rangle + \dots . \end{aligned} \tag{5.87}$$

Of course, the mean square radius acquired depends on the choice of one- or two-body form factor, which are calculated from the the full wave function in Eqs. (5.76, 5.77, 5.78). Recall that the three-boson system is found from the derived formulas for $2n$ halo nuclei by setting all parameters related to the core c equal to those of the neutron n: i.e. the core mass $A = 1$, and all scattering lengths $a_{nn} = a_{nc} = a$ and effective ranges $r_{nn} = r_{nc} = r_0$. The Jacobi momentum states are especially well suited to explore the structure of the Efimov trimer as it is related to the two-body subsystem (dimer), and the spectator boson (atom)[2]. Since $\vec{p}$ describes the relative momentum of the two bosons in the two-body subsystem, the slope of $\mathcal{F}_{nn}(k^2)$ will give the mean square distance between the two bosons in the two-body subsystem $\langle r^2_{nn} \rangle$. Analogously, because $\vec{q}$ describes the momentum of the spectator boson relative to the center of mass of the two-body subsystem, the slope of $\mathcal{F}_n(k^2)$ will give the mean square distance of the spectator boson from the center of mass of the two-body subsystem $\left\langle r^2_{n-nn} \right\rangle$. However, it is more useful to calculate the distance of the spectator boson from the center of mass of the three-body bound state. If b_n is the slope of the one-body form factor $\mathcal{F}_n(k^2)$ at the limit $k^2 = 0$, the mean square radius of the spectator boson from the three-body center of mass is given by:

$$\left\langle r^2_n \right\rangle = -\frac{8}{3} b_n. \tag{5.88}$$

[2]In order to keep a connection to the equations derived in Sec. 5.2.2, we represent a boson with the subscript n in the analysis that follows.

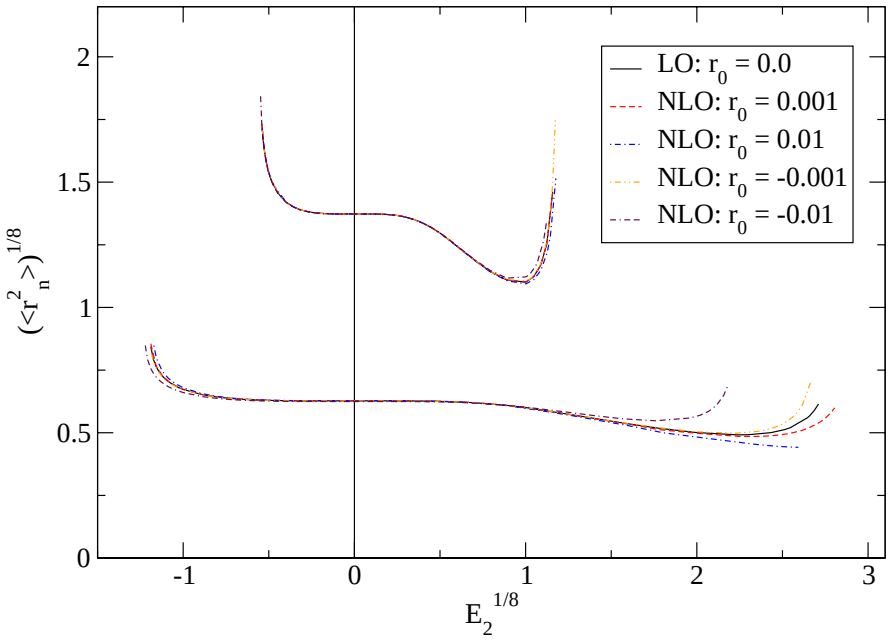

Figure 5.8: Mean square distance of the spectator particle from the three-body center of mass $\langle r_n^2 \rangle$ as a function of the two-body pole energy E_2. Negative values on the E_2-axis correspond to negative scattering lengths a. All quantities in units of the appropriate power of an arbitrarily chosen momentum scale κ_* (see text for details). Mean square distance and the two-body pole energy are both scaled by a power of 1/8 so that multiple bound states can be displayed. Results shown for multiple values of the effective range r_0.

We have extracted the radii by fitting a polynomial in k^2 to the form factor results for small k^2. We have used polynomials of varying degree up to 5th order in k^2 in order to verify the stability and convergence of the fit. We have found a satisfactory stability in the slope when fitting to a polynomial to the fourth order in k^2, up to a value of k^2 at which the form factor has dropped less than 10 percent.

We show the results for $\langle r_n^2 \rangle$, in Fig. 5.8, and $\langle r_{nn}^2 \rangle$, in Fig. 5.9, as functions of the two-body pole energy E_2 for two neighboring Efimov states, where negative values on the E_2-axis correspond to negative scattering lengths a. We have scaled the mean squared radii and the two-body pole energy by a power of 1/8 so that a greater range of the bound state spectrum can be displayed, as the discrete scaling factor λ_0 is reduced from 22.7 to $22.7^{1/8} = 1.48$. All quantities are found in units of the appropriate power of an arbitrarily chosen momentum scale κ_*. As mentioned earlier, we require one three-body parameter in order to renormalize the three-body system. We have renormalized in the same way as was done for the results shown in Fig. 5.4, by tuning the three-body term $H(\Lambda)$, for a fixed $\Lambda = 200.0\kappa_*$, such that the state with index $n_* = 1$ has a binding energy of $B_3^{(1)} = 10.0\kappa_*^2$ in the resonant limit $E_2 = 0$.

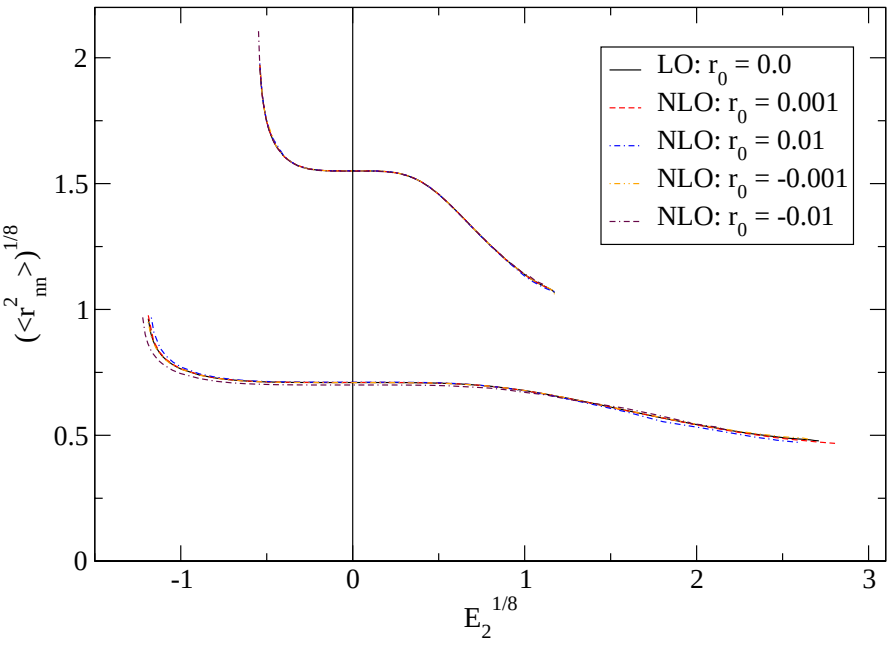

Figure 5.9: Mean square distance between the two particles in the two-body subsystem $\langle r_{nn}^2 \rangle$ as a function of the two-body pole energy E_2. Negative values on the E_2-axis correspond to negative scattering lengths a. All quantities in units of the appropriate power of an arbitrarily chosen momentum scale κ_* (see text for details). Mean square distance and the two-body pole energy are both scaled by a power of $1/8$ so that multiple bound states can be displayed. Results shown for multiple values of the effective range r_0.

Therefore, the mean square radii shown in Figs. 5.8, 5.9 are those corresponding to the binding energies shown in Fig. 5.4, for the states with indices $n = 1, 2$.

Here we see clearly the change in the three-body structure as the bound state approaches the critical scattering lengths. For negative scattering lengths, there is not a large change in either mean square radius until the critical scattering length is approached. By increasing the magnitude of the two-body virtual energy toward this point, both $\langle r_n^2 \rangle$ and $\langle r_{nn}^2 \rangle$ increase dramatically, as the bound three-body system breaks up into three free particles.

On the other side of the spectrum, as the two-body bound state energy is increased, or accordingly the positive scattering length decreased, the size of the three-body system begins to decrease. Then, as the critical scattering length is approached, the distance of the spectator particle from the three-body center of mass increases dramatically, while the distance of the particles in the two-body subsystem continues to decrease. This confirms that the positive critical scattering length corresponds to the threshold of a bound three-body state breaking up into an atom-dimer pair.

We explore NLO corrections to the mean square radii by plotting the mean square

radii results calculated for four non-zero effective ranges in Figs. 5.8, 5.9. We see that the only recognizable corrections occur at scattering lengths approaching the critical values. The shift in the critical scattering length due to a non-zero effective range, as described in the previous subsection, determines where the bound state breaks up and, therefore, where the corresponding mean square radius will increase toward infinity. For negative scattering lengths, a positive(negative) effective range leads to an increase(decrease) in the mean square radius. The opposite sign on the scattering length leads to exactly the opposite behavior. For positive scattering lengths, a positive(negative) effective range leads to a decrease(increase) in the mean square radius. This observed shift of the mean square radii for non-zero effective ranges is related to the corresponding shift of the binding energies of these states, as seen in Fig. 5.4. Specifically, in the resonant limit, $E_2 = 0$, when we force the shift of one of the Efimov states to be zero by our renormalization procedure, the shift for all states in the resonant limit is zero, up to higher order corrections.

The result for $r_0 = 0.01\kappa_*^{-1}$ appears to have an anomalous characteristic as it approaches the positive critical scattering length. First off, the position of the critical scattering length is shifted in the wrong direction from the LO result. Also, the distance of the spectator particle from the center of mass $\langle r_n^2 \rangle$ does not increase to infinity in approaching this threshold. However, this anomaly occurs due to the effective range being in the same order of magnitude as the critical scattering length, $a_+ \approx 0.02\kappa_*^{-1}$. Therefore, this result does not fulfill the condition of our effective theory, that the scattering length be much larger than the range of the interaction.

5.4 Effective Range Corrections to $2n$ Halo Nuclei

In Ch. 4, we performed the LO calculations of low-energy observables of three-body halo nuclei composed of a core and two valence neutrons, including an exploration of the Efimov effect, or the possibility thereof, in $2n$ halo nuclei (Sec. 4.3), as well as a look into the structure of halo nuclei focusing on the matter density form factors and the mean square radii (Sec. 4.4). We now turn to exploring the NLO corrections to these results arising from the effective range of the two-body interactions. We start in the following subsection by looking at range corrections to the results of Sec. 4.3.2 on the possibility of the Efimov effect in $2n$ halo nuclei, as well as Sec. 4.3.3 on the binding energy of a possible Efimov excited state in ^{20}C. After that, in Sec. 5.4.2, we estimate effective range corrections to the mean square radii results first calculated in Sec. 4.4.3.

5.4.1 Range Corrections to $2n$ Halo Nuclei Binding Energies

One of the main achievements of Sec. 4.3.2 was the calculation of boundary curves representing the existence of an excited Efimov state for various values of the core mass in the parametric region defined by the ratios $\sqrt{E_{nc}/B_3^{(n)}}$ versus $\sqrt{E_{nn}/B_3^{(n)}}$,

shown in Fig. 4.4, where E_{nc} and E_{nn} are the n-c and n-n two-body energies related to the S-wave scattering length to LO through Eq. (4.1). Recall that in Fig. 4.4, all points which lie within the boundary curve have at least one excited Efimov state above the state with energy $B_3^{(n)}$, while points outside the curve have no excited states above this state. The curve itself is built up of the points for which the $B_3^{(n+1)}$ binding energy is equal to the scattering threshold. This is equivalent to finding the critical scattering lengths of the three-body system, as was done for the three-boson system in Sec. 5.3.1. There it was observed that including a non-zero effective range shifted the position of the critical scattering lengths.

Therefore, we would assume that there is an analogous shift in the boundary curves when calculated to NLO. We could observe this shift by again calculating the boundary curves in the $\sqrt{E_{nc}/B_3^{(n)}}$ versus $\sqrt{E_{nn}/B_3^{(n)}}$ plane, where now, for a fixed value of the effective range, we would find the two-body energies E_{ni} to NLO in terms of the scattering length a_{ni} and the effective range r_{ni}, where $i = n, c$, through Eq. (5.37). However, for all values of effective ranges r_{nc} and r_{nn} which fulfill the conditions of our effective theory ($r_{ni} \ll a_{ni}$), the shift in the boundary curves is so small as to be nearly unrecognizable from the LO results. Also, the NLO results suffer from the same uncertainty issues as the shift in critical scattering lengths for the three-boson system (see Sec. 5.3.1), specifically, that the higher order theoretical corrections are of the same order of magnitude or larger than the shifts due to the effective range. Therefore, we conclude that the shifts are so small that boundary curves calculated with a non-zero effective range are, up to higher order effects, nearly identical to those already found in Fig. 4.4.

This means that the only halo candidate that has any possibility of an excited Efimov state is still ^{20}C, due to the large uncertainty in the n-^{18}C bound state energy. The central value for the n-^{18}C bound state energy, $E_{nc} = (162 \pm 112)$ keV [Aud95], lies almost exactly on the boundary region for $A = 18$ in Fig. 4.4. The large error in this value, however, dips well into the region where at least one excited Efimov state can occur. The error in the three-body ground state energy of ^{20}C is small compared to E_{nc}. Thus, in Sec. 4.3.3, we calculated the value of the excited state energies to LO as a function of E_{nc}, using the standard value for $a_{nn} = (-18.7 \pm 0.6)$ fm [Gon99], and fixing the cutoff to reproduce the experimental value of the ground state energy $B_3^{(0)} = 3506.0$ keV [TUNL, Aud95], as seen in Fig. 4.6.

We would now like to calculate the NLO corrections to these excited state energies by including the effective ranges of both the n-n and the n-^{18}C interactions. However, there is to date no reliable experimental value for the n-^{18}C S-wave effective range. Therefore, we will need to use an educated estimate for the effective range of this two-body interaction. Also, the n-n effective range has an accepted value of $r_{nn} = (2.75 \pm 0.11)$ fm [Mi90]. However, the size of this effective range is only slightly larger than the inverse of the pion mass scale, and our effective potential, made up of contact interactions, will break down for momenta of the order of the pion mass scale. We therefore use the inverse of the pion mass, $m_\pi = 140$ MeV, to estimate the effective

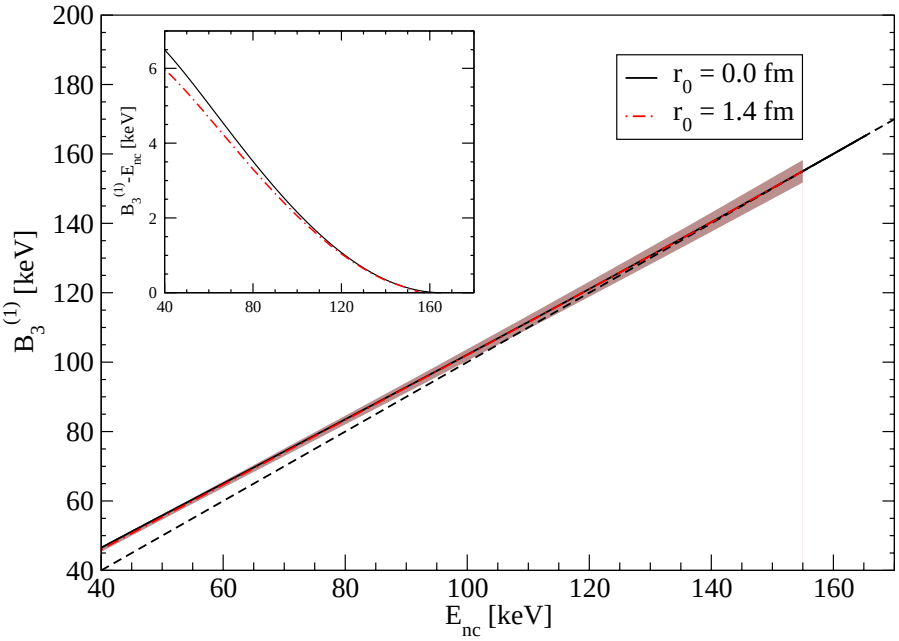

Figure 5.10: Binding energy of the ^{20}C excited Efimov state as a function of the n-^{18}C bound state energy to LO (solid black line) and NLO (dotted-dashed red line) with NLO error bands. The dashed line represents the scattering threshold which is given by $B_3^{(1)} = E_{nc}$. The inset shows the excited state energy relative to the scattering threshold.

ranges of both the n-n and the n-^{18}C interactions, $r_{nn} = r_{nc} \approx 1/m_\pi = 1.4$ fm. This can be interpreted as the maximum effective range allowed by our effective potential.

We use this estimation for the effective ranges r_{nn} and r_{nc}, along with the standard value for a_{nn}, to calculate the excited state energies as a function of E_{nc} to NLO, by fixing our cutoff Λ and tuning the three-body term $H(\Lambda)$ to reproduce the experimental value of the ground state energy $B_3^{(0)} = 3506.0$ keV [TUNL, Aud95]. Recall, the scattering lengths are related to the two-body energies to NLO through Eq. (5.37). Due to the Wigner bound, which limits the maximum positive effective range for a chosen finite Λ, or vice versa (see Sec. 5.1.3), some care must be taken in choosing Λ. Unfortunately, for the range of scattering lengths, or corresponding two-body energies, which we wish to explore, using the inverse of the pion mass to estimate the effective range leads to a maximum value for the cutoff of $\Lambda \leq 500$ keV, which is not much larger than the order of magnitude of the momentum scale of the ^{20}C ground state. For our calculations we use a cutoff $\Lambda = 490$ keV.

The NLO result along with the LO result from Sec. 4.3.3 are plotted in Fig. 5.10, where the solid black line is the excited state energy to LO, the dotted-dashed red line to NLO, and the dashed line represents the scattering threshold. The inset graph shows the excited state energy relative to the scattering threshold. Whereas the excited state in the LO calculation exists when $E_{nc} < 165$ keV, the state to NLO only

exists when $E_{nc} < 155$ keV. For larger values of E_{nc}, the ^{20}C system moves across the scattering threshold, and the excited Efimov state is destroyed. We also see that the effective range corrections lead to a shift toward smaller binding energies. However, this shift is incredibly small, no greater than ≈ 1 keV over the whole range of E_{nc} values, and always smaller than the NLO error bands.

We have estimated this NLO error using the theoretical uncertainty of our effective potential. The uncertainty in binding energies calculated using the two-body effective potential of Eq. (5.1) is $\approx (r_0/a)^2$. For effective ranges much smaller than the scattering length we know that $1/a^2 \approx 2\mu E$. Therefore, we calculate the theoretical uncertainty in the binding energy of the excited state using the sum of the uncertainties from the n-n and n-^{18}C interactions: $(r_{nn}/a_{nn})^2 + r_{nc}^2(2\mu_{nc}E_{nc})$.

5.4.2 Range Corrections to 2n Halo Nuclei Mean Square Radii

In this subsection, we will look at the NLO corrections to the mean square radii of $2n$ halo nuclei when we include the effective range of the two-body interactions. A detailed description of the mean square radii and geometry of $2n$ halo nuclei is given in Sec. 4.4.3, where more detail of the formalism can be found. We review only the necessary information here.

The mean square radii are calculated from the matter density form factors in the low momentum transfer region, where the slope of the form factor determines the mean square radius $\langle r^2 \rangle$ (see Eq. (4.71)):

$$\mathcal{F}(k^2) \;=\; 1 - \frac{1}{6}k^2 \left\langle r^2 \right\rangle + \dots \,. \tag{5.89}$$

Of course, the mean square radius acquired depends on the choice of one- or two-body form factor. Recall that these matter density form factors are calculated from the full wave function of the three-body system through Eqs. (5.76, 5.77, 5.78). The slope of $\mathcal{F}_{ni}(k^2)$, where $i = n, c$, will give the mean square distance between the two particles in the chosen two-body subsystem, either $\langle r_{nn}^2 \rangle$ or $\langle r_{nc}^2 \rangle$. Analogously, the slope of $\mathcal{F}_i(k^2)$, will give the mean square distance of the spectator particle from the center of mass of the two-body subsystem, either $\left\langle r_{c-nn}^2 \right\rangle$ or $\left\langle r_{n-nc}^2 \right\rangle$. However, it is more useful to calculate the distance of the individual particles from the center of mass of the three-body bound state. If b_i is the slope of the one-body form factor $\mathcal{F}_i(k^2)$ at the limit $k^2 = 0$, the mean square radius of one of the bodies i from the three-body center of mass is given by:

$$\left\langle r_i^2 \right\rangle = -6b_i \left(1 - \frac{m_i}{2m_n + m_c} \right)^2 , \tag{5.90}$$

where m_i is the mass of the desired particle i, and m_n and m_c are the neutron and core masses, respectively.

We have again extracted the radii by fitting a polynomial in k^2 to the form factor results for small k^2. We have used polynomials of varying degree up to 5th order in k^2 in order to verify the stability and convergence of the fit. We have found a satisfactory stability in the slope when fitting to a polynomial to the fourth order in k^2, up to a value of k^2 at which the form factor has dropped less than 10 percent.

In Sec. 4.4.3, we found that to LO there is a universal relation between the radii of neighboring Efimov states. Namely, the ratio of the mean square radii for neighboring states in the resonant limit, $a \to \pm\infty$, approaches the universal factor λ_0^{-2} as the threshold is approached, $n \to \infty$, Eq. (4.73). We also showed in Sec. 5.3.2, that for the three-boson system, up to higher order corrections, a non-zero effective range produces no shift in the radii in the resonant limit, as long as the shift in one of the Efimov states is forced to zero by our renormalization procedure. We have confirmed that this universal property also occurs in the general $2n$ halo nucleus with an arbitrary core mass A in the resonant limit.

Of further interest is the effective range corrections to the mean square radii of known halo nuclei. However, as was described in the previous subsection, the effective ranges of the various n-c interactions are not well known experimentally. Therefore, we will need to use an estimate for the effective range of our n-c interactions. Also, the n-n effective range has an accepted value of $r_{nn} = (2.75 \pm 0.11)$ fm [Mi90]. However, the size of this effective range is only slightly larger than the inverse of the pion mass scale, and our effective potential, made up of contact interactions, will break down for momenta of the order of the pion mass scale. As before, we use the inverse of the pion mass, $m_\pi = 140$ MeV, to estimate the effective range of both the n-n and the n-c interactions for all $2n$ halo nuclei, $r_{nn} = r_{nc} \approx 1/m_\pi = 1.4$ fm. This can be interpreted as the maximum effective range allowed by our effective potential.

The extracted radii for known halo nuclei to both LO and NLO are shown in Table 5.2. We show only a selection of the LO results found in Table 4.1, to give a general overview of NLO corrections to the LO results. As input we have used the standard value of the n-n scattering length, $a_{nn} = (-18.7 \pm 0.6)$ fm [Gon99], along with the experimental values of the n-c two-body energies E_{nc} shown in the third column of Table 5.2 (negative values correspond to virtual energies). The effective range of both two-body subsystems is shown in the fourth column, indicating which results refer to LO or NLO calculations. The relation between the scattering length a_{ni}, the effective range r_{ni} and the two-body energy E_{ni}, where $i = n, c$, is found in Eq. (5.37). As a three-body input, the three-body term is tuned to reproduce the experimental ground state binding energy $B_3^{(0)}$ shown in the second column of Table 5.2. These experimental values for the two-body and three-body energies are taken from the most recent results of the "Nuclear Data Evaluation Project" of TUNL [TUNL], except where otherwise noted. The cutoff Λ is held constant, but due to the Wigner bound, some care must be taken in choosing Λ. Unfortunately, as first stated in the previous subsection, for the range of scattering lengths, or corresponding two-body energies, which we wish to explore, using the inverse of the pion mass to estimate

Nucleus	B_3 [keV]	E_{nc} [keV]	r_0 [fm]	$\sqrt{\langle r_{nn}^2 \rangle}$ [fm]	$\sqrt{\langle r_{nc}^2 \rangle}$ [fm]	$\sqrt{\langle r_n^2 \rangle}$ [fm]	$\sqrt{\langle r_c^2 \rangle}$ [fm]
^{11}Li	247	-25	0.0	8.7±0.7	7.1±0.5	6.5±0.5	1.0±0.1
	247	-25	1.4	8.87±0.05	7.25±0.04	6.54±0.04	1.044±0.006
	247	-800 [Wil75]	0.0	6.8±1.8	5.9±1.5	5.3±1.4	0.9±0.2
	247	-800 [Wil75]	1.4	6.0±0.4	5.3±0.4	4.7±0.3	0.79±0.05
^{14}Be	1120	-200 [Thoe00]	0.0	4.1±0.5	3.5±0.5	3.2±0.4	0.40±0.05
	1120	-200 [Thoe00]	1.4	3.77±0.07	3.32±0.06	3.04±0.05	0.392±0.007
^{12}Be	3673	503	0.0	3.0±0.6	2.5±0.5	2.3±0.5	0.32±0.07
	3673	503	1.4	3.51±0.15	2.88±0.13	2.62±0.11	0.368±0.016
^{18}C	4940	731	0.0	2.6±0.7	2.2±0.6	2.1±0.5	0.18±0.05
	4940	731	1.4	3.1±0.2	2.7±0.2	2.6±0.2	0.22±0.01
^{20}C	3506	161	0.0	2.8±0.3	2.4±0.3	2.3±0.3	0.19±0.02
	3506	161	1.4	3.25±0.05	2.72±0.04	2.58±0.04	0.209±0.003
	3506	60	0.0	2.8±0.2	2.3±0.2	2.2±0.2	0.18±0.01
	3506	60	1.4	3.08±0.02	2.62±0.01	2.49±0.01	0.203±0.001
^{20}C*	65.0±6.8	60	0.0	42±3	38±3	41±3	2.2±0.2
^{20}C*	64.7±0.7	60	1.4	43.8±0.2	39.5±0.2	43.6±0.2	2.29±0.01

Table 5.2: Various mean square radii of different halo nuclei. The second two columns show the input values for the three-body ground state energy and the two-body n-c energy (negative values corresponding to virtual energies), respectively, as given by [TUNL], except where otherwise noted. The fourth column shows the input value for both two-body effective ranges, related to LO ($r_0 = 0.0$ fm) or NLO ($r_0 = 1.4$ fm) calculations. The rows marked by ^{20}C* show the results for the excited Efimov state of ^{20}C, with binding energy displayed in the second column, which is found above the ground state ($B_3 = 3506$ keV).

the effective range leads to a maximum value for the cutoff for most of the $2n$ halo nuclei of approximately $\Lambda < 500$ keV, which is not much larger than the order of magnitude of the momentum scale of the $2n$ halo systems. This could lead to a fairly large uncertainty in the calculations due to the details of the regulator. For our calculations we use a cutoff $\Lambda = 490$ keV for all nuclei except ^{18}C, for which the relatively large n-^{16}C binding energy constrains the cutoff to just below this value, and we therefore use $\Lambda = 436$ keV.

The NLO theoretical error is again estimated by the uncertainty of the two-body effective potential, Eq. (5.1), which is $\approx (r_0/a)^2$, where r_0 is the effective range of the interaction, and a the scattering length. For effective ranges much smaller than the scattering length we know that $1/a_{nc}^2 \approx 2\mu_{nc}E_{nc}$. The uncertainty in the radii is then calculated from the greater of the error arising from the n-n or n-c interaction: $(r_{nn}/a_{nn})^2$ or $r_{nc}^2(2\mu_{nc}E_{nc})$.

We will now discuss the results for the NLO corrections to the mean square radii, due to the effective range of the interactions. Recall that we have only used an estimated value for the effective range, setting r_0 for both the n-n and the n-c interactions

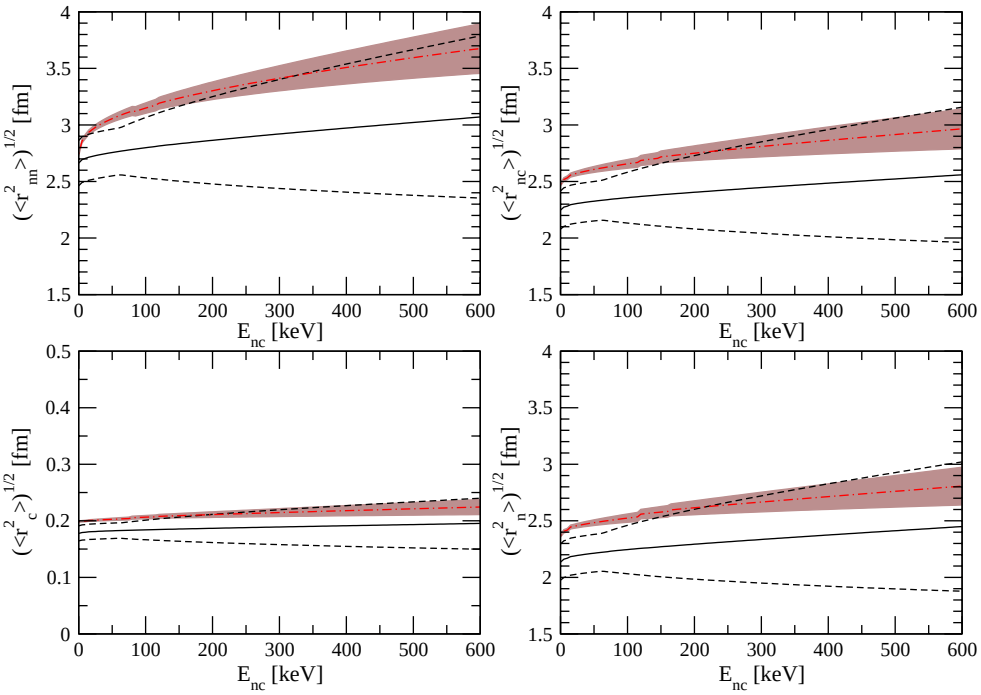

Figure 5.11: The various mean square radii for ^{20}C as a function of the n-^{18}C two-body energy with error bands from the theoretical uncertainty. The LO results represented by the solid black lines, with error bands represented by dashed lines (see Fig. 4.10). The NLO results represented by the red dotted-dashed lines with solid error bands. As input, the n-n scattering length $a_{nn} = -18.7$ fm, the three-body binding energy $B_3^{(0)} = 3506$ keV, and for NLO results the effective range $r_0 = 1.4$ fm were used.

to the inverse of the pion mass. Also, due to the relatively small cutoff Λ which is only slightly larger than the momentum scale of the $2n$ halo nuclei, there is the potential of a large uncertainty arising from regulator effects. Therefore, the results displayed in Table 5.2 give only a general estimate of the NLO shift.

For the *Borromean* halo nuclei ^{11}Li and ^{14}Be, in which all two-body subsystems are unbound, the general tendency is for a positive effective range to shift all mean square radii to smaller values. The only exception is the case of ^{11}Li using the central value of the n-c energy $E_{nc} = (-25 \pm 15)$ keV [TUNL]. This difference seems to be due to the fact that this value of the virtual energy is very close to the resonant limit, while the competing value $E_{nc} = (-800 \pm 250)$ keV [Wil75] is much larger in comparison. The opposite is true for the so called *Samba* halo nuclei ^{12}Be, ^{18}C, and ^{20}C, for which the n-c subsystem is bound. The positive effective range shifts the mean square radii of these halo nuclei to larger values.

We also see that the shift in all mean square radii is relatively small. Except for the ^{20}C ground state, the NLO corrections are all within one error bar of the LO results. The shift is small despite the fact that we have used the maximum estimate

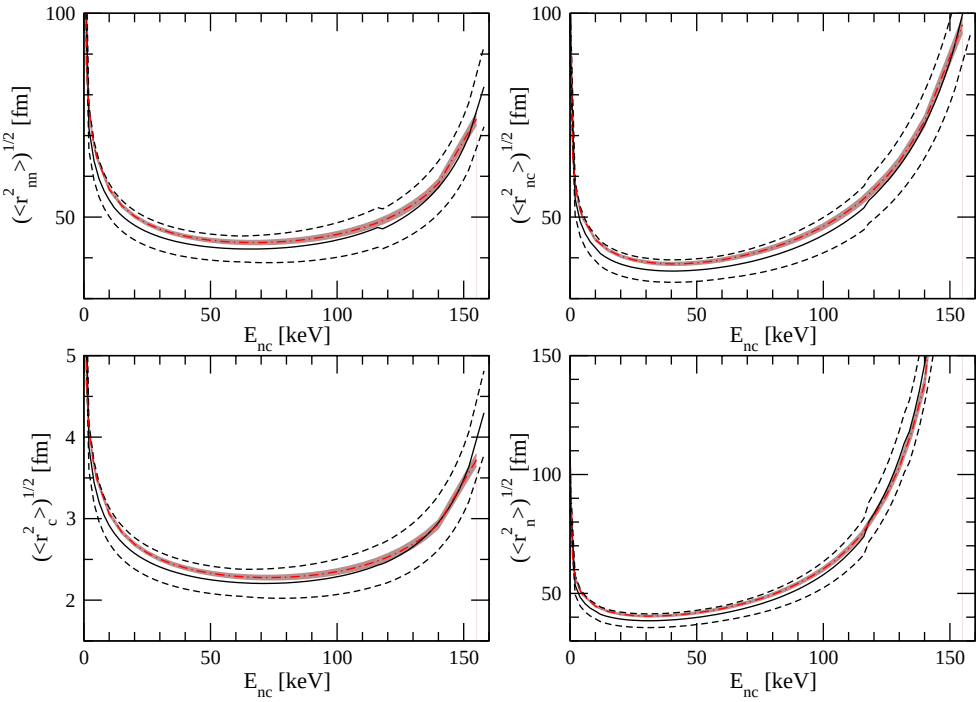

Figure 5.12: The various mean square radii for the Efimov excited state of ^{20}C as a function of the n-^{18}C two-body energy with error bands from the theoretical uncertainty. The LO results represented by the solid black lines, with error bands represented by dashed lines (see Fig. 4.11). The NLO results represented by the red dotted-dashed lines with solid error bands. As input, the n-n scattering length $a_{nn} = -18.7$ fm, the three-body binding energy $B_3^{(0)} = 3506$ keV, and for NLO results the effective range $r_0 = 1.4$ fm were used.

for the effective range which is allowable for our pionless effective theory built up of contact interactions.

We now turn our focus to the case of ^{20}C, as the large uncertainty in the n-c energy, with two competing values, $E_{nc} = (162\pm112)$ keV [TUNL], and $E_{nc} = (530\pm130)$ keV [Na99], suggests that we look at the mean square radii over a range of E_{nc} values. The results, using the central value for the three-body binding energy as input, $B_3^{(0)} = 3506$ keV, were first calculated to LO in Sec. 4.4.3, Fig. 4.10. We have now calculated these values to NLO, using the inverse of the pion mass as an estimation of the effective range, and the results compared to the LO case can be seen in Fig. 5.11, with error bands estimated from the theoretical uncertainty, as described above. The solid black lines represent the LO results, with error bands represented by the dashed lines. The dotted-dashed red lines represent the NLO results, with solid colored error bands. We see that the mean square radii to NLO show the same behavior with changing E_{nc} as the LO case, with an increase in E_{nc} leading to an increase in size. Also we see more clearly the general shift toward larger radii due to the effective range corrections.

As was shown in Sec. 4.3.3, there possibly exists one Efimov excited state in ^{20}C for $E_{nc} < 165$ keV. The NLO corrections to the binding energy of this excited state, using the inverse of the pion mass as an estimation of the effective range, were calculated in Sec. 5.4.1. In Fig. 5.12, the mean square radii for this excited state to NLO are plotted over a range of E_{nc} values, together with the LO results from Fig. 4.11. Again we see that the general behavior of the mean square radii as a function of the two-body energy remains the same when calculated to NLO. At the endpoints, signifying the critical E_{nc} where the excited state breaks up, the mean square radii diverge as the excited state is destroyed and the particles consequently fly apart. The positive shift in the mean square radii for a positive effective range is also seen, although this shift is relatively small, as compared to the relative shift in the ground state radii.

5.5 Conclusion

In this chapter, we have investigated universal aspects of two different three-body systems, identical bosons and $2n$ halo nuclei, within an effective quantum mechanics approach to next-to-leading order. Assuming that the halo nuclei have resonant S-wave interactions between the neutron and the core, the effective potential reduces to a separable S-wave potential. We have shown the renormalization of this potential in detail, which to NLO reproduces the scattering length and effective range, with results analogous to an EFT approach [Br06b]. The corrections at next-to-next-to-leading order in the expansion in M_{low}/M_{high} require no new low-energy parameters [Ham01, Pl06a]. We have derived the two-body T-matrix in such a way as to explicitly keep the regulator factors. This allowed for the elimination of a spurious pole found in the high-momentum region, as long as we properly chose the cutoff parameter Λ. We have also shown that the process of renormalizing the two-body potential, specifically the redefinition of the coupling constants to absorb high-energy effects, leads directly to a derivation of the Wigner bound in momentum space. For a chosen scattering length and effective range, the maximum cutoff allowed by the Wigner bound corresponds to the maximum cutoff which still eliminates the spurious high-energy pole in the T-matrix. Also, we have confirmed Wigner's original prediction, that in the zero-range limit, in which $\Lambda \to \infty$, the effective range must be negative or vanishing [Wig55].

We have also taken another look at the two-body renormalization in terms of a renormalization group, as was done in Refs. [Kap98, Br06b]. We have improved upon these studies by explicitly keeping the regulator factors in the analysis, thereby generating a more general RG trajectory in the limit $\Lambda \to 0$. However, as expected, the results match those found in these previous studies at the other end of the trajectory, $\Lambda \to \infty$, which is the limit desired in calculating physical observables.

We then calculated the effective range corrections to the Efimov plot for three identical bosons, and found results that match well with other recent studies [Pl08, Thog08]. For small r_0, the binding energies of the Efimov trimers will be shifted

linearly in r_0, according to a universal function, Eq. (5.79) [Pl08]. In Ref. [Pl08], it was shown that the NLO corrections to different Efimov states are approximately related to each other through a discrete scale transformation. However, while this discrete scaling is exact (up to higher order corrections in $1/\Lambda$) in the resonant limit, $a \to \pm\infty$, for finite values of $|a|$, there is a breaking of the exact scaling symmetry. We have reproduced the results of [Pl08] for positive scattering length, and have improved upon them for negative scattering length, displaying multiple Efimov states, and thereby confirming the approximate scale transformation in this region. With an improvement of numerical accuracy, it could be possible to investigate the breaking of discrete scale invariance in the NLO corrections away from the resonant limit.

Important in recombination rate experiments with ultracold atoms near a Feshbach resonance is the position of the critical scattering length, where the Efimov trimer breaks up either into three separate atoms or into an atom-dimer pair. The positions of these critical scattering lengths determine the positions of extrema of the three-body recombination rate near a Feshbach resonance [Kr06]. In such Feshbach systems, the effective range of the interaction is related to the width of the Feshbach resonance [Pet06]. We have confirmed the qualitative results of [Thog08], that for increasing effective range r_0 the absolute value of the negative critical scattering length $|a_-|$ increases. We have also shown that for increasing effective range r_0 the absolute value of the positive critical scattering length $|a_+|$ decreases. Also, the relative magnitude of this shift appears to increase when going from deeper to shallower states. However, it is difficult to conclude anything quantitatively from our calculations, as the magnitude of the shifts is of the same size as higher order corrections and numerical uncertainty inherent in the problem.

We then showed effective range corrections to the structure of the Efimov trimers over a range of scattering lengths. By calculating the mean square distance of the spectator particle as well as the distance between the two particles in the dimer subsystem, we confirmed that at the negative critical scattering length, the trimer breaks up into three free particles, while at the positive critical scattering length, the trimer breaks up into an atom-dimer pair [Ef70]. We also observed a shift of the mean square radii for non-zero effective ranges, which is related to the corresponding shift of the binding energies of these states. For negative scattering lengths, a positive(negative) effective range leads to an increase(decrease) in the mean square radius. However, for positive scattering lengths, a positive(negative) effective range leads to a decrease(increase) in the mean square radius. In a future study, it would be interesting to see if the corrections to the mean square radii for small r_0 obey the same universal function, with the same approximate scaling transformation, as was found for the binding energies. If so, one could possibly investigate the deviations from exact scale invariance more easily by calculating the effective range corrections to the dimensionless quantity $(\langle r^2 \rangle B_3)$.

Next, we turned our attention back to $2n$ halo nuclei, and calculated the NLO correction to the parametric boundary curves within which at least one excited Efimov state will occur. However, because the neutron-core effective range is not well

known experimentally, we used the inverse of the pion mass, $1/m_\pi = 1.4$ fm, as an estimate for all effective ranges in the $2n$ halo system. We found that the correction to the boundary curves was almost unrecognizable for this value of the effective range. Therefore, the only halo candidate that has any possibility of an excited Efimov state is still ^{20}C. Using the estimated effective range, the magnitude of the excited state binding energy decreased very slightly from the LO results, and the value of the n-^{18}C two-body energy at which this excited state is destroyed was also decreased.

We finished by calculating the shift from the LO results in the mean square radii for known $2n$ halo nuclei, again using the inverse of the pion mass as an estimate for all effective ranges. We found that for *Borromean* halo nuclei, the general tendency is for a positive effective range to shift all mean square radii to smaller values, unless the two-body n-c virtual energy is very close to threshold. The opposite was found to be true for the so called *Samba* halo nuclei, for which the n-c subsystem is bound. The positive effective range shifts the mean square radii of these halo nuclei to larger values. Also, the shift found using our estimated value of the effective ranges was always small relative to the theoretical error in the problem. For a better physical description, it will be necessary to experimentally measure the as yet unknown parameters, specifically the various neutron-core scattering lengths and effective ranges. With new improved experimental data for these weakly bound nuclei (from such facilities as FAIR and FRIB), much more knowledge can be obtained about the structure of these interesting systems as well as discovering whether they show universal behavior and excited Efimov states.

On the theoretical side, it would be beneficial in the future to use an effective theory which does not suffer from the Wigner bound, such as those employed in e.g. [Ham06, Pl08]. The value of the effective range used in these calculations constrained the maximum value of Λ to values that were at times of the same order of magnitude as the ground state binding energy of the $2n$ halo nuclei being explored. This not only added to the amount of theoretical uncertainty, but also increased the level of numerical uncertainty involved in extracting the mean square radii from the matter density form factors. It is hoped that such an effective theory, which eliminates this constraint, would also give more accurate results in all three-body systems for such quantities as, for example, the critical scattering lengths, so that better quantitative predictions of effective range corrections could be made.

Chapter 6

Scattering Properties of the $X(3872)$

In this chapter, we move away from the bound state problem, and turn our focus toward three-body scattering with large scattering lengths. If the scattering length is positive, there exists a two-body bound state known as a *dimer*, which, in the three-body problem, can scatter off a single particle. Also, we no longer work with the quantum mechanics framework of the previous chapters, but rather exchange this in favor of an effective field theory (EFT). A novel approach using a pionless EFT to describe particle-dimer scattering involving three identical bosons was developed in Ref. [Bed99], and reviewed in detail in Ref. [Br06b]. A generalization of this EFT can be made to three-body systems in which two of the particles are identical (or at least have the same mass), interacting with a particle of different mass. This could then be applied to scattering in the $2n$ halo nucleus system. However, in what follows, we will develop and apply this EFT in the growing field of mesonic molecules.

In recent years a cornucopia of new and possibly exotic charmonium states has been discovered at the B-factories at SLAC and at KEK in Japan, and at the CESR collider at Cornell. This has revived the field of charmonium spectroscopy [Sw06, Ei07, Vo07, God08]. Such studies will also be an important part of PANDA at the FAIR facility. Some of the new states are very close to scattering thresholds and can be interpreted as hadronic molecules. A particularly interesting example is the $X(3872)$ which was discovered by the Belle collaboration [Ch03] in $B^{\pm} \to K^{\pm}\pi^{+}\pi^{-}J/\psi$ decays and shortly after confirmed by the CDF collaboration in $p\bar{p}$ collisions [Ac04]. This state has quantum numbers $J^{PC} = 1^{++}$ and is very close to the $D^{*0}\bar{D}^{0}$ threshold.[1] As a consequence, the $X(3872)$ has a resonant S-wave coupling to the $D^{*0}\bar{D}^{0}$ system. Many studies have addressed the nature of the $X(3872)$ and provided predictions for its decay modes based on the assumption that it is a $D^{*0}\bar{D}^{0}$ molecule with even

[1] Note, however, that $J^{PC} = 2^{-+}$ can not be excluded at present.

C-parity:

$$(D^{*0}\bar{D}^0)_+ \equiv \frac{1}{\sqrt{2}}\left(D^{*0}\bar{D}^0 + D^0\bar{D}^{*0}\right) . \tag{6.1}$$

A recent status report can be found in Ref. [Br08d].

The measured mass and width of the $X(3872)$ differ significantly in the $J/\psi\pi^+\pi^-$ and $D^{*0}\bar{D}^0$ channels. This effect can be understood from a line shape analysis which shows that the true mass and width of the $X(3872)$ are measured in the $J/\psi\pi^+\pi^-$ channel because the $D^{*0}\bar{D}^0$ channel is contaminated by a threshold enhancement [Br07, Br08a]. Using the latest measurements in the $J/\psi\pi^+\pi^-$ channel [Ada08, Aub08, CDF08], the mass of the $X(3872)$ is [Br09]:

$$m_X = (3871.55 \pm 0.20)\ \text{MeV}\,, \tag{6.2}$$

which corresponds to an energy relative to the $D^{*0}\bar{D}^0$ threshold

$$E_X = (-0.26 \pm 0.41)\ \text{MeV}\,. \tag{6.3}$$

The central value corresponds to a $(D^{*0}\bar{D}^0)_+$ bound state with binding energy $B_X = 0.26$ MeV, but a virtual state can not be excluded from the current data in the $J/\psi\pi^+\pi^-$ and $D^{*0}\bar{D}^0$ channels [Hanh07b]. The $X(3872)$ is also very narrow with a width smaller than 2.3 MeV.

Because the $X(3872)$ is so close to the $D^{*0}\bar{D}^0$ threshold, it has universal low-energy properties that depend only on its binding energy [Br06b]. In first approximation, the coupling to charged D mesons can be neglected because the $D^{*+}D^-$ threshold is about 8 MeV higher in energy. As a consequence, the properties of the $X(3872)$ can be described in a universal EFT with contact interactions only. This EFT is also called pionless EFT (see Refs. [Ep08, Ph02, Bed02] and references therein). The study of the $X(3872)$ as a $(D^{*0}\bar{D}^0)_+$ molecule in the pionless EFT was initiated by Braaten and Kusunoki [Br04b]. A number of predictions for production amplitudes [Br04c, Br04d, Br05a, Br06a], decays [Br05b, Br05c, Br06c, Br08b], and line shapes [Br07, Br08a] followed. The interactions of the $X(3872)$ with other hadrons are unknown.

In this chapter, we extend these studies to three-body processes in the pionless EFT. Based on the assumption that the $X(3872)$ is a S-wave $(D^{*0}\bar{D}^0)_+$ molecule, we provide novel predictions for the scattering of D^0 and D^{*0} mesons and their antiparticles off the $X(3872)$ in pionless EFT. This is analogous to particle-dimer scattering in which two of the particles have the same mass, but the third particle has a different mass, where only the particles with different masses have an interaction with a large scattering length. For convenience, we will refer to these reactions collectively as $XD^{(*)}$ scattering in the following. This reaction will contribute to the final state interaction in decays of B_c mesons into D and D^* mesons and to rare events in $B\bar{B}$ production where one of the B's decays into a X and the other one into a D or D^* meson (see the discussion below). In the next section, we will present the EFT for $XD^{(*)}$ scattering. In section 6.2, we will present our results and discuss possible scenarios for observing this process at the LHC or B-factories. We close the chapter with a brief summary and conclusion.

6.1 $XD^{(*)}$ Scattering in Effective Field Theory

In this section, we set up the EFT for $XD^{(*)}$ scattering, derive the integral equation for the scattering amplitude, and provide relations for the total cross section. As mentioned before, such a system is similar to the $2n$ halo nucleus, in that two of the particles have the same mass while the third particle has different mass. Therefore, we expect our results to include factors similar to those found in the bound state equations derived in Sec. 4.2 and Sec. 5.2. For the derivation of the three-body equations, it is convenient to introduce a non-dynamical auxiliary field X for the $X(3872)$. The EFT is organized into an expansion around the non-trivial fixed point corresponding to infinite scattering length or, equivalently, a threshold bound state. The expansion is then in powers of γ/Λ_b, where γ is the binding momentum of the X and Λ_b the breakdown scale of the pionless EFT. To leading order in γ/Λ_b, the effective Lagrangian for the interaction of the $X(3872)$ with the D mesons can be written as:

$$\begin{aligned}\mathcal{L} &= \sum_{j=D^0,D^{*0},\bar{D}^0,\bar{D}^{*0}} \psi_j^\dagger \left(i\partial_t + \frac{\nabla^2}{2m_j} \right) \psi_j + \Delta X^\dagger X \\ &\quad - \frac{g}{\sqrt{2}} \left(X^\dagger (\psi_{D^0}\psi_{\bar{D}^{*0}} + \psi_{D^{*0}}\psi_{\bar{D}^0}) + \text{ H.c. } \right) + \dots \,, \end{aligned} \tag{6.4}$$

where H.c. denotes the Hermitian conjugate and the dots indicate terms with more derivatives and/or fields. Moreover, the D^0, D^{*0}, $\bar{D}^0$, and $\bar{D}^{*0}$ mesons are treated as distinguishable particles. Because of charge conjugation invariance, we have $m_{D^0} = m_{\bar{D}^0}$ and $m_{D^{*0}} = m_{\bar{D}^{*0}}$. The terms with more derivatives are suppressed at low energies, while four- and higher-body forces do not contribute in three-body processes. Since there is no Efimov effect [Ef70] in this system, three-body terms will also not contribute up to next-to-next-to-leading order in the expansion in γ/Λ_b.

The parameters Δ and g in Eq. (6.4) are not independent and only the combination Δ/g^2 enters into physical observables. Since the theory is non-relativistic, all particles propagate forward in time and the tadpoles vanish. The propagator for the $D^{(*)}$ mesons is

$$iS_j(p_0,\vec{p}) = \frac{i}{p_0 - p^2/(2m_j) + i\epsilon} \,, \qquad j = D^0, D^{*0}, \bar{D}^0, \bar{D}^{*0} \,, \tag{6.5}$$

where $p^2 \equiv |\vec{p}|^2$. The X propagator is more complicated because of the coupling to two-meson states. While the bare X propagator is constant, $iD_0(p_0,\vec{p}) = i/\Delta$, it is dressed by D meson loops, which due to the large scattering length must be summed to all orders, as illustrated in Fig. 6.1. The bare and full X propagators are represented by the double dashed and double lines, respectively. The D mesons are represented by the solid (D^0 and $\bar{D}^0$) and dashed lines ($\bar{D}^{*0}$ and D^{*0}). Note that each loop receives contributions from two combinations of D mesons $D^{*0}\bar{D}^0$ and $D^0\bar{D}^{*0}$. Summing the resulting geometric series leads to the full X propagator:

$$iD(p_0,\vec{p}) \;=\; iD_0(p_0,\vec{p}) \left[1 - D_0(p_0,\vec{p})\Sigma(p_0,\vec{p}) \right]^{-1} \,, \tag{6.6}$$

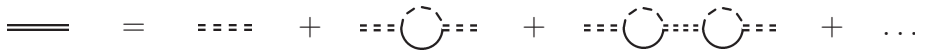

Figure 6.1: Dressing of the bare X propagator (double dashed line) by D meson loops (solid and dashed lines).

where $\Sigma(p_0, \vec{p})$ is the self energy of the X. Using the reduced mass of the D^0 and D^{*0} mesons, $\mu_X = m_{D^0} m_{D^{*0}}/(m_{D^0} + m_{D^{*0}})$, and their total mass, $M_X = m_{D^0} + m_{D^{*0}}$, the self energy can be written

$$\begin{aligned}\Sigma(p_0, \vec{p}) &= -2\mu_X g^2 \int \frac{d^3q}{(2\pi)^3} \left[q^2 - 2\mu_X p_0 + \frac{p^2}{4} + \sqrt{1 - \frac{4\mu_X}{M_X}}\, \vec{p}\cdot\vec{q} - i\epsilon \right]^{-1} \\ &= \frac{2\mu_X g^2}{4\pi} \left[\sqrt{-2\mu_X p_0 + \frac{\mu_X}{M_X} p^2 - i\epsilon} - \frac{2}{\pi}\Lambda + \mathcal{O}(1/\Lambda) \right], \end{aligned} \tag{6.7}$$

where the ultraviolet divergence was regulated with a strong momentum cutoff Λ. Substituting this expression into Eq. (6.6) and dropping terms that vanish as $\Lambda \to \infty$, we obtain the full X propagator:

$$iD(p_0, \vec{p}) = \frac{-i4\pi}{2\mu_X g^2} \left[-\gamma + \sqrt{-2\mu_X p_0 + \frac{\mu_X}{M_X} p^2 - i\epsilon} \right]^{-1}, \tag{6.8}$$

where we have eliminated the coupling constant dependence Δ/g^2 as well as the dependence on Λ, in favor of γ, by matching the pole position

$$\gamma \equiv \frac{1}{a} = \frac{4\pi\Delta}{2\mu_X g^2} + \frac{2}{\pi}\Lambda, \tag{6.9}$$

to the binding energy of the $X(3872)$: $\gamma = \sqrt{2\mu_X B_X}$ and a is the $D^0\bar{D}^{*0}$ scattering length.

The full X propagator can now be used to calculate the scattering of a D^0 or D^{*0} meson (or their antiparticles) off the $X(3872)$. Because of their different masses, the scattering of a D^0 or a D^{*0} will lead to different scattering amplitudes and cross sections even though the interaction strength is the same. The scattering amplitude is the solution of the integral equation shown in Fig. 6.2. The X and the scattered meson, denoted as S, are represented by a double line and a single line, respectively. If an S particle is scattered, a second complementary particle type, denoted by $\bar{S}$, appears as the virtual exchange particle, and is represented by the dashed lines in Fig. 6.2. The masses of the S and $\bar{S}$ particles are different. For a given scattered particle S, the corresponding complementary particle $\bar{S}$ can be read off the flavor wave function of the $X(3872)$ in Eq. 6.1. For example, if $S = D^0$ we have $\bar{S} = \bar{D}^{*0}$, and for $S = D^{*0}$ we have $\bar{S} = \bar{D}^0$.

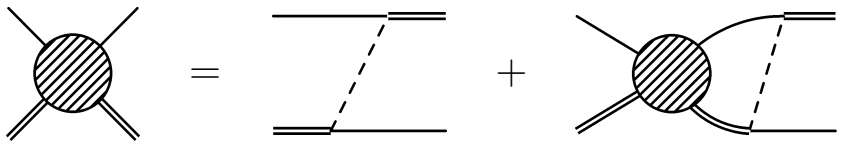

Figure 6.2: Integral equation for scattering of a particle S (single line) off the $X(3872)$ (double line). The dashed line indicates the complementary particle $\bar{S}$ as explained in the text.

We formulate the problem in the center-of-mass system of the XS system. Then, with k the relative momentum of S and X, the total energy is

$$E = \frac{k^2}{2\mu_{SX}} - B_X \,, \tag{6.10}$$

where $\mu_{SX} = m_S M_X/(M_X + m_S)$ is the reduced mass of the XS system and $S = D^0, D^{*0}, \bar{D}^0, \bar{D}^{*0}$. The resulting amplitude for XS scattering is:

$$\begin{aligned} T(\vec{k},\vec{p}) &= \frac{2\pi\gamma}{\mu_X}\left(p^2+k^2+\frac{2\mu_X}{m_{\bar{S}}}\vec{p}\cdot\vec{k}-2\mu_X E\right)^{-1} \\ &\quad + \frac{1}{(2\pi)^2}\int d\Omega_q \int_0^\infty dq\, \frac{q^2\, T(\vec{k},\vec{q})}{-\gamma+\sqrt{-2\mu_X\,(E-q^2/(2\mu_{SX}))-i\epsilon}} \\ &\quad \times\left(p^2+q^2+\frac{2\mu_X}{m_{\bar{S}}}\vec{p}\cdot\vec{q}-2\mu_X E\right)^{-1} . \end{aligned} \tag{6.11}$$

Performing a partial wave decomposition of $T(\vec{k},\vec{p})$:

$$T(\vec{k},\vec{p}) = \sum_l (2l+1) T_l(k,p) P_l(\cos\theta_{kp}) \,, \tag{6.12}$$

where θ_{kp} is the angle between $\vec{k}$ and $\vec{p}$ and $P_l(\cos\theta_{kp})$ is a Legendre polynomial, we obtain

$$\begin{aligned} T_l(k,p) &= \frac{2\pi\gamma}{\mu_X}\frac{m_{\bar{S}}}{2\mu_X pk}(-1)^l Q_l\left(\frac{m_{\bar{S}}}{2\mu_X pk}(p^2+k^2-2\mu_X E)\right) \\ &\quad + \frac{1}{\pi}\int_0^\infty dq\, \frac{q^2\, T_l(k,q)}{-\gamma+\sqrt{-2\mu_X\,(E-q^2/(2\mu_{SX}))-i\epsilon}} \\ &\quad \times\frac{m_{\bar{S}}}{2\mu_X pq}(-1)^l Q_l\left(\frac{m_{\bar{S}}}{2\mu_X pq}(p^2+q^2-2\mu_X E)\right) , \end{aligned} \tag{6.13}$$

where

$$Q_l(z) = \frac{1}{2}\int_{-1}^{1} dx \frac{P_l(x)}{z-x} \tag{6.14}$$

is a Legendre function of the second kind. The integral equation for the S-wave amplitude reduces to

$$\begin{aligned} T_0(k,p) &= \frac{2\pi\gamma}{\mu_X}\frac{m_{\bar{S}}}{4\mu_X pk}\ln\left(\frac{p^2+k^2+\frac{2\mu_X}{m_{\bar{S}}}pk-2\mu_X E}{p^2+k^2-\frac{2\mu_X}{m_{\bar{S}}}pk-2\mu_X E}\right) \\ &\quad +\frac{1}{\pi}\int_0^\infty dq\,\frac{q^2\,T_0(k,q)}{-\gamma+\sqrt{-2\mu_X\left(E-q^2/(2\mu_{SX})\right)-i\epsilon}} \\ &\quad \times\frac{m_{\bar{S}}}{4\mu_X pq}\ln\left(\frac{p^2+q^2+\frac{2\mu_X}{m_{\bar{S}}}pq-2\mu_X E}{p^2+q^2-\frac{2\mu_X}{m_{\bar{S}}}pq-2\mu_X E}\right)\,. \end{aligned} \tag{6.15}$$

Note that, as expected, the factors appearing in the kernel of the integral equation are completely analogous to those found in the kernel of the corresponding $2n$ halo nucleus bound state equations, Eqs. (5.60, 5.61), found in Sec. 5.2.2. Solutions of the integral equations, Eqs. (6.13, 6.15), can be obtained using standard techniques.

We can now use the solutions for the amplitudes T_l to calculate the scattering cross section. They are related to the scattering phase shifts through the relation:

$$T_l(k,k)=\frac{2\pi}{\mu_{SX}}\frac{1}{k\cot\delta_l(k)-ik}\,. \tag{6.16}$$

The differential cross section can be calculated from the phase shifts in the usual way:

$$\frac{d\sigma}{d\Omega}=\left|\sum_l\frac{2l+1}{k\cot\delta_l-ik}P_l(\cos\theta)\right|^2\,, \tag{6.17}$$

For the total cross section for XS scattering we then obtain the expression:

$$\sigma_{XS}(E)=\sum_l\frac{(2l+1)\mu_{SX}^2}{\pi}\left|T_l(k,k)\right|^2\,. \tag{6.18}$$

6.2 $XD^{(*)}$ Scattering Results and Discussion

In Fig. 6.3, we show our results for the S-wave scattering amplitude $f_0(k)$ for scattering of D^0 and D^{*0} mesons off the $X(3872)$ obtained by solving Eq. (6.15). The scattering amplitude f_0 is related to the amplitude $T_0(k,k)$ through a mass dependent factor (see analogous Eq. (2.34) in Sec. 2.2.1):

$$f_0(k)=\frac{\mu_{SX}}{2\pi}T_0(k,k)=\frac{1}{k\cot\delta_0(k)-ik}\,. \tag{6.19}$$

One can see clearly in Fig. 6.3 the influence the different masses of the D^0 and D^{*0} have on the scattering amplitude. At their peak values, the amplitude for XD^{*0}

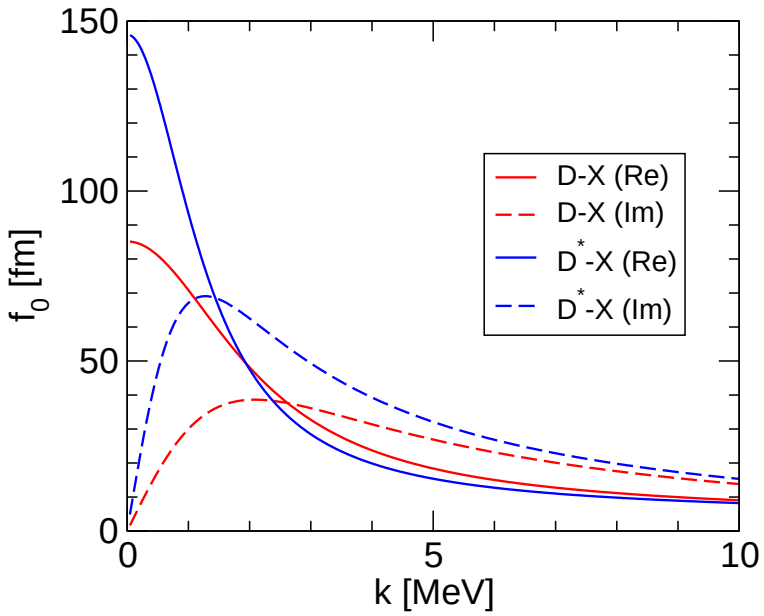

Figure 6.3: S-wave scattering amplitude for scattering of D^0 and D^{*0} mesons off the $X(3872)$. Results displayed for $f_0(k) = (\mu_{SX}/2\pi)T_0(k,k)$. The scattering amplitude is identical for particles and antiparticles.

scattering is almost twice as large as that for XD^0 scattering for both the real and imaginary parts. However, the real part of the XD^{*0} amplitude falls more quickly, moving below the real part of the XD^0 amplitude for values of approximately $k > 2$ MeV. The scattering amplitudes are the same for the scattering of particles and antiparticles.

In Fig. 6.4, we show the total cross section for scattering of D^0 and D^{*0} mesons off the $X(3872)$. We show the contribution of only S-waves ($l = 0$, solid lines) as well as the full cross section with all partial waves up to $l = 6$ (dashed lines). As one can see, the contribution of higher partial waves is negligible for momenta below ≈ 16 MeV. Also, one again clearly sees the influence of the mass difference, as the full cross section in the $k \to 0$ limit is almost three times as large for XD^{*0} as for XD^0 scattering. As with the scattering amplitude, the cross sections are the same for scattering of particles and antiparticles.

As was first defined in Sec. 2.1.1, the S-wave scattering length can be calculated from either the scattering amplitude, Eq. (2.4), or the full cross section, Eq. (2.5), in the limit $k \to 0$. From our results we find that the particle-dimer scatting lengths for scattering either a D^0 or a D^{*0} meson (or their antiparticles) off of a $X(3872)$ are:

$$a_{XD^0} = -85\,\text{fm}, \tag{6.20}$$

$$a_{XD^{*0}} = -146\,\text{fm}. \tag{6.21}$$

To observe the three-body interactions described here requires identifying an experimental process where two D^0 and one D^{*0} (or two D^{*0} and one D^0) particles are

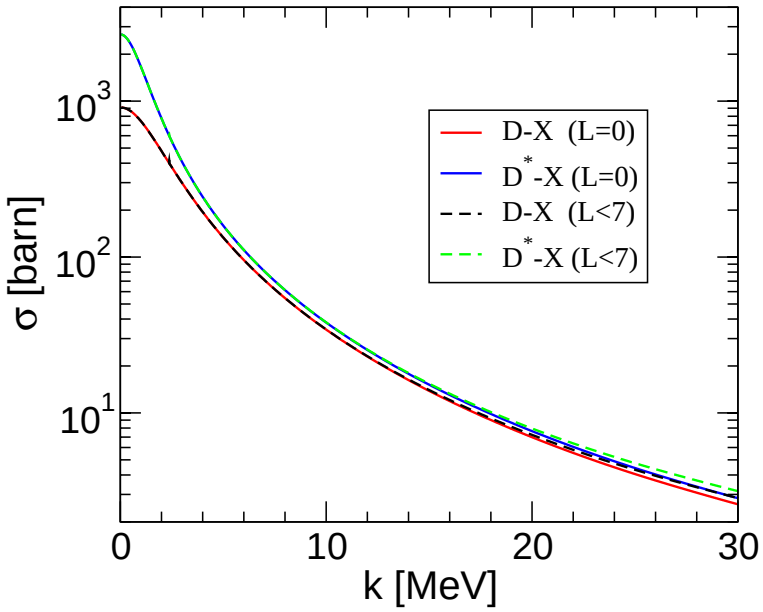

Figure 6.4: Total cross section for scattering of D^0 and D^{*0} mesons off the $X(3872)$ for S-waves ($l = 0$, solid lines) and including higher partial waves with $l < 7$ (dashed lines). The cross section is the same for scattering of particles and antiparticles.

produced nearly simultaneously in space and time. One possibility is provided by the decay of the B_c particle. The B_c was discovered through its decays into J/ψ in Run I at CDF [Ab98a, Ab98b]. Particle Data Book (2007) averages are: $m_{B_c} = 6.286 \pm 0.005$ GeV and $\tau_{B_c} = 0.46 \pm 0.07$ x 10^{-12} s. Several analyses have been undertaken (see references in [Bram04], Chapter 4) to determine the most likely mode by which the B_c would decay; the b quark decaying first, the c quark decaying first, the two valence quarks annihilating, etc.

For access to the three-body neutral D meson interactions, we require that the B_c decay in a mode such as that in Fig. 6.5, yielding three $c(\overline{c})$ quarks in the final state. The mass total for the three-body D meson system will be 5.75 to 5.88 GeV (depending upon whether the third D is a D^0 or a D^{*0}). Along with the additional meson in a P-wave required to balance the B_c charge and spin, there is not much phase space available. The q in the diagram could be the Cabbibo-favored strange quark or the Cabbibo-suppressed ($V_{cd}/V_{cs} \sim 1/4$) down quark. Relative suppression of both decay modes is caused by Pauli interference between the spectator $\overline{c}$ and the $\overline{c}$ from the (second vertex of the) weak decay of the b quark. From Ref. [Bram04]: the estimate for the quark level $B_c \to \overline{c}c\overline{c}s$ decay is about 1.4 % [Ki02]; the detection efficiency for a single D^0 is expected to be 11 to 31 %; the production cross section at the LHC (not including feeddowns, which may provide an increase of more than a factor of five, but might also be harder to identify) of the B_c is expected at the 30-60 nb level. At LHCb, the yield will be perhaps 10^7 B_c events per week of running. So the prospect of seeing the three-body neutral D meson interactions through B_c decay

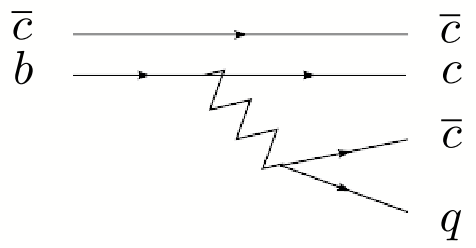

Figure 6.5: An example of a quark-level B_c decay yielding three charmed or anticharmed quarks in the final state

may well be difficult, but is worth investigating.

The effect of such final state interactions, along with the characteristics of the two-body resonance, may be reflected in the distribution in space and energy of the detected particles. Typically, (e.g., Ref. [Ama69]) there will be an enhancement or de-enhancement of the total cross section relative to the situation where three-body scattering does not occur in the final state.

6.3 Conclusion

In this chapter, we have explored the scattering of either a D^0 or D^{*0} meson (or their antiparticles) on the recently discovered exotic charmonium state $X(3872)$. The $X(3872)$ was assumed to be a weakly bound S-wave $(D^{*0}\bar{D}^0)_+$ molecule, which would then display universal behavior dependent only on its binding energy. We derived an inhomogeneous integral equation for solving the scattering amplitude from a pionless EFT approach, and found this to be a generalization to unequal masses of the particle-dimer EFT found in the review [Br06b].

Using our integral equation, we solved for the S-wave scattering amplitudes and the total cross sections with contributions of partial waves up to $l = 6$ for both the XD^0 and XD^{*0} scattering. We found that, although the results are identical for the scattering of particles and antiparticles due to charge conjugation invariance, the mass difference between the D^0 and D^{*0} mesons produce different scattering results. We then calculated the $XD^{(*)0}$ scattering lengths from our scattering amplitude results and found $a_{XD^0} = -85$ fm, and $a_{XD^{*0}} = -146$ fm. We concluded with a discussion of the possible scenarios and likelihood for observing this process at the LHC or B-factories.

Chapter 7

Summary and Outlook

In this thesis, we explored non-relativistic three-body systems through short-range interactions with a large S-wave scattering length in the two-body subsystems. Such short-range interactions are suitable for describing the two-body forces between the pairs of particles in $2n$ halo nuclei, as well as in weakly bound mesonic molecules. This illustrates the universality of our results, as they apply to all three-body systems composed of two particles with the same mass interacting with a spin-zero particle of arbitrary mass regardless of the details of the underlying interaction, as long as all pair-wise interactions have a large scattering length. Due to the separation of scales involved in such systems, we were able to use an effective S-wave separable potential built up of contact interactions in a momentum expansion. This is equivalent to taking the expansion in $l/|a|$, where l is the natural low-energy length scale of the system, and a is the large scattering length, where *large* was defined in comparison to l. The effective range of the interaction r_0 is of the same order as l. By including the next-to-leading order term in the expansion, we were able to calculate results for $2n$ halo nuclei with a theoretical uncertainty of the order of $(r_0/a)^2$. In generating our effective potential directly from the effective Lagrangian used in pionless effective field theory, we were able to show that the renormalization of the two-body interaction was completely analogous to that from the EFT. The two-body interaction T-matrix was then used in the Faddeev equations to solve the three-body problem. In the three-body problem, we required one three-body observable be fixed in order to properly renormalize our theory. For the LO case, we could simply tune the cutoff parameter Λ to reproduce the chosen three-body observable. However, in the NLO case, we included an explicit three-body force term, which was then tuned to reproduce the chosen observable.

Our main focus was on three-body halo nucleus systems composed of a spinless core surrounded by two loosely bound neutrons ($2n$ halo nuclei). We calculated low-energy universal results for these systems which are dominated by the S-wave part of the interaction, first to LO, for which only the large scattering length is needed to describe the two-body interaction, and then to NLO, for which the effective range also appears (Ch. 4 and Ch. 5, respectively). After confirming that our theory reproduces

the already well-known universal properties of the Efimov effect [Ef70], specifically in the resonant limit, $a \to \pm\infty$, for systems where two of the particles have the same mass and one particle has a different mass [Br06b], we explored the possibility of known $2n$ halo nuclei to possess an excited Efimov state. This was done by constructing the boundary curve in the parametric plane defined by the root of the ratio of the two-body energy to the three-body binding energy $\sqrt{E_{nc}/B_3^{(n)}}$ versus $\sqrt{E_{nn}/B_3^{(n)}}$. We calculated boundary curves for multiple values of the core mass. Points lying within the boundary curve possess at least one Efimov excited state above the state with binding energy $B_3^{(n)}$. Due to the discrete scaling invariance in such Efimov systems, we can always interpret the state with index n as the ground state. To leading order, the two-body energy is determined by only the scattering length, but to NLO by both a and the effective range r_0. We found that to NLO, for values of r_0 which are allowed in our effective theory, $r_0 \ll |a|$, there is almost no recognizable shift in the calculated boundary curves in comparison to the LO results. From the current experimental data, we concluded that none of the known halo nuclei is likely to have an excited Efimov state, with the possible exception of ^{20}C. We calculated the binding energy of the ^{20}C excited state as a function of the n-^{18}C binding energy and found one excited state which to LO exists for $E_{nc} < 165$ keV, with a binding energy always less than 7 keV, and which to NLO exists for $E_{nc} < 155$ keV, with a binding energy always less than 6 keV. For these NLO calculations, we estimated the as yet experimentally unknown effective ranges by the inverse of the pion mass scale $\hbar/m_\pi c = 1.4$ fm, as this is considered the natural low-energy length scale of such nuclear systems. Throughout this work, we have estimated the theoretical error of the effective potential. This uncertainty was quantified in our results through error bands.

We then studied the cluster-like structure of known $2n$ halo nuclei to both LO and NLO, extracting the mean square distance of the two particles in a chosen two-body subsystem, as well as the distance of the spectator particle from the three-body center of mass. It was shown that the NLO corrections, using the estimated effective range, generally decrease the size of Borromean halo nuclei, unless the n-c two-body virtual energy is very close to threshold. On the other hand, the size of the so called *Samba* halo nuclei, where the n-c subsystem is bound, generally increased due to effective range corrections. We found that our results to both LO and NLO for the n-n mean square radius agree well with the experimental data for the *Borromean* halo nuclei ^{11}Li and ^{14}Be [Mar00]. However, the large uncertainty in both the experimental and theoretical results suggests the need for future precision studies of these systems.

An exploration of such light nuclei is currently being done at facilities such as FAIR and FRIB, where a beam of exotic nuclei is scattered off of the Coulomb field of a heavy nucleus in low-energy experiments. This scattering can populate the excited states of the halo nuclei, which then decay in a process called "Coulomb dissociations" [Ber88]. The data from such experiments leads to useful information on halo nuclei, for example, the cluster structure, as well as scattering behavior of the underlying

two-body interactions. The effective theory developed in this thesis provides a useful quantum-mechanical framework for treating these reactions.

Also of importance is the determination of the effective range parameters, especially the scattering lengths and effective ranges, of the two-body systems found in halo nuclei. The just mentioned experiments will provide new and more precise data for some of these systems, which could lead to a more detailed analysis of effective range parameters. However, the recent theoretical work of Quaglioni and Navratil [Qu08] has produced an accurate description of S-wave neutron-core scattering of light nuclei. By combining a cluster technique, the resonating-group method, with the no-core shell model, this theory can treat the bound and scattering states of light nuclei, starting from the fundamental nucleon-nucleon interaction. The accurate calculation of S-wave neutron-core phase shifts could then be used to extract the effective range parameters needed to study three-body halo nuclei.

Although there already exists much experimental data with which to compare (see, i.e. [TUNL, Arn73], and references therein), we have purposefully not studied the ^{6}He halo nucleus, as the unbound "^{5}He" subsystem is dominated by a P-wave resonance. While various schemes to treat such P-wave resonances in EFT have been developed [Ber02, Bed03b], their application to three-body systems remains to be worked out. In a future study, we hope to generate a P-wave effective potential, similar to the one used in this work, which can then be used in the Faddeev equations to investigate three-body bound states of the ^{6}He system. Such a study would also be interesting for investigating the renormalization properties of a P-wave effective potential.

In Ch. 5, we also studied the NLO corrections to the Efimov effect for three identical bosons which arise from a non-zero effective range, comparing our results to recent studies [Pl08, Thog08]. For small effective ranges, the corrections to the trimer binding energies appear linear in r_0 according to a universal function, Eq. (5.79). We explored the universal relationship between the corrections to different Efimov states first proposed in Ref. [Pl08], showing explicitly the breaking of the discrete scale symmetry for finite scattering lengths. We also discussed the shift in the position of the critical scattering lengths, where the trimer breaks up into either three free bosons (at $a_- < 0$) or an atom-dimer pair (at $a_+ > 0$). We have shown that for increasing effective range, the absolute value of $|a_-|$ increases, while a_+ decreases. These results are important in experiments with ultracold atoms near a Feshbach resonance, as the position of the critical scattering lengths determine the positions of extrema of the three-body recombination rate [Kr06]. The effective range of the interaction is related to the width of the Feshbach resonance [Pet06]. Unfortunately, the large amount of numerical and theoretical uncertainty involved in our calculations made it difficult to make definite quantitative conclusions on the size of these NLO corrections.

We also studied the structure of the Efimov bound states, looking at the mean square distance of the two particles in the dimer subsystem, as well as the mean square distance of the spectator particle from the center of mass. We confirmed the break-up properties of these Efimov trimers at the negative and positive critical scattering lengths, as described above, and discussed the general shift in the size of the trimers

due to range corrections. We saw that the shift in the mean square radii corresponds to the shift in the binding energy, and proposed that in a future study, the deviation from discrete scaling invariance for a finite scattering length could be more easily investigated through the dimensionless quantity $(\langle r^2 \rangle B_3)$.

We then briefly moved away from the quantum-mechanical framework, and returned to a pionless EFT, in order to study the universal properties of particle-dimer scattering, for systems where two of the particles have the same mass while the third particle has different mass. We formulated this investigation around the scattering of either a D^0 or D^{*0} meson (or their antiparticles) on the $X(3872)$ meson, assumed to be a weakly bound S-wave $(D^{*0}\bar{D}^0)_+$ molecule. We showed that the mass difference between the D^0 and D^{*0} mesons produces a fairly large change in the S-wave scattering amplitude and total cross section of the XD^0 or XD^{*0} scattering. From the scattering amplitudes we were able to extract the particle-dimer scattering lengths $a_{XD^0} = -85$ fm, and $a_{XD^{*0}} = -146$ fm.

In the future it would be interesting to see how these effective theories can be applied to other potential mesonic molecules. For example, it was recently suggested that the $Y(4660)$, which was seen in the $\pi^+\pi^-\psi'$ invariant mass distribution in $e^+e^- \to \gamma_{ISR}\pi^+\pi^-\psi'$, with a mass of $4664 \pm 11 \pm 5$ MeV and a width of $48 \pm 15 \pm 3$ MeV [Wa07], could potentially be a $f_0(980)\psi'$ bound state [Gu08]. The threshold of the $f_0(980)$-ψ' system is approximately 4666 ± 10 MeV [Yao06], which would correspond to a $Y(4660)$ binding energy of ≈ 2 MeV. As we have already seen, such a small binding energy corresponds to a large S-wave scattering length. In turn, the $f_0(980)$ has been successfully treated as a $K\bar{K}$ molecule [Kal05, Hanh07a]. Therefore, we could possibly treat the $Y(4660)$ as a three-body halo-like bound state, for which two of the particles (K and $\bar{K}$) have the same mass, while the third particle (ψ') has different mass. This system is then analogous to the $2n$ halo nuclei studied in this thesis.

The results of this thesis display the usefulness of universal effective theories as a tool for describing a large variety of physical systems. Due to the large scattering length of these systems, whether accidental or experimentally controlled, the effective theory using contact interactions has been successful in calculating results from ultracold atomic systems, to $2n$ halo nuclei, up to mesonic molecules.

Appendix A

The A_i Integrals

The derivation of the two-body interaction T-matrix using a separable potential along with a Gaussian regulator function includes Gaussian-like integrals of the form:

$$A_i = 4\pi 2\mu \int_0^\infty dq \, \frac{q^{2i} \exp\left(\frac{-2q^2}{\Lambda^2}\right)}{2\mu E - q^2}. \tag{A.1}$$

For $E < 0$, these integrals can be solved using the Gaussian complementary error function:

$$\mathrm{erfc}(x) = 1 - \frac{2}{\sqrt{\pi}} \int_0^x e^{-t^2} dt. \tag{A.2}$$

The derivation begins with the A_0 integral written as follows:

$$A_0 = \frac{4\pi 2\mu}{2\mu E} \sqrt{2\mu E} \int_0^\infty dx \frac{\exp\left(\frac{-2(2\mu E)}{\Lambda^2} x^2\right)}{1 - x^2}, \tag{A.3}$$

where, here:

$$x \equiv \frac{q}{\sqrt{2\mu E}}. \tag{A.4}$$

We can now use the binomial expansion of the denominator:

$$\frac{1}{1 - x^2} = \sum_{n=0}^{\infty} x^{2n}. \tag{A.5}$$

Taking the summation outside of the integral, the Gaussian integral can be solved.

$$\begin{aligned} A_0 &= \frac{4\pi 2\mu}{2\mu E}\sqrt{2\mu E}\sum_{n=0}^{\infty}\left(\frac{1}{2}\right)^{n+1}(2n+1)!!\frac{\sqrt{\pi}}{\left(\frac{2(2\mu E)}{\Lambda^2}\right)^{\frac{2n+1}{2}}} \\ &= \frac{4\pi 2\mu}{2\mu E}\frac{\Lambda}{2}\sqrt{\frac{\pi}{2}}\sum_{n=0}^{\infty}\frac{(2n+1)!!}{2^n\left(\frac{2(2\mu E)}{\Lambda^2}\right)^n} \\ &= \frac{4\pi 2\mu}{2\mu E}\frac{\Lambda}{2}\sqrt{\frac{\pi}{2}}\sum_{n=0}^{\infty}\frac{(2n+1)!!}{2^n(-1)^n y^{2n}}, \end{aligned} \tag{A.6}$$

where

$$y \equiv \sqrt{\frac{2(-2\mu E)}{\Lambda^2}} \Rightarrow -y^2 = \frac{2(2\mu E)}{\Lambda^2}. \tag{A.7}$$

The summation is then related to the complementary error function:

$$\sum_{n=0}^{\infty}\frac{(2n+1)!!}{2^n(-1)^n y^{2n}} = \sqrt{\pi}y\exp(y^2)\mathrm{erfc}(y), \tag{A.8}$$

leading to a final result for A_0:

$$\begin{aligned} A_0 &= \frac{4\pi 2\mu}{2\mu E}\frac{\Lambda}{2}\sqrt{\frac{\pi}{2}}\sqrt{\pi}y\exp(y^2)\mathrm{erfc}(y) \\ &= -2\pi^2 2\mu\frac{\sqrt{-2\mu E}}{-2\mu E}\exp\left(\frac{2(-2\mu E)}{\Lambda^2}\right)\mathrm{erfc}\left(\frac{\sqrt{2(-2\mu E)}}{\Lambda}\right). \end{aligned} \tag{A.9}$$

Now a recursive relation can be found in order to calculate the other A_i's. For A_1, this is most easily seen by adding and subtracting by $2\mu E$ within the integral:

$$\begin{aligned} A_1 &= 4\pi 2\mu\int_0^{\infty}dq\frac{\exp\left(\frac{-2q^2}{\Lambda^2}\right)}{2\mu E - q^2}(q^2 + 2\mu E - 2\mu E) \\ &= -4\pi 2\mu\int_0^{\infty}dq\exp\left(\frac{-2q^2}{\Lambda^2}\right) + 2\mu E A_0 \\ &= -2\pi^2 2\mu\frac{\Lambda}{2}\sqrt{\frac{2}{\pi}} + 2\mu E A_0. \end{aligned} \tag{A.10}$$

By repeating this procedure one finds the relation:

$$A_i = -2\pi^2 2\mu(2i-3)!!\left(\frac{\Lambda}{2}\right)^{2i-1}\sqrt{\frac{2}{\pi}} + 2\mu E A_{i-1}, \tag{A.11}$$

or for $j \geq 1$:

$$A_j = -2\pi^2 2\mu \sum_{i=1}^{j} (2\mu E)^{j-i}(2i-3)!! \left(\frac{\Lambda}{2}\right)^{2i-1} \sqrt{\frac{2}{\pi}} + (2\mu E)^j A_0. \tag{A.12}$$

For reference A_1 through A_4 are listed here:

$$A_1 = -2\pi^2 2\mu \left[\frac{\Lambda}{2}\sqrt{\frac{2}{\pi}} - \sqrt{-2\mu E}\exp\left(\frac{2(-2\mu E)}{\Lambda^2}\right)\operatorname{erfc}\left(\frac{\sqrt{2(-2\mu E)}}{\Lambda}\right)\right], \tag{A.13}$$

$$\begin{aligned} A_2 = -2\pi^2 2\mu \Bigg[& \left(\frac{\Lambda}{2}\right)^3 \sqrt{\frac{2}{\pi}} - (-2\mu E)\frac{\Lambda}{2}\sqrt{\frac{2}{\pi}} \\ & + \sqrt{(-2\mu E)^3}\exp\left(\frac{2(-2\mu E)}{\Lambda^2}\right)\operatorname{erfc}\left(\frac{\sqrt{2(-2\mu E)}}{\Lambda}\right)\Bigg], \end{aligned} \tag{A.14}$$

$$\begin{aligned} A_3 = -2\pi^2 2\mu \Bigg[& 3\left(\frac{\Lambda}{2}\right)^5 \sqrt{\frac{2}{\pi}} - (-2\mu E)\left(\frac{\Lambda}{2}\right)^3 \sqrt{\frac{2}{\pi}} + (-2\mu E)^2 \frac{\Lambda}{2}\sqrt{\frac{2}{\pi}} \\ & - \sqrt{(-2\mu E)^5}\exp\left(\frac{2(-2\mu E)}{\Lambda^2}\right)\operatorname{erfc}\left(\frac{\sqrt{2(-2\mu E)}}{\Lambda}\right)\Bigg], \end{aligned} \tag{A.15}$$

$$\begin{aligned} A_4 = -2\pi^2 2\mu \Bigg[& 15\left(\frac{\Lambda}{2}\right)^7 \sqrt{\frac{2}{\pi}} - (-2\mu E)\ 3\left(\frac{\Lambda}{2}\right)^5 \sqrt{\frac{2}{\pi}} + (-2\mu E)^2 \left(\frac{\Lambda}{2}\right)^3 \sqrt{\frac{2}{\pi}} \\ & - (-2\mu E)^3 \frac{\Lambda}{2}\sqrt{\frac{2}{\pi}} + \sqrt{(-2\mu E)^7}\exp\left(\frac{2(-2\mu E)}{\Lambda^2}\right)\operatorname{erfc}\left(\frac{\sqrt{2(-2\mu E)}}{\Lambda}\right)\Bigg]. \end{aligned} \tag{A.16}$$

The derivation of the two-body interaction T-matrix using a separable potential along with a strong cutoff, as opposed to the Gaussian regulator scheme, differs due to the results for the A_i integrals. The integrals using a strong cutoff are of the form:

$$A_i = 4\pi 2\mu \int_0^{\Lambda} dq\ \frac{q^{2i}}{2\mu E - q^2}. \tag{A.17}$$

For $E < 0$, these integrals can be solved analytically using trigonometric functions. Starting with the A_0 and A_1 integrals we find:

$$A_0 = -2\pi^2 2\mu \frac{1}{\sqrt{-2\mu E}} \frac{2}{\pi} \arctan\left(\frac{\Lambda}{\sqrt{-2\mu E}}\right), \tag{A.18}$$

$$A_1 = -2\pi^2 2\mu \left[\frac{2}{\pi}\Lambda - \sqrt{-2\mu E}\frac{2}{\pi}\arctan\left(\frac{\Lambda}{\sqrt{-2\mu E}}\right)\right], \tag{A.19}$$

which we see are analogous to Eqs. (A.9, A.13). In solving for the other A_i integrals using a strong cutoff, we find that to switch from a Gaussian regulator to a strong cutoff one must simply replace the forms of the regulator factor and the Λ dependent terms using the following prescription:

	Gaussian Regulator	Strong Cutoff
	$\exp\left(\frac{2(-2\mu E)}{\Lambda^2}\right)\operatorname{erfc}\left(\frac{\sqrt{2(-2\mu E)}}{\Lambda}\right)$	$\frac{2}{\pi}\arctan\left(\frac{\Lambda}{\sqrt{-2\mu E}}\right)$
	$(n-2)!!\left(\frac{\Lambda}{2}\right)^n\sqrt{\frac{2}{\pi}}$	$\frac{2}{\pi}\frac{1}{n}\Lambda^n.$

Here we see that in both cases the regulator factors quickly approach 1 as Λ becomes much larger than $\sqrt{-2\mu E}$.

Appendix B

The Overlap-Matrix Element

The solution of the Faddeev equations requires the solution of the recoupling of two Jacobi momentum states. The derivation of this overlap-matrix element was done for three identical spin-1/2 particles in the book by Glöckle [Gl83]. A good review of the use of the overlap-matrix element in the Faddeev equations can also be found in Ref. [Wit08]. The analogous result for an arbitrary three-body system is presented here.

While a more detailed description of the Jacobi momentum and the corresponding Jacobi momentum basis states is given in Sec. 3.2, we review the basic concepts needed in the overlap-matrix elements.

For three particles (i, j and k) with momenta $\vec{k}_i$ and masses m_i, the Jacobi momenta are defined as:

$$\vec{p}_i = \mu_{jk}\left(\frac{\vec{k}_j}{m_j} - \frac{\vec{k}_k}{m_k}\right) \qquad \text{and} \qquad \vec{q}_i = \mu_{i,jk}\left(\frac{\vec{k}_i}{m_i} - \frac{\vec{k}_j + \vec{k}_k}{m_j + m_k}\right), \tag{B.1}$$

where $\vec{p}_i$ is the relative center-of-mass momentum of the two-body subsystem, composed of particles j and k, and $\vec{q}_i$ is the momentum of particle i relative to the center of mass of the two-body subsystem.[1] The two-body and three-body reduced masses are given by:

$$\mu_{jk} = \frac{m_j m_k}{m_j + m_k} \qquad \text{and} \qquad \mu_{i,jk} = \frac{m_i(m_j + m_k)}{m_i + m_j + m_k}. \tag{B.2}$$

The relations for other choices of spectator particles can be easily obtained through a cyclic permutation of ijk in Eqs. (B.1,B.2).

The Jacobi momenta can be used to define a complete basis of vector Jacobi states:

$$|\,\vec{p}\vec{q}\rangle_i \equiv |\,\vec{p}_i\vec{q}_i\rangle. \tag{B.3}$$

[1] The spectator notation is used throughout. In this notation the index refers to the spectator particle of the three-body system. The exceptions are the variables which refer to individual particles, for example, the individual particle momenta $\vec{k}_i$, the individual masses m_i, or individual spin or isospin quantum numbers s_i or t_i, as well as the various reduced masses μ_{ij} or $\mu_{i,jk}$.

One then constructs a partial wave projected basis state from these states, which is then used in the application to the Faddeev equations:

$$\begin{aligned} \mid pq\mathcal{J}\rangle_i &\equiv \mid p_i q_i \mathcal{J}_i\rangle \\ &\equiv \mid pq[(ls)j(\lambda\sigma)\mathbf{j}]JM_J(t\mathbf{t})TM_T\rangle_i, \end{aligned} \tag{B.4}$$

where $\mathcal{J}_i$ is used as an abbreviation for all the discrete quantum numbers. The definition of every quantum number in the partial wave basis state can be found in Sec. 3.2.2.

The solution of the Faddeev equations requires the recoupling of two Jacobi momentum states in an overlap-matrix element of the form:

$$ {}_i\langle pq\mathcal{J} \mid p'q'\mathcal{J}'\rangle_j. \tag{B.5}$$

However, it is useful to decouple the momentum-, spin-, and isospin-space according to the well known prescription using the $9j$ symbol [Ed96]:

$$\mid pq\mathcal{J}\rangle_i = \sum_{LS} \sqrt{\hat{j}\hat{\mathbf{j}}\hat{L}\hat{S}} \left\{ \begin{array}{ccc} l & s & j \\ \lambda & \sigma & \mathbf{j} \\ L & S & J \end{array} \right\} \mid pq(l\lambda)L\rangle_i \ \mid (s\sigma)S\rangle_i \ \mid (t\mathbf{t})T\rangle_i, \tag{B.6}$$

where in all expressions, the hatted quantum numbers are

$$\hat{j} \equiv 2j+1. \tag{B.7}$$

The overlap-matrix element is therefore

$$\begin{aligned} {}_i\langle pq\mathcal{J} \mid p'q'\mathcal{J}'\rangle_j = \sum_{LS}\sum_{L'S'} \sqrt{\hat{j}\hat{\mathbf{j}}\hat{L}\hat{S}}\sqrt{\hat{j}'\hat{\mathbf{j}}'\hat{L}'\hat{S}'} \left\{ \begin{array}{ccc} l & s & j \\ \lambda & \sigma & \mathbf{j} \\ L & S & J \end{array} \right\} \left\{ \begin{array}{ccc} l' & s' & j' \\ \lambda' & \sigma' & \mathbf{j}' \\ L' & S' & J' \end{array} \right\} \\ {}_i\langle pq(l\lambda)L \mid p'q'(l'\lambda')L'\rangle_j \ {}_i\langle (s\sigma)S \mid (s'\sigma')S'\rangle_j \ {}_i\langle (t\mathbf{t})T \mid (t'\mathbf{t}')T'\rangle_j. \end{aligned} \tag{B.8}$$

The problem is now the calculation of three recoupling matrix elements for the momentum, spin, and isospin.

The spin and isospin parts are completely analogous to one another and easily solved from the known properties of angular momentum recoupling coefficients. Using the $6j$ symbol [Ed96]:

$$ {}_i\langle (s\sigma)S \mid (s'\sigma')S'\rangle_j = \delta_{SS'}\sqrt{\hat{s}\hat{s}'}(-1)^{s_i+2s_j+s_k+s'} \left\{ \begin{array}{ccc} s_j & s_k & s \\ s_i & S & s' \end{array} \right\} \tag{B.9}$$

and

$$ {}_i\langle (t\mathbf{t})T \mid (t'\mathbf{t}')T'\rangle_j = \delta_{TT'}\sqrt{\hat{t}\hat{t}'}(-1)^{t_i+2t_j+t_k+t'} \left\{ \begin{array}{ccc} t_j & t_k & t \\ t_i & T & t' \end{array} \right\}. \tag{B.10}$$

The momentum part of the overlap-matrix element in Eq. (B.8) is at the very root of the three-body problem as it holds all the mechanics of the interplay between two different three-body states. The derivation is complicated and tedious, and follows the procedure in Ref. [Gl83]. For brevity, we present only the final result for arbitrary masses and spins, which naturally has the same structure as the result of Ref. [Gl83]:

$$ {}_i\langle pq\mathcal{J} \mid p'q'\mathcal{J}'\rangle_j = \int_{-1}^{1} dx \, \frac{\delta(p-\tilde{\pi}_j)}{p\tilde{\pi}_j^{l+1}} \frac{\delta(p'-\tilde{\pi}'_j)}{p'\tilde{\pi}_j^{\prime l'+1}} G_{\mathcal{J}\mathcal{J}'}(qq'x), \tag{B.11} $$

where

$$ \tilde{\pi}_j = \sqrt{\left(\frac{\mu_{jk}}{m_k}\right)^2 q^2 + q'^2 + 2\frac{\mu_{jk}}{m_k} qq'x} \tag{B.12} $$

and

$$ \tilde{\pi}'_j = \sqrt{q^2 + \left(\frac{\mu_{ki}}{m_k}\right)^2 q'^2 + 2\frac{\mu_{ki}}{m_k} qq'x}. \tag{B.13} $$

The angular dependence is now found in the x variable, which is the cosine of the angle between q and q'.

Notice the choice of delta functions in Eq. (B.11). The delta functions could be chosen in order to fix two of the four momenta, or one momentum and the x variable. In our present case, in order to derive the most useful form of the Faddeev equations for halo nuclei, we fix the two-body subsystem momenta p and p' in terms of the spectator momenta q and q'. However, in reconstructing the full wave function from its Faddeev components, it is more useful to fix the momentum on the right hand side of the overlap-matrix element p' and q' in terms of the momentum on the left hand side p and q. The solution for this choice of delta functions can be found in [No01].

The x dependence of the G function is expanded in Legendre polynomials, and has the form:

$$ \begin{aligned} G_{\mathcal{J}\mathcal{J}'}(qq'x) &= \sum_{\mathbf{k}} P_{\mathbf{k}}(x) \sum_{l_1+l_2=l} \sum_{l'_1+l'_2=l'} \left(\frac{\mu_{jk}}{m_k}\right)^{l_1} \left(\frac{\mu_{ki}}{m_k}\right)^{l'_2} \\ &\quad (q)^{l_1+l'_1} (q')^{l_2+l'_2} g_{\mathcal{J}\mathcal{J}'}^{\mathbf{k}l_1l_2l'_1l'_2}. \end{aligned} \tag{B.14} $$

The quantity $g_{\mathcal{J}\mathcal{J}'}^{\mathbf{k}l_1l_2l'_1l'_2}$ is a completely geometrical function of the angular momentum quantum numbers. Because the total three-body angular momentum cannot depend on the choice of Jacobi coordinates, g is diagonal in J and M_J. Also, because the parity is not changed $(-1)^{l+\lambda} = (-1)^{l'+\lambda'}$. The explicit form of g for our choice of

delta functions, using $6j$ and $9j$ symbols, as well as Clebsch-Gordan coefficients C, is:

$$
\begin{aligned}
g_{\mathcal{J}\mathcal{J}'}^{\mathbf{k}l_1l_2l_1'l_2'} &= \frac{1}{2}\hat{\mathbf{k}}\sum_{LS}\hat{L}\hat{S}\sqrt{\hat{l}\hat{j}\hat{\lambda}\hat{\mathbf{j}}\hat{l}'\hat{j}'\hat{\lambda}'\hat{\mathbf{j}}'}(-1)^{l'}\left\{\begin{array}{ccc} l & s & j \\ \lambda & \sigma & \mathbf{j} \\ L & S & J \end{array}\right\}\left\{\begin{array}{ccc} l' & s' & j' \\ \lambda' & \sigma' & \mathbf{j}' \\ L & S & J \end{array}\right\} \\
&\sqrt{\frac{\hat{l}!}{(2l_1)!(2l_2)!}}\sqrt{\frac{\hat{l}'!}{(2l_1')!(2l_2')!}}\ \sqrt{\hat{s}\hat{s}'}(-1)^{s_i+2s_j+s_k+s'}\left\{\begin{array}{ccc} s_j & s_k & s \\ s_i & S & s' \end{array}\right\} \\
&\sqrt{\hat{t}\hat{t}'}(-1)^{t_i+2t_j+t_k+t'}\left\{\begin{array}{ccc} t_j & t_k & t \\ t_i & T & t' \end{array}\right\} \\
&\sum_{ff'}\left\{\begin{array}{ccc} l_2 & l_1 & l \\ \lambda & L & f \end{array}\right\}C(l_1\lambda f,00)\left\{\begin{array}{ccc} l_1' & l_2' & l' \\ \lambda' & L & f' \end{array}\right\}C(l_2'\lambda' f',00) \\
&\left\{\begin{array}{ccc} f & l_2 & L \\ f' & l_1' & \mathbf{k} \end{array}\right\}C(\mathbf{k}l_2f',00)C(\mathbf{k}l_1'f,00). \qquad \text{(B.15)}
\end{aligned}
$$

Bibliography

[Ab98a] F. Abe *et al.* [CDF Collaboration], Phys. Rev. D **58** (1998) 112004 [arXiv:hep-ex/9804014].

[Ab98b] F. Abe *et al.* [CDF Collaboration], Phys. Rev. Lett. **81** (1998) 2432 [arXiv:hep-ex/9805034].

[Ac04] D.E. Acosta *et al.* [CDF II Collaboration], Phys. Rev. Lett. **93** (2004) 072001 [arXiv:hep-ex/0312021].

[Ada08] I. Adachi *et al.* [Belle Collaboration], arXiv:0809.1224 [hep-ex].

[Adh88] S.K. Adhikari, A. Delfino, T. Frederico, I.D. Goldman, and L. Tomio, Phys. Rev. A **37** (1988) 3666.

[Ama69] R.D. Amado and J.V. Noble, Phys. Rev. **185** (1969) 1993.

[Amo96] A.E.A. Amorim, T. Frederico and L. Tomio, Phys. Rev. C **56** (1997) R2378 [arXiv:nucl-th/9708023].

[Arn73] R.A. Arndt, D.L. Long, and L.D. Roper, Nucl. Phys. A **209** (1973) 429.

[Aro04] V. Arora, I. Mazumdar, and V.S. Bhasin, Phys. Rev. C **69** (2004) R061301.

[Aub08] B. Aubert *et al.* [BABAR Collaboration], Phys. Rev. D **77** (2008) 111101 [arXiv:0803.2838 [hep-ex]].

[Aud95] G. Audi and A.H. Wapstra, Nucl. Phys. **A595** (1995) 409.

[Ba09] G. Barontini *et al.*, arXiv:0901.4584 [cond-mat.other].

[Bed99] P.F. Bedaque, H.-W. Hammer, and U. van Kolck, Phys. Rev. Lett. **82** (1999) 463 [arXiv:nucl-th/9809025]; Nucl. Phys. A **646** (1999) 444 [arXiv:nucl-th/9811046].

[Bed02] P.F. Bedaque and U. van Kolck, Ann. Rev. Nucl. Part. Sci. **52** (2002) 339 [arXiv:nucl-th/0203055].

[Bed03a] P.F. Bedaque, G. Rupak, H.W. Griesshammer, and H.-W. Hammer, Nucl. Phys. A **714** (2003) 589 [arXiv:nucl-th/0207034].

[Bed03b] P.F. Bedaque, H.-W. Hammer and U. van Kolck, Phys. Lett. B **569** (2003) 159 [arXiv:nucl-th/0304007].

[Ber88] C.A. Bertulani and G. Baur, Phys. Rep. **163** (1988) 299.

[Ber02] C.A. Bertulani, H.-W. Hammer and U. Van Kolck, Nucl. Phys. A **712** (2002) 37 [arXiv:nucl-th/0205063].

[Ber07] C.A. Bertulani and M.S. Hussein, Phys. Rev. C **76** (2007) 051602 [arXiv:0705.3998 [nucl-th]].

[Ber09] C.A. Bertulani, R. Higa, and U. van Kolck, in progress.

[Br04a] E. Braaten and H.-W. Hammer, Phys. Rev. A **70** (2004) 042706 [arXiv:cond-mat/0303249].

[Br04b] E. Braaten and M. Kusunoki, Phys. Rev. D **69** (2004) 074005 [arXiv:hep-ph/0311147].

[Br04c] E. Braaten and M. Kusunoki, Phys. Rev. D **69** (2004) 114012 [arXiv:hep-ph/0402177].

[Br04d] E. Braaten, M. Kusunoki and S. Nussinov, Phys. Rev. Lett. **93** (2004) 162001 [arXiv:hep-ph/0404161].

[Br05a] E. Braaten and M. Kusunoki, Phys. Rev. D **71** (2005) 074005 [arXiv:hep-ph/0412268].

[Br05b] E. Braaten and M. Kusunoki, Phys. Rev. D **72** (2005) 014012 [arXiv:hep-ph/0506087].

[Br05c] E. Braaten and M. Kusunoki, Phys. Rev. D **72** (2005) 054022 [arXiv:hep-ph/0507163].

[Br06a] E. Braaten, Phys. Rev. D **73** (2006) 011501 [arXiv:hep-ph/0408230].

[Br06b] E. Braaten and H.-W. Hammer, Phys. Rept. **428** (2006) 259 [arXiv:cond-mat/0410417].

[Br06c] E. Braaten and M. Lu, Phys. Rev. D **74** (2006) 054020 [arXiv:hep-ph/0606115].

[Br07] E. Braaten and M. Lu, Phys. Rev. D **76** (2007) 094028 [arXiv:0709.2697 [hep-ph]].

[Br08a] E. Braaten and M. Lu, Phys. Rev. D **77** (2008) 014029 [arXiv:0710.5482 [hep-ph]].

[Br08b] E. Braaten, Phys. Rev. D **77** (2008) 034019 [arXiv:0711.1854 [hep-ph]].

[Br08c] E. Braaten, H.-W. Hammer, D. Kang and L. Platter, Phys. Rev. A **78** (2008) 043605 [arXiv:0801.1732 [cond-mat.other]].

[Br08d] E. Braaten, arXiv:0808.2948 [hep-ph].

[Br09] Eric Braaten, talk presented at the EFT09 meeting, February 1-6, 2009, Valencia, Spain.

[Bram04] N. Brambilla *et al.* [Quarkonium Working Group], arXiv:hep-ph/0412158.

[Ca08] D.L. Canham and H.-W. Hammer, Eur. Phys. J. A **37** (2008) 367 [arXiv:0807.3258 [nucl-th]].

[CDF08] CDF collaboration, talk presented by Thomas Kuhr at the QWG08 meeting, December 2-5 2008, Nara, Japan.

[Ch03] S.K. Choi *et al.* [Belle Collaboration], Phys. Rev. Lett. **91** (2003) 262001 [arXiv:hep-ex/0309032].

[Da99] J. Dalibard, "Collisional dynamics of ultra-cold atomic gases," in *Bose-Einstein Condensation in Gases*, ed. M. Inguscio, S. Stringari, and C.E. Wieman, pp. 321-349 (IOS Press, 1999).

[Ed96] A.R. Edmonds, *Angular Momentum in Quantum Mechanics*, (Princeton University Press, 1996).

[Ef70] V. Efimov, Phy. Lett. **33B** (1970) 563.

[Ef90] V. Efimov, Comments Nucl. Part. Phys. **19** (1990) 271.

[Ei07] E. Eichten, S. Godfrey, H. Mahlke and J.L. Rosner, Rev. Mod. Phys. **80** (2008) 1161 [arXiv:hep-ph/0701208].

[Ep08] E. Epelbaum, H.-W. Hammer and U.-G. Meissner, arXiv:0811.1338 [nucl-th].

[Fa61] L.D. Faddeev, Sov. Phys. JETP **12** (1961) 1014 [Zh. Eksp. Teor. Fiz. **39** (1960) 1459].

[Fed94] D.V. Fedorov, A.S. Jensen and K. Riisager, Phys. Rev. Lett. **73** (1994) 2817 [arXiv:nucl-th/9409018].

[Fes62] H. Feshbach, Ann. Phys. **19** (1962) 287.

[Few95] C.J. Fewster, J. Phys. A **28** (1995) 1107 [arXiv:hep-th/9412050].

[Ge93] H. Georgi, Ann. Rev. Nucl. Part. Sci. **43** (1993) 209.

[Gl83] W. Glöckle, *The Quantum Mechanical Few-Body Problem*, (Springer, 1983).

[God08] S. Godfrey and S.L. Olsen, arXiv:0801.3867 [hep-ph].

[Gon99] D.E. Gonzales Trotter *et al.*, Phys. Rev. Lett. **83** (1999) 3788.

[Gr00] R.E. Grisenti *et al.*, Phys. Rev. Lett. **85** (2000) 2284.

[Gu08] F.K. Guo, C. Hanhart and U.-G. Meissner, Phys. Lett. B **665** (2008) 26 [arXiv:0803.1392 [hep-ph]].

[Hag07] K. Hagino and H. Sagawa, Phys. Rev. C **76** (2007) 047302 [arXiv:0708.1543 [nucl-th]].

[Ham01] H.-W. Hammer and T. Mehen, Phys. Lett. B **516** (2001) 353. [arXiv:nucl-th/0105072].

[Ham06] H.-W. Hammer, T.A. Lahde and L. Platter, Phys. Rev. A **75** (2007) 032715 [arXiv:cond-mat/0611769].

[Ham08] H.-W. Hammer and R. Higa, Eur. Phys. J. A **37** (2008) 193 [arXiv:0804.4643 [nucl-th]].

[Hanh07a] C. Hanhart, Yu.S. Kalashnikova, A.E. Kudryavtsev and A.V. Nefediev, Phys. Rev. D **75** (2007) 074015 [arXiv:hep-ph/0701214].

[Hanh07b] C. Hanhart, Yu.S. Kalashnikova, A.E. Kudryavtsev and A.V. Nefediev, Phys. Rev. D **76** (2007) 034007 [arXiv:0704.0605 [hep-ph]].

[Hans95] P.G. Hansen, A.S. Jensen, and B. Jonson, Ann. Rev. Nucl. Part. Sci. **45** (1995) 591.

[He99] D.J. Heinzen, "Ultra-cold atomic interactions," in *Bose-Einstein Condensation in Gases*, ed. M. Inguscio, S. Stringari, and C.E. Wieman, pp. 351-389 (IOS Press, Amsterdam, 1999).

[Hi08] R. Higa, H.-W. Hammer and U. van Kolck, Nucl. Phys. A **809** (2008) 171 [arXiv:0802.3426 [nucl-th]].

[Hu08] J.H. Huckans, J.R. Williams, E.L. Hazlett, R.W. Stites and K.M. O'Hara, arXiv:0810.3288.

[Je04] A.S. Jensen, K. Riisager, D.V. Fedorov, and E. Garrido, Rev. Mod. Phys. **76** (2004) 215.

[Kal05] Yu.S. Kalashnikova, A.E. Kudryavtsev, A.V. Nefediev, C. Hanhart and J. Haidenbauer, Eur. Phys. J. A **24** (2005) 437 [arXiv:hep-ph/0412340].

[Kap95] D.B. Kaplan, arXiv:nucl-th/9506035.

[Kap98] D.B. Kaplan, M.J. Savage and M.B. Wise, Nucl. Phys. B **534** (1998) 329 [arXiv:nucl-th/9802075].

[Kh72] V.F. Kharchenko, Sov. J. Nucl. Phys. **16** (1973) 173 [Yad. Fiz. **16** (1972) 310].

[Ki02] V.V. Kiselev, arXiv:hep-ph/0211021.

[Kn08] S. Knoop *et al.*, arXiv:0807.3306 [cond-mat].

[Kr06] T. Kraemer *et al.*, Nature **440** (2006) 315 [arXiv:cond-mat/0512394v2].

[Man96] A.V. Manohar, arXiv:hep-ph/9606222.

[Mar00] F.M. Marqués *et al.*, Phys. Lett. B **476** (2000) 219; Phys. Rev. C **64** (2001) 061301.

[Maz00] I. Mazumdar, V. Arora, and V.S. Bhasin, Phys. Rev. C **61** (2000) R051303.

[Maz06] I. Mazumdar, A.R.P. Rau and V.S. Bhasin, Phys. Rev. Lett. **97** (2006) 062503 [arXiv:quant-ph/0607193].

[Me00] T. Mehen, I.W. Stewart and M.B. Wise, Phys. Lett. B **474** (2000) 145 [arXiv:hep-th/9910025].

[Mi90] G.A. Miller, B.M.K. Nefkens and I. Slaus, Phys. Rept. **194** (1990) 1.

[Na99] T. Nakamura *et al.*, Phys. Rev. Lett. **83** (1999) 1112.

[No01] A. Nogga, Ph.D. thesis, Ruhr-Universität, Bochum, 2001; http://www-brs.ub.ruhr-uni-bochum.de/netahtml/HSS/Diss/NoggaAndreas/

[Or08] N.A. Orr, arXiv:0803.0886 [nucl-ex].

[Ot08] T.B. Ottenstein, T. Lompe, M. Kohnen, A.N. Wenz and S. Jochim, Phys. Rev. Lett. **101** (2008) 203202 [arXiv:0806.0587 [cond-mat]].

[Pes95] M.E. Peskin and D.V. Schroeder, *An Introduction to Quantum Field Theory*, (Addison-Wesley Publishing Company, 1995).

[Pet06] D.S. Petrov, Phys. Rev. Lett. **93** (2004) 143201.

[Ph96] D.R. Phillips and T.D. Cohen, Phys. Lett. B **390** (1997) 7 [arXiv:nucl-th/9607048].

[Ph97] D.R. Phillips, S.R. Beane and T.D. Cohen, Annals Phys. **263** (1998) 255 [arXiv:hep-th/9706070].

[Ph02] D.R. Phillips, Czech. J. Phys. **52** (2002) B49 [arXiv:nucl-th/0203040].

[Pl04a] L. Platter, H.-W. Hammer and U.-G. Meißner, Phys. Rev. A **70** (2004) 052101 [arXiv:cond-mat/0404313].

[Pl04b] L. Platter, H.-W. Hammer and U.-G. Meißner, Few Body Syst. **35** (2004) 169 [arXiv:cond-mat/0405660].

[Pl05] L. Platter, H.-W. Hammer, and U.-G. Meißner, Phys. Lett. B **607** (2005) 254 [arXiv:nucl-th/0409040].

[Pl06a] L. Platter and D.R. Phillips, Few Body Syst. **40** (2006) 35. [arXiv:cond-mat/0604255].

[Pl06b] L. Platter, Phys. Rev. C **74** (2006) 037001 [arXiv:nucl-th/0606006].

[Pl08] L. Platter, C. Ji and D.R. Phillips, arXiv:0808.1230 [cond-mat.other].

[Qu08] S. Quaglioni and P. Navratil, Phys. Rev. Lett. **101** (2008) 092501 [arXiv:0804.1560 [nucl-th]]; arXiv:0901.0950 [nucl-th].

[Ri94] K. Riisager, Rev. Mod. Phys. **66** (1994) 1105.

[Ro99] F. Robicheaux, Phys. Rev. A **60** (1999) 1706.

[Sw06] E.S. Swanson, Phys. Rept. **429** (2006) 243 [arXiv:hep-ph/0601110].

[Ta96] I. Tanihata, J. Phys. G **22** (1996) 157.

[Thoe00] M. Thoennessen, S. Yokoyama, P. G. Hansen, Phys. Rev. C **63** (2000) 014308.

[Thog08] M. Thøgersen, D.V. Fedorov and A.S. Jensen, Phys. Rev. A **78** (2008) 020501.

[Thom35] L.H. Thomas, Phys. Rev. **47** (1935) 903.

[Ti92] E. Tiesinga, A.J. Moerdijk, B.J. Verhaar, and H.T.C. Stoof, Phys. Rev. A **46** (1992) 1167.

[Ti93] E. Tiesinga, B.J. Verhaar, and H.T.C. Stoof, Phys. Rev. A **47** (1993) 4114.

[TUNL] TUNL nuclear data evaluation project WWW: http://www.tunl.duke.edu/NuclData/.

[vK99] U. van Kolck, Nucl. Phys. A **645** (1999) 273 [arXiv:nucl-th/9808007].

[Vo07] M.B. Voloshin, Prog. Part. Nucl. Phys. **61** (2008) 455 [arXiv:0711.4556 [hep-ph]].

[Wa07] X.L. Wang *et al.* [Belle Collaboration], Phys. Rev. Lett. **99** (2007) 142002 [arXiv:0707.3699 [hep-ex]].

[We72] S. Weinberg, *Gravitation and Cosmology: Principles and Applications of the General Theory of Relativity*, (John Wiley and Sons, Inc., 1972).

[Wig55] E.P. Wigner, Phys. Rev. **98** (1955) 145.

[Wil75] K.H. Wilcox *et al.*, Phys. Lett. **59B** (1975) 142.

[Wit08] H. Witala and W. Glöckle, Eur. Phys. J. A **37** (2008) 87 [arXiv:0806.2757 [nucl-th]].

[Yam04] M.T. Yamashita, L. Tomio and T. Frederico, Nucl. Phys. A **735** (2004) 40 [arXiv:nucl-th/0401063].

[Yam06] M.T. Yamashita, T. Frederico, and M.S. Hussein, Mod. Phys. Lett. A **21** (2006) 1749 [arXiv:nucl-th/0501052].

[Yam08a] M.T. Yamashita, T. Frederico and L. Tomio, Phys. Lett. B **660** (2008) 339 [arXiv:0704.1461 [nucl-th]].

[Yam08b] M.T. Yamashita, T. Frederico and L. Tomio, Phys. Lett. B **670** (2008) 49 [arXiv:0808.3113 [nucl-th]].

[Yao06] W.M. Yao *et al.* [Particle Data Group], J. Phys. G **33** (2006) 1.

[Zh93] M.V. Zhukov, B.V. Danilin, D.V. Fedorov, J.M. Bang, I.J. Thompson, and J.S. Vaagen, Phys. Rep. **231** (1993) 151.

[Zi02] J. Zinn-Justin, *Quantum Field Theory and Critical Phenomena*, (Clarendon Press, 2002).

Acknowledgments

Although I try to sometimes, I can not make it through life without help. I am in constant need and there are many people who have in one way or another fulfilled needs in my life. I would like to thank as many of you as possible who have given your support and encouragement during this unlikely adventure.

First of all, I thank my Lord Jesus Christ, who is the provider of all I really need and, in a way, the origin of all the thanks that follow. After all, "every good and perfect gift is from above," (James 1:17).

Whenever I give thanks, I always give thanks for my parents, to whom I dedicate this work. I thank you for your unfailing love and support throughout all of the things that I've done in life, whether it was my interest in hockey although we lived in the desert, or moving a quarter of the way around the world for this doctoral work. Thank you for not only allowing me to be involved in such seemingly outlandish adventures, but encouraging me to live out my dreams, equipping me with all I needed to give my best, as well as allowing these interests of mine to become interests of yours. I hope one day to show as much love as you have shown me.

I would like to thank the rest of my family for their love and support while I've lived so far away. Thank you, Michael and Beverly, for coming to visit and always being there for things like computer problems and advice. Thanks also to my wonderful grandparents, for being so much fun at visits, and for your continual prayers. You are all a great blessing in my life.

I thank Hans-Werner for taking me on as his first doctoral student in Bonn, although, at the time, I knew next to nothing about the topic. Thank you for always having the time to talk about the work and the struggles no matter how much else you had to do. It was also nice to have an adviser with whom I could just as often talk about sports and life outside of physics.

My thanks go to Ulf-G. Meißner for carefully reading and assessing this thesis. Thank you as well for helping my work along at certain points, and for having a good humor with the group, whether in the mensa or seminars.

I thank Lucas Platter, whose work most of this dissertation is based on. Although we've only met in person briefly, you've been friendly in all conversations, and incredibly generous in all the help you've given. Thank you as well for taking the time to proofread this work.

I thank Dr. Andreas Nogga for some helpful discussions at the very beginning of this work.

I thank Prof. E. Braaten, Prof. U. van Kolck, and Prof. D. Phillips for taking an interest in this work and providing useful discussions.

I have to give thanks to Barbara for all of the administrative work she's done. I probably would've been sent back to America by now if you hadn't taken care of things so well. Thanks as well for your openness, being a friend and not just a secretary.

I would like to thank Kerstin, who went quickly from being an officemate to becoming one of my good friends. Knowing that coming to the office meant getting to spend time talking and sharing with you made it more of a joy to go to work. Thank you as well for all of the help and encouragement you've given, work related or otherwise. Thanks for proofreading this dissertation, too.

Similarly, I thank Kathryn for making it even more of a joy to come to the office. I will miss chatting with you about the weekend's activities and struggles with the work. Thank you for making the office a comfortable and open place to talk.

I thank Bastian for all of the patience and understanding he's shown in answering a wide variety of questions, most of which were small or trivial (or not physics related at all), and always taking the time to help with sometimes even more trivial requests. It is out of a great respect for you that I keep coming back with these questions and requests.

My thanks go to Simon for being the go-to guy for all of my computer blunders and questions, especially in saving my programs when I managed to erase an entire folder. Thanks for bringing more laughter to the group as well.

I also thank everyone else on the third floor of the HISKP, with whom I've had the pleasure to work. I really am going to miss coming to the office, going to the mensa, and celebrating birthdays over coffee and cake with all of you. I am especially thankful for the times listening to the Blues in Sessions with Matthias, Robin and Renato (among others); for the laughter and conversations with Michael, Simon, Mark and Christoph (among others); and just the general good times, in the office or outside, with David, Stefan, Akaki, André, Bernard, Maxim, Dominik, Eike, Eva, Konstantin,. . . . Soccer (sorry, football) was also a grand time.

I thank my beautiful Tabea, for being so warm, kind and loving. Your patience and compassion, especially during these last stressful weeks, have been an incredible source of encouragement and support in my life. Thank you for giving me a reason to stay in Germany, even after this doctoral work is through. Your love has brought me so much joy.

Give thanks to the Lord*, for he is good;*
his love endures forever.
Psalm 118:1